The impact of structure on the electrical transport properties of nitrogen-doped carbon microspheres

Vincent Derek Marsicano

A thesis submitted to the Faculty of Science, University of the Witwatersrand, Johannesburg, in fulfilment of the requirements for the degree of Doctor of Philosophy.

April 2016

Declaration

I declare that this is my own, unaided work, other than where acknowledged. It is being submitted in fulfilment of the requirements for the degree of Doctor of Philosophy in Physics to the University of the Witwatersrand, Johannesburg. It has not been submitted for any degree or examination in any other university.

Signed this 23^{rd} day of October 2016

Vincent Marsicano

Digitally signed by Vincent Marsicano
DN: cn=Vincent Marsicano, o, ou, email=vincent@piware.co.za, c=ZA
Date: 2016.10.27 08:09:50 +02'00'

Vincent Derek Marsicano

Abstract

Chemical vapour deposition was used to synthesise four carbon microspheres (CMS) samples. Introduction of acetonitrile in different quantities produced spheres of differing nitrogen concentration. The structure of the spheres was investigated using Raman spectroscopy, scanning electron microscopy and X-ray photoelectron spectroscopy techniques. The Raman investigation revealed a decrease in average graphitic flake size which forms the surface layers of the spheres with nitrogen incorporation. XPS showed that increased nitrogen doping caused a larger proportion of pyridinic nitrogen, which process likely restricts the growth of the crystallite flakes detected with the Raman technique. Microscopy revealed spheres with differing morphologies which did not correlated with the level of nitrogen doping. Electron paramagnetic resonance techniques were employed to investigate the impact of nitrogen doping on the spin system of the samples. Electrical transport and Hall effect data were collected with an automated experiment station purpose built for this work. Samples displayed semiconducting behaviour at low temperatures which was ascribed to fluctuation assisted tunnelling. At higher temperatures all four samples display a transition to metallic behaviour. Models for conduction, which were tested but ultimately rejected, include variable range hopping in all its dimensional forms, Efros-Shklovskii VRH and weak localisation. A comparison of the conduction results and the structural information showed the conductivity to be more closely affected by the structure of the spheres than the overall doping level. A case is made for the dominant conduction mechanism being determined by the intersphere rather than

the intrasphere conduction. This research shows that creating carbon microspheres with specific electrical properties requires control of the structure induced during synthesis. Nitrogen doping alone does not determine the final physical and electrical transport properties.

Acronyms and Paege Numbers

AWG - American Wire Gauge - 50

BWF - Breit-Wigner-Faro - 80

CCD - Charge-couple device - 64

CF - Carbon Fibre- 5

CMS - Carbon Microshere - 6

CNH - Carbon Nanohorn - 5

CNS - Carbon Nanosphere - 5

CNT - Carbon Nanotube - 5

CSV - Comma Separated Value - 57

CVD - Chemical Vapour Deposition - 6

DAC - Digital to Analogue Converter - 55

DC - Direct Current - 7

DP - D'yakonov-Perel - 33

DPPH - 2,2-diphenyl-1-dicrylhydrazyl - 62

EPR - Electron Paramagnetic Resonance - 27

ESR - Electron Spin Resonance - 27

ESVRH - Efros-Shklovskii Varaible Range Hopping - 70

EY - Elliot-Yafet - 33

FAT - Fluctuation Assisted Tunnelling - 72

FIT - Fluctuation Induced Tunnelling - 14

FWHM - Full Width Half Maximum - 83

GPIB - General Purpose Internet Bus - 57

GUI - Graphical User Interface - 142

IV - Current Voltage - 55

LBM - Layer Breathing Mode - 106

LWD - Long Working Distance - 64

MWCNT - Multiwalled Carbon Nanotube - 22

NC - Not Connected - 50

NMR - Nuclear Magnetic Resonance - 61

PCB - Printed Circuit Board - 54

PET - Polyethelene Terephthelate - 6

PLA - Polylactic Acid - 48

RBM - Radial Breathing Mode - 85

SEM - Scanning Electron Microscopy - 37

SPI - Serial Peripheral Interface - 56

SWCNT - Single Walled Carbon Nanotube - 33

TEM - Transmission Electron Microscopy - 37

TK - Tuinstra Koening - 86

USB - Universal Serial Bus - 122

VDP - Van Der Pauw - 67

VRH - Variable Range Hopping - 14

VDOS - Vibrational Density of States - 26

XPS - X-ray Photoelectron Spectroscopy - 10

Acknowledgements

I would like to thank my family and friends for their constant support and patience with my studies. In particular my wife for her love and encouragement, I would not be who I am without her, and my parents who have inspired and supported me.

To my supervisors, Prof. Keartland and Prof. Joubert, I would like to express my gratitude for their guidance. I would like to thank Dr. Rudolph Erasmus for his assistance with the Raman spectroscopy component of the thesis. I would also like to thank Ross McIntosh for his support with the electrical transport models and William Wright for his assistance and lengthy discussions in the laboratory.

Financial assistance for this research was provided by the National Research Foundation.

Financial resources and special study leave was provided by Picourseware towards the completion of this research.

A special thanks to the open-source communities which permitted the creation of the experimental equipment used in this thesis.

A peer reviewed journal article was published as a result of this study.

W.P. Wright, V.D. Marsicano, J.M. Keartland, R.M. Erasmus, S.M.A. Dube, N.J. Coville, The electrical transport properties of nitrogen doped carbon

microspheres, Materials Chemistry and Physics, Volume 147, Issue 3, 15 October 2014, Pages 908-914, ISSN 0254-0584,

Papers in a refereed conference proceeding resulting from the work described in this thesis are as follows.

V.D. Marsicano, W.P. Wright ,J. M. Keartland, R.M. Erasmus, S. Dube, N.J. and Coville, 'Characterisation of carbon microspheres using electron paramagnetic resonance spin-concentration techniques.', in Proceedings of SAIP2013: the 58th Annual Conference of the South African Institute of Physics, edited by Roelf Botha and Thulani Jili (2014), pp. 85 - 90. ISBN: 978-0-620-62819-8. Available online at http://events.saip.org.za

W.P. Wright, V.D. Marsicano, J.M. Keartland, R.M. Erasmus, S. Dube, N.J. and Coville, 'The Electrical Transport Properties of Bulk Nitrogen Doped Carbon Microspheres', in Proceedings of SAIP2013: the 58th Annual Conference of the South African Institute of Physics, edited by Roelf Botha and Thulani Jili (2014), pp. 199 - 204. ISBN: 978-0-620-62819-8. Available online at http://events.saip.org.za

J.M. Keartland, M.B. Dubuzane, V.D. Marsicano, N. Kunjuzwa, N.J. Coville, 'Characterization of nitrogen-doped carbon nanospheres using electron magnetic resonance', in Proceedings of SAIP2011: the 56th annual conference of the South African Institute of Physics (SAIP), edited by Ilsa Basson and André E. Botha, pp. 127 - 133. ISBN: 978-1-86888-688-3. Available online at http://www.saip.org.za

The equipment developed in this thesis was employed in the following peer reviewed journal article

F.K. Crundwell, A Van Aswegen, L.J. Bryson, C Biley, D Craig, V.D. Marsicano and J.M. Keartland, 2015, The effect of visible light on the dissolution of natural chalcopyrite (CuFeS2) in sulphuric acid solutions, Hydrometallurgy, 158, Pages 119–31

A mia madre

Contents

List of Figures

List of Tables

Chapter 1

Introduction

Carbon blacks and other forms of graphitic carbon have been studied extensively throughout the previous decades due to their applicability in industries, however it was not until the discovery of the carbon nanotube (CNT) [1] that the detailed nanostructure of the material was taken in to account. Since then, other carbon nanostructures have been synthesised such as the carbon nanohorn (CNH), carbon sea-urchins and carbon microspheres (CMS). These structures have spurred a great deal of research thanks to their potential industrial application.

While extensive studies have been conducted on CNTs some of the other structures have received less attention. The electrical and structural properties of CMSs have only recently been investigated with very few studies conducted on spheres doped with boron or nitrogen. Nevertheless they do present an interesting avenue of study due to their use in supercapacitor electrodes, lubricants and lithium-ion batteries.

Carbon microspheres can be produced in a variety of morphologies via a number of techniques. Spheres can be made either solid or hollow with other atoms introduced within the hollow sphere. Solid spheres are composed of graphitic flakes that can either form radially from, or concentrically to, the

centre of the spheres. The graphitic flakes have characteristic sizes and provide a large number of defect edges where chemical functionalization and reaction can occur. This highly varied set of morphologies provides an interesting avenue for tailoring some of the properties of the spheres and the relationship between the structural and electrical properties is not yet well understood. CMS growth mechanisms are still under investigation with a few models proposed for their synthesis.

This thesis presents a study of the electrical properties of nitrogen doped CMSs and the relationship with their structure. To this end, electrical transport measurements on bulk samples of CMSs will be discussed. The change in the resistivity as a function of temperature is used to determine which semiconductor model applies to these samples. The majority carrier species and the carrier density are determined using the Hall Effect. Equipment required to determine the electrical transport properties of the materials was built in the laboratory as part of this research. Labview code was developed to control and automate the data acquisition during the experiment. A digital multiplexer with an Arduino code enabled microcontroller was designed and built in the laboratory. This allowed computer control of the wire orientation in the test sample and control of the magnetic field direction during the Hall Effect experiment via a stepper motor. A motorised cryostat insert was designed to change the applied magnetic field direction on the sample during the Hall Effect experiment.

Electron paramagnetic resonance (EPR) spectroscopy is used to determine the behaviour of individual spins present in the samples, with an emphasis on the interaction between localised spin and carrier spin states. Finally Raman spectroscopy is employed to understand the changes that nitrogen incorporation introduces in to the spheres. A comparison between these varied experimental techniques will determine what relationship, if any, exists between the structural and electrical transport changes within nitrogen doped CMSs.

This thesis begins with a review of the relevant literature on carbon heterostructures with a focus on the experimental techniques employed. This is followed by a brief preliminary characterisation of the carbon spheres by XPS and SEM techniques. The experimental equipment and techniques are discussed in chapter 4 along with some overview of the laboratory built equipment. Chapter 5 contains the collection of the results of each experiment compartmentalised, while chapter 6 will draw the conclusions from a holistic overview of all the data. The appendices contain the details of the construction of the electrical transport station, and the computer code developed to control the experiment and process the data.

Chapter 2

Theory and literature review

This chapter will review the standing literature on carbon nanospheres (CNS). While there is a large body of knowledge on carbon nanostructures the carbon nanosphere has received less attention than carbon nanotubes or Buckminsterfullerenes. Some investigation into the properties of carbon nanospheres have been conducted due to their varied industrial applications. A discussion of the properties of CNSs and their synthesis follows here. A review of the theory governing the investigations performed as part of this thesis follows as well as some of the models used to understand the fundamental physics.

2.1 Carbon nanospheres

Carbon Nanospheres (CNS) are a subset of structured carbon systems such as CNTs, CFs and CNHs. Traditionally, the CNS has received less research attention than the CNT which has a highly ordered structure and low dimensionality. This has resulted in CNTs finding many industrial applications which in turn, has driven research in to other carbon nanostructures. CNSs have also found mechanical applications such as a strengthening additive,

electrical applications such as a cathode material in batteries [2] and capacitors as well as a pigment in inks.

CNSs is a term that describes a large range of spherical structures with varying sizes and morphologies. Unlike Buckminsterfullerenes [3] the CNS is not defined by a specific number of carbon atoms in a fixed arrangement. Rather, they are a conglomerate of graphitic carbon which can be found in many orientations and sizes depending on synthesis parameters [4]. Spheres can range from a few nanometres up to a micron or more. The term carbon microsphere (CMS) is used interchangeably with CNS. Spheres can be made hollow [5] or filled with a template material [6], well ordered or highly disordered and the graphitic layers which make up the spheres can either be arranged concentrically or radially with respect to the sphere centre [7]. Hollow spheres can also be made to contain a core of another material.

2.1.1 Synthesis methods

The most popular synthesis paths to produce CMSs are similar to the techniques used to produce many other types of structured carbon samples. The production of any particular type of carbon allotrope is determined by the synthesis parameters such as temperature, pressure, atmosphere, precursor flow rates and catalysts which will ultimately determine the carbon structure that will dominate. Carbon spheres were first produced in an arc discharge chamber used primarily to produce large quantities of CNTs. Alternative methods to the arc-discharge have arisen over the years including chemical vapour deposition (CVD) and laser ablation. Catalysts are often used in carbon heterostructure formation. However, some methods can reliably produce spheres without the use of catalysts. Synthesis of carbon nanospheres as recycling has been successfully investigated with the production of spheres by thermal decomposition of PET (Polyethylene Terephthalate), the material used in plastic soda bottles [8]. More recently alternative precursors have

also been investigated with CMSs successfully produced from pyrolysis of cooking palm oil [9].

Arc-discharge reactions involve the sublimation of a carbon anode creating a free carbon atmosphere. This is then cooled, in some designs with a water cooling system, to allow the carbon to condense back, creating many different types of structured carbons. Due to the abundance of carbon structures formed the system parameters must be modified to ensure that the desired structure is the most prevalent. Almost all types of carbon sphere can be produced in this way. A typical arc-discharge reactor is shown in Fig. 2.1. Alternative carbon sources have been used with this method including coal derived electrodes [10] and PET from recycled bottles [11].

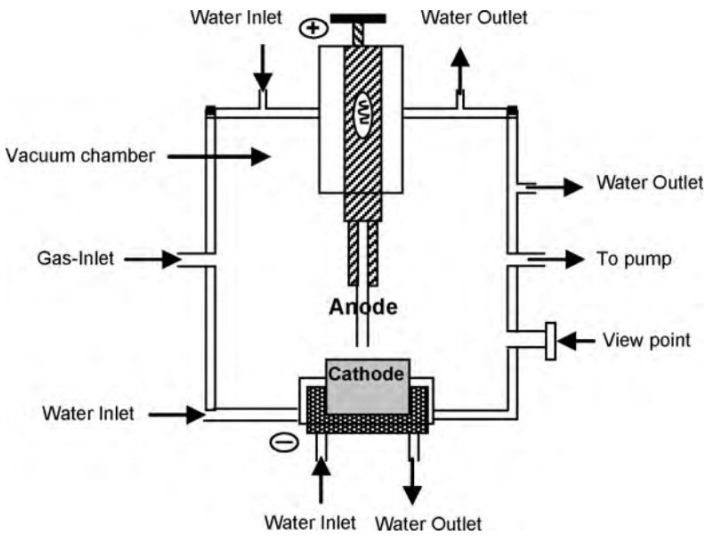

Figure 2.1: A diagram of the DC arc-discharge reactor used by He. et al to produce carbon spheres [12].

Chemical Vapour Deposition (CVD) is the technique employed to produce the samples investigated in this thesis. As such a brief description of this synthesis method can be found in Chapter 3. The technique involves the conversion of a volatile carbon source into a solid within a controlled environment. CVD can be conducted with or without the presence of a catalyst and can have many varying experimental parameters. The atmospheres of

the reaction can contain many different elements for doping like inert gases such as helium at varying pressures from vacuum to atmospheric pressure. This allows CVD to create many carbon structures with well controlled properties in respectable quantities.

Laser ablation is similar to the arc discharge technique however, in this case a carbon target is vaporised by a pulsed laser rather than a high current arc. The vapour is then allowed to float in a high temperature environment where the carbon structures begin to coalesce on the cooler surfaces. A water cooled surface may be provided to a growth site for the majority of the carbon.

2.1.2 Formation

A number of formation processes for carbon spheres have been proposed. Given that CMSs have such varying properties, it is likely that a number of different formation mechanisms exist to the creation of spherical carbon structures. Each determines the properties of the material. Generally CMSs are composed of graphitic carbon which has formed in to layers concentrically around a core of material.

The most commonly accepted synthesis path involves the formation and deposition of carbon flakes of different curvatures caused by the inclusion of heptagonal and pentagonal rings in a graphitic lattice [13]. This causes the flakes to have either positive or negative curvature as shown in Fig. 2.2. Kroto et al. [14] proposed that the centre of the sphere was nucleated by a pentagonal carbon flake which then experiences in-plane growth creating a smooth spiral. This provides an explanation for what causes smaller spheres, also known as carbon onions, [15] to present a smooth surface while larger spheres do not. The curvature of the larger sphere can only be achieved by mixing the flake curvatures of hexagonal and heptagonal rings [4]. The final structure of a common CMS is shown in Fig.2.3. Spheres with carbon flakes radiating from the core have not been studied extensively and their formation is yet to be modelled.

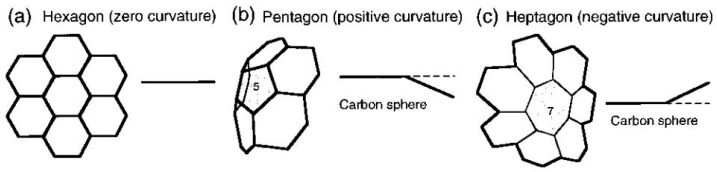

Figure 2.2: Graphitic flake curvature caused by different structures. a) Standard hexagonal structure is planar while b) Pentagonal and c) Heptagonal structures cause the flakes to curve as shown [13].

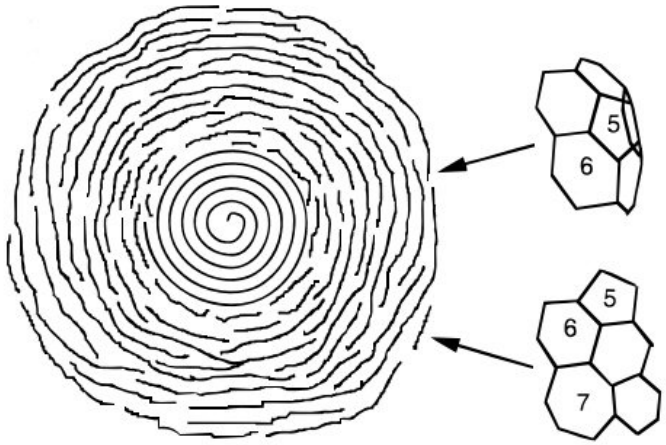

Figure 2.3: The final structure of the carbon sphere post synthesis showing the spiral core and the flake agglomerates on the surface [16].

2.1.3 Properties

A spheres' properties are highly dependent on the bonding configuration of carbon on the surface. These can be present as a complete graphitic shell or the outer layers can be formed by non continuous graphitic flakes deposited on a more structured core [17]. These flakes present crevices on the surface of the sphere and create a sphere with a much larger surface area and porosity. Given that the edges of graphitic lattices must present alternative atoms to fulfil the valence requirements, these flake edges are the location for many chemical functional groups. These are often OH or COOH groups as shown in Fig.2.4. However, other functional groups can occur especially in the presence of doping species. The presence of oxygen functional groups is

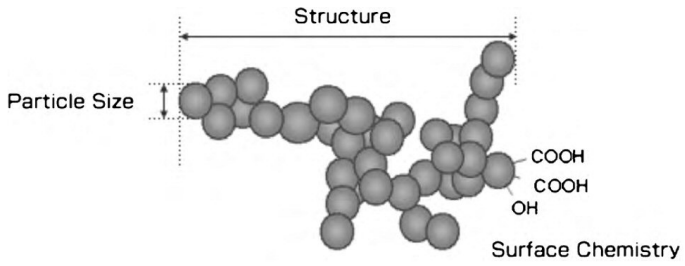

Figure 2.4: Spheres collect together in loose strings as shown due to van der Waals forces. The functional groups attached to the outer surfaces of the spheres are shown here [4].

corroborated later in this thesis by the oxygen content detected in the XPS data in Table 3.1. These functional groups contribute greatly to chemical properties of the spheres such as acidity, hydrophilicity etc. Larger spheres, due to the large number of disordered flakes on their surface, possess more chemical functional groups.

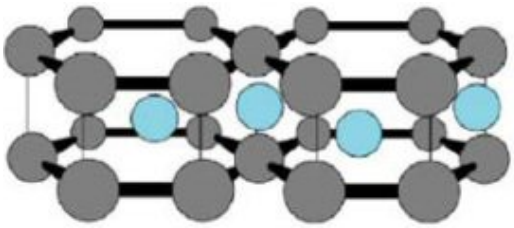

Figure 2.5: The doping element (blue) is found trapped between two layers of graphite (grey). It is not part of the graphite structure itself however its presence deforms the surrounding structure and increases the coupling between graphite layers. [17]

The behaviour of CMS can also be influenced by doping, with boron and nitrogen being the most common dopant species. Boron doping has been achieved by CVD synthesis with BF_3 as a boron source [18], [19]. NH_3 [20] and CH_3CN [21] are the most common precursors for synthesis of N doped carbon structures. A dopant can be added to the carbon structure during sample synthesis by addition of precursors to the reaction or post-synthesis by techniques such as ion implantation. The doping element can be included in to the sphere structure interstitially, where the doping atoms are wedged between the graphitic layers, such as is shown in Fig 2.5 or

by substitution, replacing a carbon atom in the lattice, such as quaternary nitrogen in graphite.

Of particular interest to this thesis is the doping of graphitic carbon lattices with nitrogen. N-doping can occur in four primary functional types namely pyridinic, pyrollic, quaternary and nitrogen oxides as shown in Fig.2.6. The type of nitrogen incorporation can impact on many physical and chemical properties of the carbon materials such as acidity and hydrophilicity [22] [23]. The presence of some of the dopants can cause distortions in the carbon lattice and promote pentagons and heptagons which, as has been discussed, are important components during the formation of carbon spheres [24]. Nitrogen incorporation can also cause an increase in the localised states around the Fermi level depending on weather the incorporation is pyridinic or graphitic [25]. This is due to the charge of the extra electron nitrogen contributes to a graphitic lattice over the carbon atom it replaces.

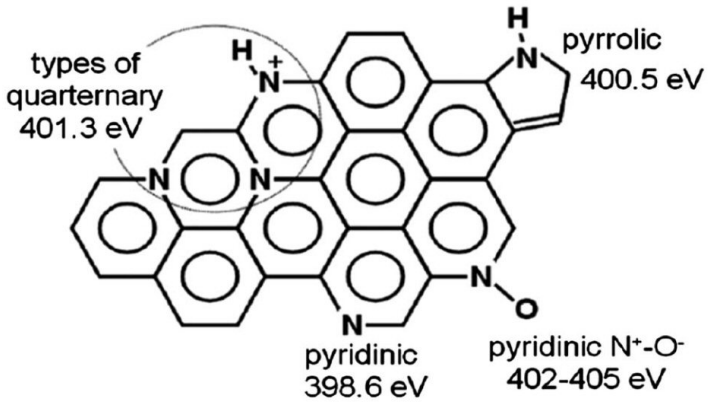

Figure 2.6: Common nitrogen doping structures found in graphitic carbon. The XPS binding energies are noted near their respective carbon bonds [22].

The consequences of nitrogen doping can be detected via Raman spectroscopy as each type of nitrogen bonding promotes the formation of different structures, along with increasing edge type defects. The D band in Raman spectra can be expected to increase given it's association with bond disorder arising from increased nitrogen incorporation [26]. The type of nitrogen bond can also have dramatic effects on the electron transport properties of the carbon

materials as each type of nitrogen incorporation site can influence the energy band gap of the semiconductor. Strelko et al [27] calculated the energy band gap change with varying nitrogen incorporation. Pyridinic carbon lattices had a band gap of ΔE 4.91 eV. Quaternary or graphitic nitrogen showed improved band gaps of ΔE 3.95 eV and ΔE 3.10 eV for "valley" and "centre" nitrogen positions respectively. Pyrollic nitrogen clusters reported a band gap of ΔE 2.98 eV and when combining all three types of nitrogen dopants band gaps as low as ΔE 2.88 eV were calculated. From this it is clear that the band gap is generally improved by nitrogen incorporation, an indication that samples with nitrogen incorporation will see the onset of thermally driven conduction at lower temperatures. This was also confirmed in a first principles study conducted by Huang et al. [28] where he investigated the effect of changing the placement of a nitrogen atom along the edges of a carbon lattice showing the quaternary nitrogen could push the density of states close to the Fermi level, increasing the mobility of charge carriers.

2.1.4 Applications

Carbon blacks have been used extensively in a number of industries taking advantage of their electrical, mechanical and pigment properties. CMSs represent a novel subset of carbon blacks with properties that can be modified to suit a particular application with relative ease. It is possible to manufacture CMSs in respectable quantities and with high purity.

Yuan et al [29] reported excellent specific capacitance of CMS electrodes highlighting their possible applications in electrochemical capacitors. The suitability of hollow CMSs as an electrode material was also investigated [30]. Due to the modularity of carbon nanomaterials, composite structures can be formed for example by grafting carbon nanofibres on the surface of a CMS creating a sea-urchin like structure [31]. This allowed Huang et al to report improvements to the electrode performance in double layer capacitors. Li et al [32] also reported improvements to electrode performance using a

hierarchical pore structure on the surface of CMSs. CMSs have found uses as fuel cell electrodes in methanol fuel cells [33] and proton exchange membrane fuel cells [34]. This is due to the improved access to Pt reactant in fuel cells over traditional carbon blacks.

Carbon spheres have been used in various battery technologies such as anode materials in Lithium-ion batteries [35]. They have also found use as a cathode material in Lithium-Sulphur [36] batteries and as an additive to $LiFePO_4$ cathode material [37].

CMSs have also found application outside their electrochemical properties. Their applicability as a strengthening agent in composites was investigated by Song et al [38] and similarly have been applied as an additive to rubber [39]. Carbon sphere in conjunction with gold nanoparticles have been used as detectors of protein markers to construct disposable immunosensors in biomedical applications [40].

2.2 Electrical transport

In this section the models for electrical conduction in CMSs will be discussed as well as the existing literature on conduction in disordered systems. The body of knowledge on the electrical properties of doped carbon spheres is limited, usually restricted to application specific research, however much more scientific research has been published on conduction mechanisms in CNTs. While the level of order in CNTs is usually higher, and the underlying theory more complete than in CMSs, they provide a starting point in understanding electron transport in bulk structured carbon samples. This appears to be especially true in bundles or mats of CNTs. Literature on other carbon structures will also be discussed.

2.2.1 Electrical transport in carbon allotropes

After the publication of Iigima's [1] description of carbon nanotubes, many research papers have been published concerning their electrical properties. CNTs have varying electrical properties depending on their structural arrangement. They can present metallic or semiconducting behaviours depending on the vector at which the graphene, which is rolled to form the tube, is cut. This vector is called the chiral vector and determines the chirality of the tube. Electron transport in individual tubes has been investigated extensively. A single electron can complete resonant tunnelling through the length of the tube in regimes of very low bias [41]. CNTs have also been found to exhibit behaviour consistent with a Luttinger liquid [42], where the weak Coulomb interactions are significant in a 1D system. In certain regimes, CNTs also demonstrate ballistic transport [43] where an electron will travel the length of the tube without scattering at all allowing for current densities greater than 10^7 A.cm^{-2}. These basic properties of carbon nanotubes can also be tuned by doping [44] [45].

While individual CNT studies provide insight into the conduction models which govern structured carbons in general, the size and disorder in larger samples of CMSs are more closely reminiscent of bundles or mats of carbon tubes. These mats share many properties with large CMSs. Structurally they both possess non-uniform graphitic zones with different curvature and spacing all competing for conduction. Low temperature conduction measurements performed on bundles of CNT fibres revealed competing conduction phenomena [46] with classical Variable Range Hopping (VRH) [47] dominating at temperatures lower than 80K and Fluctauation Assisted/Induced Tunnelling (FAT) at higher temperatures [48]. In the same paper magnetoresistance measurements revealed both positive and negative magnetoresistance depending on the strength of the magnetic fields. Both conduction regimes have been detected in doped carbon nanotube mats [49] and the temperature dependence displayed an irreversibility at temperatures greater than 300K in [50]. This annealing resulted in a "U" shaped resistivity curve

associated with an increase in resistivity with desorption of dopants. One dimensional metallic conduction models have also been detected [51] [52] [53] in CNTs which provided an alternative explanation for the "U" shaped resistivity. A study conducted on boron doped carbon horns found that VRH was the dominant conduction mechanism and the researchers postulated that the change in conductivity due to doping was due to an increase in the available states at the Fermi level [54].

Conduction mechanisms in carbon spheres are still under investigation, usually in the context of their application as electrode materials. Recent studies showed that the conductivity of carbon nanospheres produced by annealing of nanodiamond particles was dominated by VRH at low temperature while FAT was dominant at temperatures greater than 130K [55]. Romanenko et al [56] showed that samples synthesised in a similar manner to the Macutkevic study displayed different regimes of VRH behaviour with the Coulomb gap playing a significant part in the conduction paradigm at very low temperatures and the classical VRH at higher temperatures. The type of annealing also played a role in determining at which temperature the Coulomb effect set in, indicating a structural influence on the conduction mechanism. Changes to the localisation of charge carriers was shown to change with doping [57]. El Mir et al [58] confirmed that the pyrolysis temperature affected the conduction paths in spherical structured carbons when produced from pyrolysis of xerogels. B-doped CNSs were produced via CVD and investigated by Mondal et al [59] revealing that Boron doping promoted p-type semiconducting behaviour. In these samples hopping conductivity was dominant with Boron incorporation reducing the conductivity of the samples with possible decrease in the density of hopping sites due to Boron substitution. Previous work on nitrogen doped samples produced by CVD by Wright et al [60] showed a preference for FAT conduction in nitrogen doped samples and the presence of metal insulator transition. In that study the effect of the nitrogen doping on the absolute value of the resistivity was not reported and is one the primary subjects of this thesis.

2.2.2 Theory of conduction Models

Given the dominance of VRH and FAT in the literature explaining the electrical conduction in systems of structured carbon that possess some intrinsic disorder, such as CNT mats or large carbon spheres, those models are likely to be present in the CMS samples under investigation. The data collected will then be tested against these models to their applicability to the carbon microspheres. Experimental results obtained in this work were collected with constant voltages therefore all the models investigated will concern DC conductivity only.

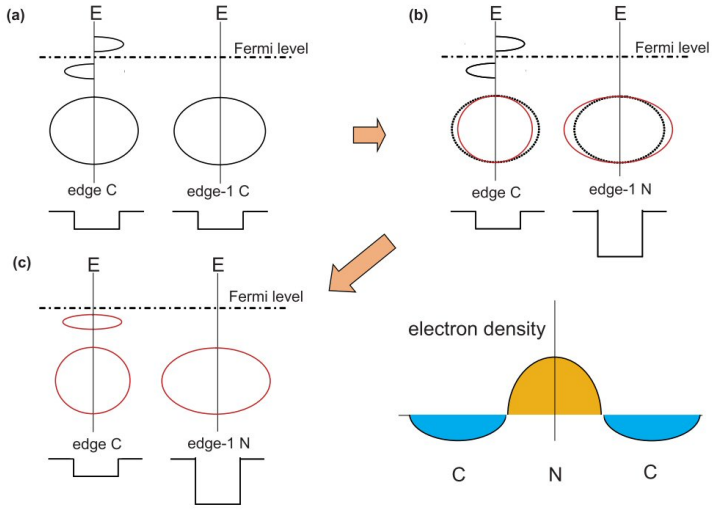

Figure 2.7: The diagram from Huang et al [28] showing the localisation effect of quaternary nitrogen in a carbon lattice. The nitrogen attracts the electron wave function around its site, reducing the free movement of the electron around the carbon ring.

Carbon blacks composed of collections of structured carbon that are doped can be considered to contain two types of disorder. The first type, is a structural disorder of the system itself contributed by the random arrangement of surface flakes and the random distribution of dopant ions either intercalated between the lattice or within the lattice in a number of functional types. The second, is the amorphous nature of the sample as a whole with its random distribution of spheres influenced by the packing pressure, alternative carbon

nanostructure contaminants, humidity etc. Disordered systems of these types give rise to localised electron states by trapping the electron wave functions within regions of low potential energy distributed randomly throughout the material. This is also known as Anderson localisation and is the basis for understanding some of the hopping models which follow. For example the localisation caused by quaternary nitrogen in a carbon lattice aggregates the electron wave function around it, reducing the mobility around the hexagonal rings of carbon as shown in Fig. 2.7 [28]. Alternative localisation could be caused by large scale structure such as electrons unable to cross from one sphere to another due to the low packing factor of spheres. When electrons are strongly localised in this way they are restricted to potential energy boxes at the disorder site. Each site may present a different amplitude and shape determined by the type of disorder at a given location. The probability of movement between localised states is affected by local potentials, total energy of the electron and distance between sites. Disorder density would also therefore be strongly correlate with the electrons overall ability to traverse the bulk of the sample.

Hopping conduction

When electron valence states lie below the conduction band and the states at the Fermi energy are localised, conduction can occur in two possible ways. Electrons in these states can be excited thermally to the conduction band and be free to conduct or electrons can receive enough thermal excitation to hop to a neighbouring energy state but not enough to reach the conduction band. Both these mechanisms are strongly dependant on temperature and should each be dominant in different temperature regimes. The following derivations are based on the work presented by Bottger, H. and Bryksin, V.V. [61].

Nearest neighbour hopping The initial formulation of hopping conduction was based on ideas developed in percolation theory. An electron in a localised state can access empty localised states by hopping to them. One of the factors determining the energetic cost of hopping to another state is the distance between states. It was originally considered likely that all hopping occurred only to the immediately neighbouring states. The current density in such a model is given by:

$$\boldsymbol{j} = \frac{1}{2e\Omega} \sum_{mm'} (\boldsymbol{R}_m - \boldsymbol{R}_{m'})(U_{m'} - U_m) Z^{-1}_{m'm} \tag{2.1}$$

$$Z_{m'm} = \frac{kT}{e^2 \Gamma_{mm'}} \tag{2.2}$$

$\Gamma_{m'm}$ has dimensions of resistance which implies $Z_{m'm}$ defines a relationship between resistance and hopping probability. Ω represents the total system volume and R_m and U_m are the position and electrical potential at site m. If the system is well ordered the internal potential energy is a simple function of position to the externally applied field. The defining equations illustrate the impact of the field present at the hopping sites via U_m and the importance of thermal energy via the kT term in $Z_{m'm}$ in determining the final current density. The system is bound by the rate equation which in this scenario is equivalent to Kirchoff's current law, where all possible hops through site m must sum to 0.

$$\sum_{m'} (U_{m'} - U_m) Z^{-1}_{m'm} = 0 \tag{2.3}$$

Miller et al [62] determined that the system could be understood as a random resistor network with a potential applied at each end. The hopping probability is analogous to the resistance of each element in the resistor network, with junctions of higher probability allowing more electrons to complete the hop

in the same manner as lower resistance resistors allow a greater proportion of the current to pass.

The expression for hopping probability is a complex function composed of the Fermi function, the frequencies of the phonons at each site, the energy levels of each site and the phonon-electron coupling [61]. Some simplifications can reduce the complexity of the problem. If the phonon coupling is kept weak and we only consider a single phonon and we further consider the low temperature limit, the hopping probability is given by [63]:

$$Z_{m'm}^{-1} = Z_0^{-1} e^{-2\alpha|\boldsymbol{R_{m'm}}| - \frac{1}{2kT}(|\epsilon_{m'}-\mu|+|\epsilon_m-\mu|+|\epsilon_{m'}-\epsilon_m|)} \tag{2.4}$$

Where ϵ and μ are the energy state and Fermi level energy at the m^{th} position. Z_0^{-1} is considered to have only a weak dependence on $\boldsymbol{R}_{mm'}$ and $\epsilon_{mm'}$ making it largely a constant with respect to the positions and energies of the hopping sites. The initial path taken to solve for the resistor network proposed by Miller and Abrahams [62] was to assume that the largest contributor to the energy requirement for hopping was the distance element $\boldsymbol{R_{m'm}}$ rather than the energy levels at the neighbouring states. The path options through the network were reduced by taking only the paths that minimised the energies between the two electrode ends, minimising the impedance of the paths, which selected out the paths that were generally favourable for current flow and parallel to the electric field lines. The average conductivity can then be written

$$\sigma = C_0 e^{-f(N)} e^{-\frac{\epsilon_{activ}}{kT}} \tag{2.5}$$

This final expression for the nearest neighbour conduction regime contains two important quantities. ϵ_{activ} is the energy required to activate the conduction or the energy consumed in completing the hop to the neighbour energy state. $f(N)$ is a function dependant on the choice of critical path

and depends on the concentration of localised states involved in the hopping transport. The exact form of $f(N)$ is determined by the choice of path taken through the material modelled as a continuous random network [61]. C_0 is a temperature independent constant.

Variable Range Hopping While the previous approach does solve the problem of the resistor network, calculating the conductivity with the strict requirement that hops only occur to immediately neighbouring sites is not the only process found in nature. Mott [64] proposed that an electron would choose to hop to a site further away if the hop was energetically favourable i.e. the hopping distance could be variable. If hopping occurs at energy levels around the Fermi level we can reduce the Eqn. 2.4 to:

$$Z_{m'm}^{-1} = Z_0^{-1} e^{-2\alpha|\boldsymbol{R_{m'm}}| - \frac{|\epsilon_{m'm}|}{kT}} \tag{2.6}$$

Mott et al [64] showed that in a given volume, at least one pair of sites must exist with energy E above the Fermi energy level, we can use the following condition:

$$\frac{4\pi}{3} R^3 \int_{\mu}^{\mu+E} N(E')dE' = 1 \tag{2.7}$$

Combining Eq 2.7 with an attempt to minimise the exponent in Eqn. 2.6, we can derive a R_{min} which is the minimised hopping distance. If we are still considering hopping near the Fermi level μ then it can be assumed that the density of states at the Fermi energy is largely determined by the Fermi energy itself and not the small energy element E'. If we also assume the density of states is constant around the Fermi energy we can then replace $N_{E'}$ with N_μ in expression 2.7. Solving for E in Eq 2.7 then allows one to replace $|\epsilon_{m'm}|$ in Eq 2.6 with an expression dependant only on R. After some minimisation we recover the three dimensional Mott VRH law.

$$\sigma = \sigma_0 e^{-\left(\frac{T_0}{T}\right)^{1/4}}, \tag{2.8}$$

Where

$$T_0 = \frac{c_3^4 \alpha^3}{kN(\mu)} \tag{2.9}$$

Here T_0 is called the characteristic temperature and is a function dominated by the density of states at the Fermi level. c_3 is a constant with respect to temperature and has been calculated for different dimensionality of the Mott VRH equation. Finally, σ_0 is also a temperature independent constant. This shows that the temperature dependence of conductivity is a marker for VRH conduction. The Mott VRH formula has been derived generally for any dimensionality of the system as follows:

$$\sigma = \sigma_0 e^{-\left(\frac{T_0}{T}\right)^{1/d+1}} \tag{2.10}$$

The above derivation also be considered as a nearest neighbour hopping process in a four dimensional space where the distance vector $\boldsymbol{R}$ is composed of three spacial coordinates and an energy coordinate. While many assumptions were made during this derivation the formalism was found to be valid even in more relaxed paradigms such as with moderate phonon interactions.

Efros-Shklovskii VRH One of the approximations made thus far that has not been addressed is that the electron-electron Coulomb interaction. In 1975 Efros and Shklovskii [65] pointed out that this interaction could introduce a gap in the available states around the Fermi level, which was previously assumed to be constant. The modification to the conductivity in such a system is as follows:

$$\sigma_{ES} = Ce^{-\left(\frac{T_0}{T}\right)^{1/2}} \tag{2.11}$$

Where C is again a temperature independent constant and T_0 is the characteristic temperature. While this may appear to be the classical VRH formula for a single dimensional system this formula would hold true for a system of any number of dimensions.

Fluctuation Assisted Tunnelling Fluctuation assisted tunnelling (FAT) or sometimes called fluctuation induced tunnelling (FIT) is a mechanism of conduction which is also dependant on thermal excitation of electrons. While localisation in the VRH model is considered as distinct points within the sample which hold hopping electrons in FAT the localisation is not as rigidly defined. The sample is modelled as zones of conduction and insulation with electrons free to move over both areas when thermal energy is sufficient to allow them to surmount the energy barriers [66]. In situations where the thermal excitations are not large enough, the electrons conduct normally in the conductive areas but must quantum tunnel through areas of insulation. It regards the whole conduction as an average function of all the smaller segments and as such does not have a strictly defined scale. In comparison VRH is only possible if the minimum hop length is not larger than the lattice in which the hopping occurs. In this system the resistivity is given by:

$$\rho(T) = \beta e^{\left(\frac{T_b}{T_s + T}\right)} \tag{2.12}$$

Here β contains information regarding the height of the insulating barriers and their geometrical placement. It is approximated as constant with respect to temperature. T_s is considered to be the critical temperature at which thermal fluctuation begin to give a significant portion of the conducting electrons enough energy to overcome some of the insulating barrier heights. T_b is constructed from the energy profiles the electrons must tunnel through i.e. the barrier shapes, heights and any impact local electric field may have on those barriers. This equation shows that a particular temperature dependence of

the conductivity can be used as a signature that this process is determining the conductivity of a sample.

2.3 Raman spectroscopy in carbon

The Raman spectra of carbon allotropes have been studied extensively as this technique is a quick and non-destructive way of determining structural properties of a large number of carbon allotropes. Raman spectra have been used to determine the diameter of CNT [67] and the graphitic structures of MWCNT [68]. In cases where there is little structural differences between samples, Raman spectroscopy has been used as an indication of chemical functionalisation [69] or of doping [70]. It has been used to probe the properties of graphene since its discovery [71] and it can also be used to determine the degree of graphitization in any carbon allotrope, including spheres [72]. A decrease in size of carbon spheres was detected by Raman Spectroscopy by a blue-shift of spectral elements [73]. Variation in the size of spectral elements was used to show the greater disorder caused by Boron doping of CMSs [59]. Kim et al showed how annealing at high temperatures can improve the structure of MWCNTs showing the definition of the spectral elements improved as the tubes became more ordered [74]. Micro Raman has been used to confirm the number of layers present in a graphene sample and the presence of defects or dopants in specific parts of a graphene sample [75].

2.3.1 Origin of Raman spectral elements

The Raman spectra for all carbon allotropes are dominated by two peaks, namely the D and G peaks, found around 1355 cm^{-1} and 1581 cm^{-1} respectively. Vidano et al [76] associated the G peak with the bond stretching of carbon sp^2 bonds. This vibrational mode has E_{2g} symmetry which involves every second atom in a chain vibrating in the opposite direction to the first

and third as shown in Fig. 2.8. This mode can also exists in rings with each side of a ring behaving as a chain 180^o out of phase to its neighbour.

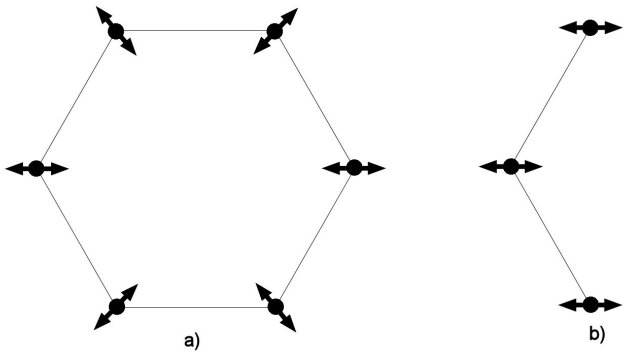

Figure 2.8: The most prominent vibrational modes for graphitic carbon lattices with a) the A_{1g} mode giving rise to the D peak and b) the E_{2g} mode responsible for the G peak.

As shown in Fig.2.8 the D peak arises from a A_{1g} vibrational symmetry mode which involves entire rings of carbon atoms and is also referred to as a breathing mode. This mode is not possible in a perfect graphite lattice and is therefore governed by the presence of defects in a carbon sample. The origin of the D peak has been the subject of much debate in the literature with a number of models proposed such as; a relaxation of phonon selection rules [77], a resonance coupling of a phonon wave vector with an electron transition [78] and a resonance involving the long range polarization of $\boldsymbol{\pi}$ bonds [79]. The D peak has been shown to be dispersive, with its magnitude dependant on Raman laser excitation energy as shown in Fig. 2.9.

The intensity of the D peak was shown to be dependant on the crystallite size [77] by comparison with X-ray data. This work was further developed to determine a general equation relating the crystallite size to I(D)/I(G) ratio by Cançado et al [80] shown as in Eqn. 2.13 which takes in to account the dispersion of the D peak vs incident Raman energy, and therefore wavelength. This equation is valid up to L_a values of 2 nm where the rings themselves begin to disintegrate. From this point, Ferrari et al propose an alternative

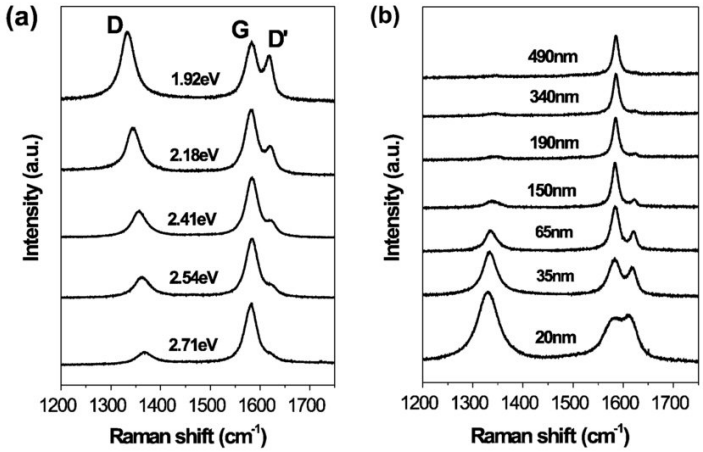

Figure 2.9: This figure from Cançado et al [80] shows the dispersion characteristics of the D peak with a) the change in D peak intensity vs Raman photon incident energy and b) the increased presence of the peak with decreasing crytallite size.

relation for the intensity ratio to crystallite size [79]. Pimenta et al [81] also showed how edges of graphitic lattices contribute to the D peak's intensity by providing areas where the breathing modes are present, implying that samples of similar size but made up of smaller pieces will present larger D peaks.

$$L_a = (2.4 \times 10^{-10})\lambda_l^4 \left(\frac{I_D}{I_G}\right)^{-1} \tag{2.13}$$

2.3.2 Evolution of spectral elements with structure

The evolution of Raman spectra for carbon allotropes was discussed in a review article by Ferrari et al [79] which forms the basis for the following analysis. In the review paper the collated work of Raman spectra of various carbons was analysed to produce a map of the changes to the elements of Raman spectra as samples of carbon change from perfect graphite through amorphous forms to fully diamond like sp^3 bonded carbon. The primary

elements that influence the Raman spectra, apart from what has been previously discussed, are the bond disorder, the quantity of sp^2 bonds which are collected in chains vs rings and the ratio of sp^2 bonded carbon vs sp^3 bonded carbon. The various elements compete simultaneously to affect the Raman spectrum as shown in Fig. 2.10.

While sp^3 bonded carbon moves the G peak position to lower Raman shifts, the clustering in the sp^2 and the increased number of non-hexagonal rings pushes it to higher shifts. The first stage in the transition from a graphitic lattice to a diamondlike one is changing graphite into nanocrystalline graphite, usually via breaking of graphitic lattices into smaller and smaller pieces. As discussed previously this creates smaller crystallite areas which themselves possess more edges, all contributing to the formation and growth of the D peak. As the crystallites are still generally large, the general Eqn. 2.13 is valid. At this stage no sp^3 bonds occur yet and the structure is largely still well ordered. Higher order phonons create a small D' peak at around 1620 cm^{-1} which, if not easily distinguishable from the G peak, appears as an upwards shift of the G peak.

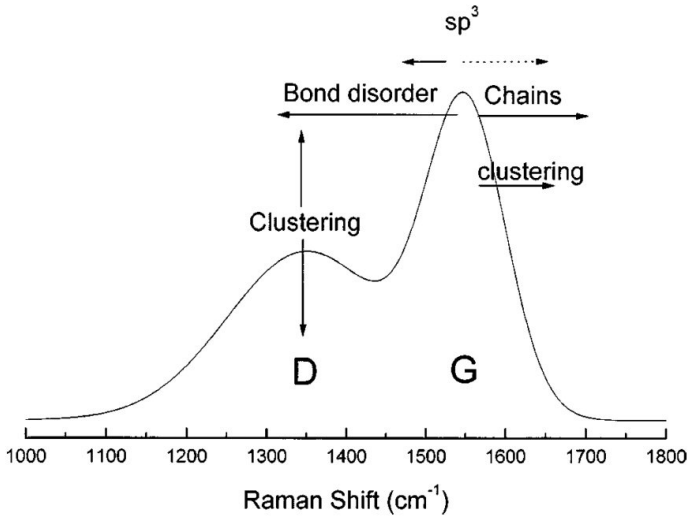

Figure 2.10: The effect of various structural changes in the sample on the primary Raman spectrum features. sp^3 bonds cause competing changes in the G peak position as marked. [79]

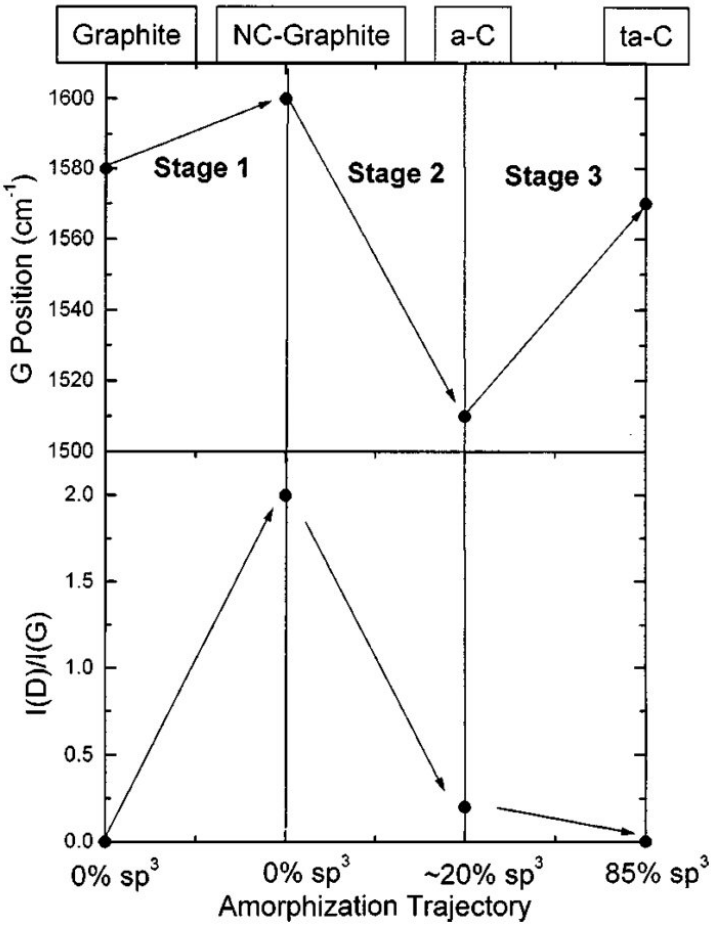

Figure 2.11: The trajectory of the I(D)/I(G) ratio and G peak position with greater levels of amorphitization [79].

The second stage of the process introduces greater disorder in the system. Crystallite sizes continue to shrink to the point that this process begins to break the rings in which the A_{1g} vibrational symmetry mode is created, lowering the D peak. Non hexagonal rings begin to form causing the density of vibrational states (VDOS) to no longer be that of graphite throughout the sample. sp^3 bonds begin to appear in limited numbers further reducing the sites that form the D peak. The chains formed by sp^3 bonding however retain their E_{2g} vibrational symmetry mode and therefore the G peak intensity does not change. Consequently the I(D)/I(G) ratio shrinks. As shown previously carbon spheres are likely to be found in one of these two stages

as stage 3 is characterised by a complete loss hexagonal rings and therefore a disappearance of the D peak which is not generally detected for carbon spheres.

2.4 Electron Paramagnetic Resonance

Electron Paramagnetic Resonance (EPR), also termed Electron Spin Resonance (ESR), is a non-destructive technique that can be used to probe the properties of unpaired electrons in a lattice. Information such as the proximal lattice structure and chemical composition, as well as some information regarding the electron's mobility can be exacted from EPR spectra. The following subsection will contain a brief description of the origin of EPR spectra, the interpretation of spectral elements and finally some of the spectra detected in carbon allotropes. While a great many spectral elements are possible the discussion will be restricted to elements detected in this study.

2.4.1 Origin of EPR spectra

Electrons possess an intrinsic quantum number described as spin angular momentum generated by the particle spinning about its own axis. This gives rise to an intrinsic magnetic moment for the electron defined by the g value g_e, the Bohr magneton μ_B and the spin of the particle $\boldsymbol{S}$.

$$\mu_e = -g_e \mu_B \boldsymbol{S} \tag{2.14}$$

If we apply an external magnetic field, $\boldsymbol{B}$ to the sample we know that in general the energy of the particle is described by $E = -\boldsymbol{\mu} \cdot \boldsymbol{B}$ and in quantum mechanical terms is given by the spin Hamiltonian.

$$H = g_e \mu_B \boldsymbol{S} \cdot \boldsymbol{B} \tag{2.15}$$

The direction of the magnetic field defines the z-axis of the angular momentum.

$$E = g_e \mu_B B M_s, M_s = \pm 1/2 \tag{2.16}$$

This results in two energy levels at either $+1/2$ and $-1/2$. Physically it can be understood as a breaking of the degeneracy of the energy level occupied by the unpaired electron. The magnetic field differentiates between its spin being either parallel or antiparallel to the field. The difference in the energy levels and therefore the energy of a photon required to cause the electron to switch from the low to the high energy levels is then given by:

$$\Delta E = h\nu = g \mu_B B \tag{2.17}$$

The incidence photon of the resonant energy can promote an electron from the lower parallel spin to the higher antiparallel spin. If this occurred continuously the sample would saturate when all the spins are promoted and any EPR effect would cease. In practice the spins return to the lower energy level by interacting with the surrounding nuclear lattice. This characteristic time is defined as spin-lattice relaxation time T_1. Alternatively the electron can interact with the other spins in the system around it, characterised by a spin-spin relaxation time T_2. These two mechanisms compete simultaneously in a sample. In most cases, especially at room temperatures, $T_2 << T_1$ which means the spin-spin interaction is more likely to occur before the lattice interaction. T_1 can be significant in certain orientations and at lower temperatures. The direct impact of the spin-spin relaxation time is on the line width of the EPR spectra as will be discussed in the following section [82].

In an equilibrium, the spin population in a sample is divided between the high and low energy states by the Boltzmann distribution:

$$\frac{n_{\uparrow}}{n_{\downarrow}} = e^{-\frac{h\nu}{k_B T}} \tag{2.18}$$

This population distribution is contingent on the relaxation mechanism having sufficient time to re-equilibrate the populations post excitation. If sufficient power is applied to the ensemble of spins the number of photons incident on the spins does not permit a sufficient number to return to the lower energy state. In this case a greater and greater proportion of spins are not available for re-excitation with increasing microwave power, causing the EPR signal to saturate. This is known as a power saturation and the onset of saturation is dependant on the number of spins available and their relaxation rates.

A number of real world situations do complicate the spectra. Firstly samples may not be isotropic, creating a much more complex spin Hamiltonian for the system wherein the previously isotropic g-value is replaced with a $\boldsymbol{g}$ tensor. This implies the orientation of a particular crystal affects the EPR spectra. Further complication can occur if the sample is not a single well ordered crystal but a powder where many different crystallite orientations are present. The resulting signal is an averaging of all possible EPR signals emanating from the sample's various orientations. This powder averaged signal will hide any hyperfine interactions or other detailed features of the signal in a single broad peak. Given the powder nature of the samples and their concentric spherical arrangement CMSs generate an averaged EPR signal.

2.4.2 EPR Spectral Elements

The primary spectral elements of interest in this thesis will be linewidth of the signal, the amplitude and the g-value. Another important factor is the A/B ratio as defined by Feher et al [83] which is indicative of surface

conduction electrons and characterises a Dysonian line shape. While many other spectral elements exist such as hyperfine splitting these elements were not detected in the samples investigated. Powder samples, such as those studied here, do not produce discernible hyperfine spectral elements because of the random orientations of their crystal elements to the magnetic field. In recent years alternative definitions have been developed to attempt to include all the elements of an EPR signal in to a single parameter such as the R_{10} parameter [84]

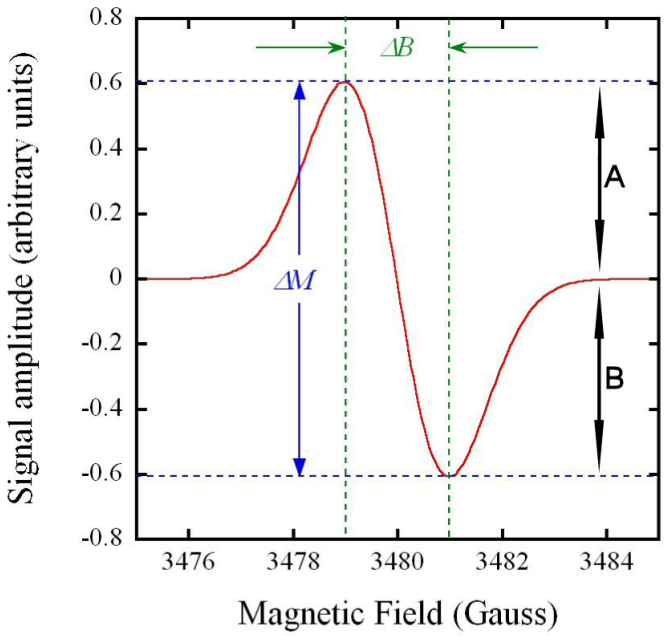

Figure 2.12: An example of an EPR spectrum showing the line width ΔB and the amplitude ΔM.

The amplitude of the EPR peak ΔM is indicative of the total signal strength. It is dependant on many factors relating to the experimental apparatus, and the calibration of the spectrometer itself. If these are controlled and kept constant along with temperature it can be used to approximately determine the relative concentration of paramagnetic spin sites. This is accomplished by comparing its change with incident radiation power, essentially retaining a linear relationship until saturation occurs. Samples with greater number of spins will require greater numbers of incident photons to saturate the

sample. If measured with a fixed microwave power and varying temperature it can indicate a change in dominant relaxation mechanism as relaxation times change with temperature the signal size may change due to saturation effects.

ΔB is the line width of the EPR signal and is determined by the spin-spin relaxation time of the system. A shorter T_2 results in a narrower peak. In the case of changing temperatures different relaxation mechanisms may dominate in different temperature regimes causing large changes to the relaxation time. It is also an indication of electrical conductivity when combined with the A/B parameter.

The asymmetry of the first derivative peak A/B is a useful parameter in defining the quantity of spins that are involved in conduction. The asymmetry was associated with the diffusion time, τ_D, of the surface electrons. The EM field only penetrates the conductor to a thin skin with defined thickness δ known as the skin-depth. τ_D is then defined as the time taken for the excited spin to diffuse through this skin and is a component of the total relaxation time of the electrons [85].

The g-value is the proportionality constant between the incident photon energy and the energy difference in the split degeneracy levels. This proportionality is fixed for a free electron $g_e = 2.002319304$ and can vary depending on the chemical environment surrounding the excited spin state. This is because the spin state is sensitive to the local magnetic field, and not just the applied external field. All the spins surrounding the electron can align with or against the external field, inducing fields of their own which are characteristic to the chemical identity of the surrounding particles and their particular binding.

2.4.3 EPR studies in carbon

EPR studies of Carbon were conducted before the discovery of nanostructured carbons. Early studies on carbon blacks by Mrozowski developed the understanding behind the effect of doping using EPR spectra, with neutron implantation [86] and Boron diffusion [87] being the primary techniques employed. These studies showed that doping can, in the case of boron, initially replace the de-localise electron states and push the g-value of the system towards the free electron g-value. It was understood that the single EPR signal collected was a compound signal formed by the mixing of the localised and conduction electron spins. Some studies included the effect of impurities in carbon during annealing, revealing a broadening of the EPR curve as the carbon samples were annealed to temperatures above 1600^{o}C [88].

Given its high sensitivity, EPR techniques allows analysis of very small quantities of sample in a non-destructive manner, a feature which can be important when sample synthesis methods are not particularly fecund. Beuneu et al [89] showed how CNTs possessed a high resistance to electron radiation. Despite the low number of radiation induced defects, the sample developed a marked change in the EPR signal, heralding a large impact on the Fermi level. Similarly to the carbon blacks, annealed CNTs showed the g-values are approximately equal to the free electron g-value at all temperatures. Spin localisation over non-annealed tubes was more evident at low temperatures showing how defects are responsible for spin localisation [90]. The presence of boron also enhanced the conduction of spins in CNTs and fixed the g-value approximately to the free electron g-value. This was also indicative of an increased density of states at the Fermi level, and a commensurate increase in the thermally induced conduction [91]. The EPR signal of other structured carbons was used to confirm the successful growth of long carbon filaments, also known as sausages, by Pol et al [92]. A more complete description of EPR spectra of SWCNTs was completed in 2007 showing such features as detection of itinerant spins at low temperatures via relaxation time analysis, possible superconduction in CNTs at temperatures below 12K and a spin

concentration of $6 \times 10^{18} g^{-1}$ or equivalent to 8×10^{-4} spins per carbon atom in the lattice [93].

EPR studies involving carbon spheres have been limited. Dubuzane et al [94] reported that in nitrogen doped CMSs the presence of two competing relaxation processes, namely EY (Elliot-Yafet) and DP (D'yakonov-Perel) relaxation, occurred simultaneously throughout the temperature range. Spin concentrations in samples with known dopant concentration were used to coarsely calibrate an EPR spectrometer [95]. This calibration procedure was then used in determining the dopant concentrations in samples investigated by Wright et al [60]. EPR measurements on CVD synthesised CMSs showed a strong Dysonian lineshape with g-values close to the free electron value, indicative of large quantities of conduction electrons. Furthermore the linewidth of the EPR spectra increased with decreasing size, indicating longer relaxation times for smaller spheres, likely caused by a decrease in the number of defects in the surface carbon lattice [73]. Spheres generated by PET waste also displayed g-values and lineshapes similar to the doped samples possibly indicating a large number of dopants present as contaminants during sphere synthesis from these recycled materials [8].

Chapter 3

Sample Synthesis and Characterisation

This chapter contains a brief description of the synthesis of the samples under investigation performed by Sibongile Dube in the School of Chemistry at the University of the Witwatersrand during her postgraduate studies under the supervision of Prof. Neil Coville. Further details of the synthesis procedures can be found in the literature [96]. The samples were characterised in the school of Physics with Electron Microscopy to confirm that carbon spheres had been successfully produced and to determine their morphologies.

3.1 Sample synthesis

The carbon microsphere samples were created using a horizontal CVD reaction chamber. This technique is popular due the high yield and purity of the product [4]. The experimental parameters require an extensive tuning to select a particular carbon allotrope for growth. If experimental parameters are not accurate growth of alternative carbon allotropes such as carbon

nanotubes as well as large quantities of amorphous or loosely structured carbonaceous material can occur.

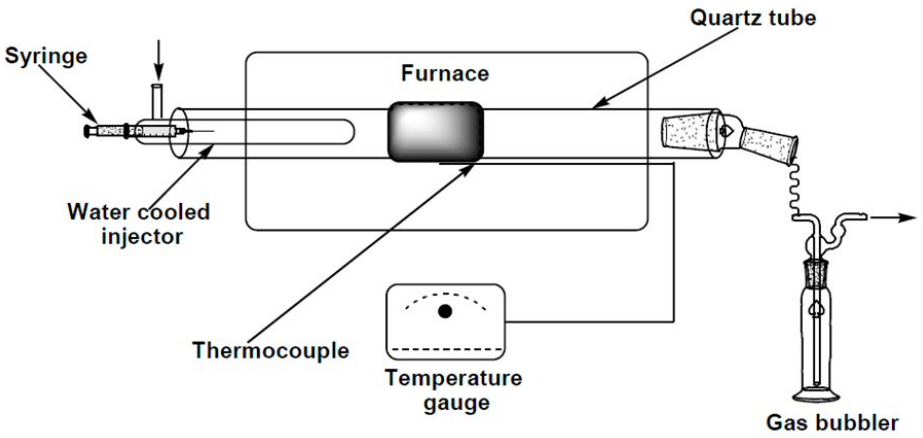

Figure 3.1: Diagram showing the primary elements of a horizontal CVD reactor.

In a horizontal CVD reaction a neutral carrier gas is used to flush out the reactor of residual atmosphere prior to the precursor gases being introduced. Precursor gas flow is allowed to enter the carrier gas stream prior to entering the reaction chamber. The precursor gases, in our case acetylene and acetonitrile, are then allowed to react in the chamber via pyrolysis. Synthesis occurred at 900^{o}C and the acetylene flow rate was set to 100 ml/min for a duration of 2 hours. Varying quantities of acetonitrile were used to dope the spheres during growth over four runs producing the four samples studied here.

3.2 Characterisation

Characterisation techniques employed below were used to determine the quality of the samples produced in the CVD reactor. Reaction products are primarily a light and black powder which has a tacky quality. It holds a shape when compressed and adheres to instruments due to electrostatic forces.

3.2.1 Scanning electron microscopy

Scanning electron microscopy (SEM) is a technique which creates images of the surface of a sample by bathing it in electrons and collecting secondary electrons emitted from the surface. The secondary electrons carry topographical data which can be used to create a micrograph of a sample. In Fig 3.2 the images used primarily in determining the character of the spheres are shown.

The low nitrogen samples are primarily made up of medium sized spheres. Some very large formations are occasionally visible, however most of them are broadly spherical. These approximately 1 μm spheres are generally smoother and easily recognizable. Samples SDA and SDB also contained a portion of smaller spheres, as is evidenced in Fig 3.2a and Fig 3.2c, in the 100 nm range. These samples also appear to contain a greater proportion of concatenated spheres, as compared to the other samples as shown by 3.2h. Nitrogen incorporation could encourage the formation of curved flakes which help form larger spheres. Samples with fewer curved flakes would struggle to form the large curvatures needed for the inner layers of the spheres. This could be contributing to the formation of joined spheres, where many straight flakes force spheres to form oblate centres around which the curved flakes then accreted to form two joined spheres. TEM images may help show the precise mechanism which forms the conjoined spheres. The presence of the smaller spheres could be indicative of sphere centre formation, as proposed by Kroto et al [14], where the sphere centres, unable to find flakes to continue their growth, remain exposed.

SDC presents some of the most pristine carbon spheres of all the samples. The levels of concatenation are lower and no small (<300 nm) carbon spheres were detected. A few very large ($>2\mu m$) spheres are still visible and Fig 3.2d shows the relative uniformity of the spheres. A high magnification scan of the spheres with lower electron beam energy was used to observe the details of the surface structure. The flakes themselves are too small for the SEM to

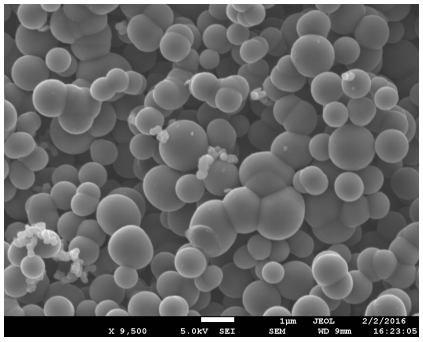

(a) SDA

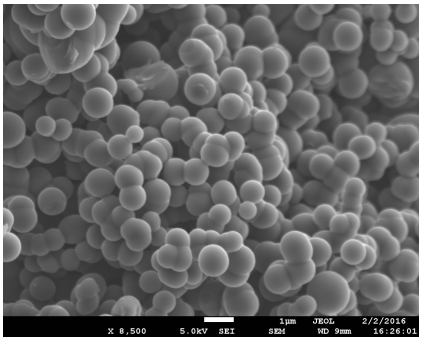

(b) SDA

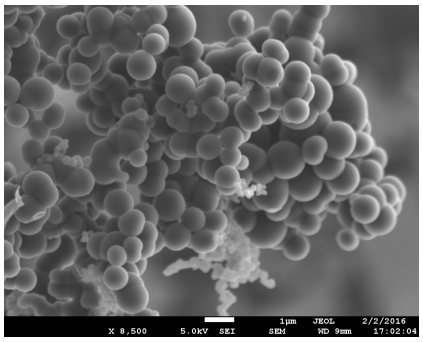

(c) SDB

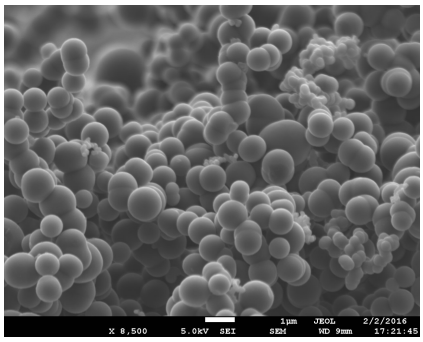

(d) SDB

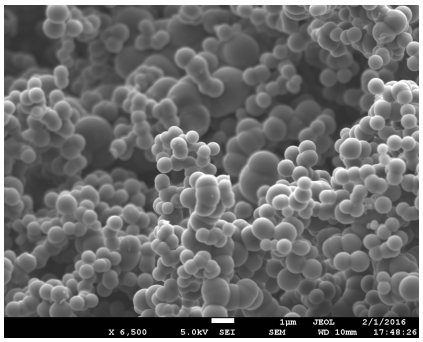

(e) SDC

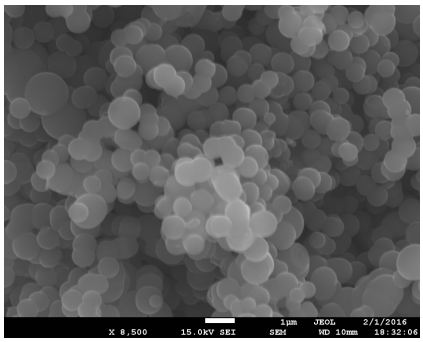

(f) SDC

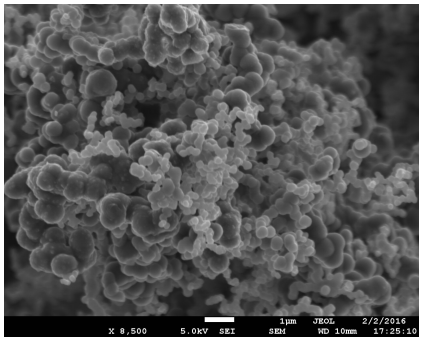

(g) SDD

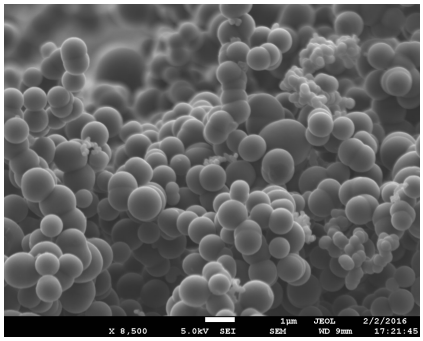

(h) SDD

Figure 3.2: SEM images of the carbon sphere samples.

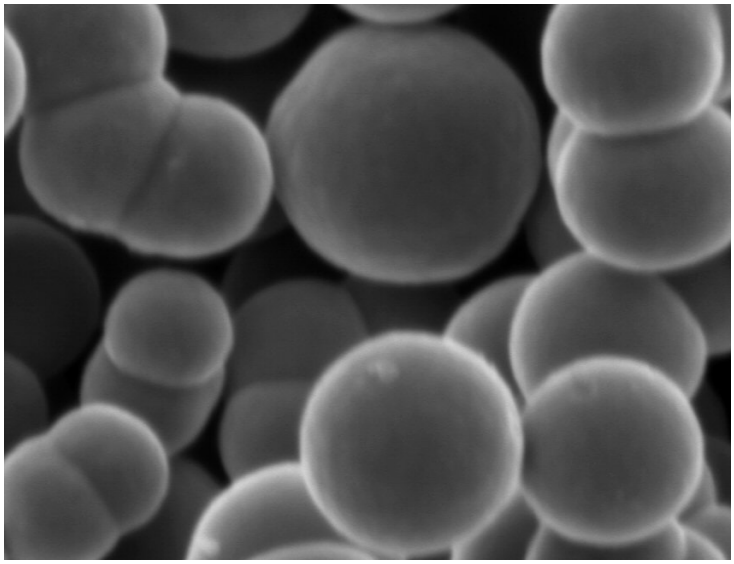

Figure 3.3: A low electron source potential (2 kV) image highlights the surface morphology of the SDC sample showing the uneven surface caused by the flaking on large spheres.The foreground spheres show slight mechanical damage on the surface.

detect directly however Fig 3.3 shows the uneven surface of the spheres, which resemble an orange peel in the SEM, indicative of the coarse morphology of the surface flakes. Finally in Fig 3.4 a damaged sphere found within the sample of SDC being studied demonstrates the structure of the interior. Small concentric delaminations are visible, indicated by arrows, showing how the flakes have arranged themselves concentrically rather than radially. It is likely that the delamination itself occurred during the sphere fracturing event and is not necessarily a standard part of the spheres.

SDD presents a number of peculiarities to be discussed. Firstly the number of smaller spheres is much higher when compared to the other samples. The larger spheres themselves appear heavily deformed and the surfaces contain a number of protuberances. Concatenation is also present which, in conjunction with the oblate deformation, create long worm-like structures. Fig 3.5a highlights these features with a low energy electron beam. The large central spheres are covered in small bright spots which are protruding structures charging and therefore appear bright. A high energy electron beam was used

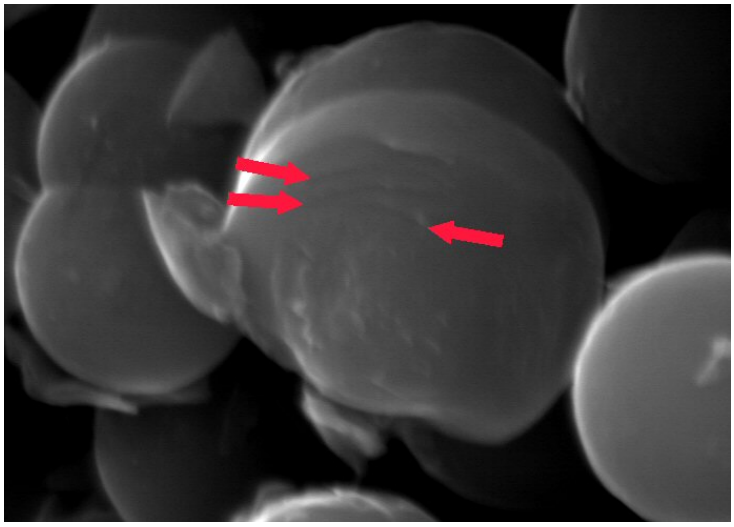

Figure 3.4: The damaged sphere above demonstrates the concentrically layered nature of the samples with the arrows showing areas of separation between layers of graphite likely caused when the sphere was damaged. The core which is now exposed retains its spherical shape demonstrating that the spherical morphology extends below the surface of the spheres.

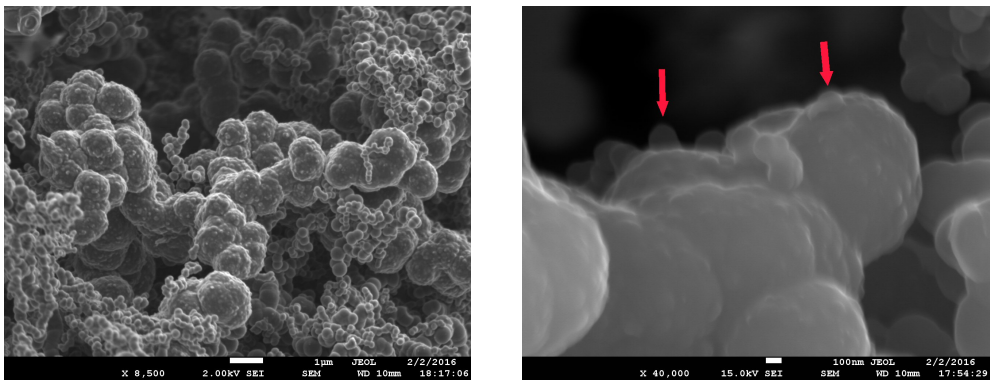

(a) SDD (b) SDD

Figure 3.5: SEM images of the surface of SDD carbon spheres..

to create the highly magnified image in Fig 3.5b. This allows for the electron beam to penetrate the first few layers of the spheres revealing a number of structures protruding from it. Some of the images of the SDB sample also contain a few of these protrusions however they are much rarer in the SDB sample. These images bear some resemblance to SEM images of some nanodiamond samples which contain a relatively high quantity of sp^2 hybridised carbon. These results are particularly interesting when compared with the XPS data discussed below.

3.2.2 X-ray photoelectron spectroscopy

X-ray photoelectron spectroscopy (XPS) is a technique which reveals the elemental composition and chemical shifts of the surface of a material. High energy X-rays are allowed to impact the surface of a material causing its surface electrons to be ejected. The momentum of the ejected electrons is compared to the incident photons and the difference between the two is indicative of the chemical species present and their bonding characteristics. To eliminate collisions between the ejected electrons and atmospheric particles the sample under investigation is placed in a vacuum. The XPS data presented in the first table is compared to traditional elemental analysis by mass spectrometry.

Sample Name	Elemental Analysis %		XPS analysis %		
	C	N	C	N	O
SDB	98.28	0.41	97	1	2
SDC	93.90	2.39	93	3	4
SDD	94.44	3.84	92	5	3
SDA	98.46	ND	-	-	-

Table 3.1: Elemental composition of the carbon microsphere samples. Elemental and XPS data commissioned by the School of Chemistry. Percentages quoted by number. Sample SDA had no detectable nitrogen and consequently no XPS experiment was conducted. No experimental errors were provided.

Samples SDB, SDC and SDD were synthesised with different levels of acetonitrile in the precursor gases. This created samples with varying degrees of nitrogen doping. The elemental analysis shows steadily increasing levels of nitrogen present which is confirmed by the XPS data. The XPS data also shows the presence of oxygen to be significant within the samples. This is evidence of the presence of oxygen containing functional groups which fulfil the valence requirements of the flakes [4]. Some oxygen absorption from the atmosphere is also possible [97] and would be overemphasised, as compared to the bulk, in the XPS data due to the sensitivity of XPS being limited to the surface layers. The limiting penetration depth of the electrons and given that the spheres range from 700 nm to 1 μm the statements regarding the interior of the spheres should not be made using data from this technique. We also note that the presence of oxygen and possibly other chemical impurities is born out by the elemental analysis where the entire mass of the sample is not accounted for by carbon and nitrogen atoms. SDA was created in a pure acetylene environment and so reported no detectable nitrogen within the sample. This sample was not tested with the XPS technique however some oxygen absorption is likely present in this sample as well. The data was provided without experimental errors and therefore should only be used as indicative of relative concentrations. Accurate calculations based on this data were not possible.

Nitrogen doping in a complex carbon structure can occur in a number of configurations [98]. The nitrogen can be incorporated interstitially, essentially creating pockets of nitrogen bound between the layers of the microspheres during synthesis or it can be incorporated in to the graphitic lattice as it forms. Graphitic incorporation itself can produce a number of orientations between nitrogen and carbon atoms [99], as discussed in Chapter 2. XPS can be used to differentiate between these nitrogen species.

The XPS data broadly shows that as nitrogen incorporation occurs the quantity of pyridinic nitrogen increases. Nitrogen doping also drives the formation of nitrogen structures which involve nitrogen double bonds or more than one

Sample	Nitrogen Species %				
	Pyridinic	Pyridinic / Pyrrolic	Pyrrolic	Pyrrolic / Quaternary	Quaternary
SDB		23		77	
SDC	17			83	
SDD	26				74

Table 3.2: Composition of Nitrogen species in synthesised samples. The column titled with two nitrogen species indicate when an XPS peak centre is between two species and the percentage attributable to a particular species can't be discerned

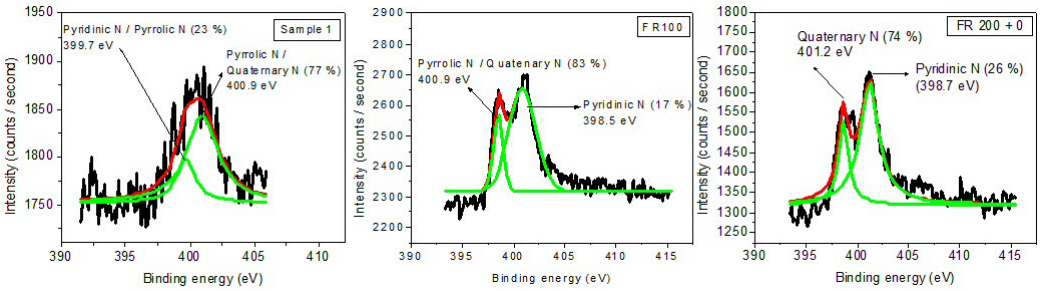

Figure 3.6: Peak fitting applied to sample XPS data. The SDB spectrum is characterised by a very small signal which is close to the background making peak fitting difficult.

nitrogen such as quaternary nitrogen. Li et al [100] also showed how the higher temperatures promote the creation of pyridinic nitrogen from quaternary nitrogen. A similar process may be the cause for the promotion of pyridinic nitrogen in some CMS samples. Further XPS studies conducted by Jian et al [101] showed how the nitrogen containing precursor could influence the nitrogen functional group produced in the carbon heterostructure.

Quaternary nitrogen also has a less disruptive effect on the graphitic lattice, inserting itself smoothly while the pyridinic form tends to create vacancies and edge defects [25]. The Raman data presented in the Results section also confirms the increase in the number of edge defects present. The low quantity of nitrogen in the SDB sample made the peak fitting difficult with the peak itself only barely rising above the noise floor in Fig. 3.6. Confident

statements as to the distribution of nitrogen species based on this data should not be made for SDB.

Comparing the results obtained in XPS and SEM it is possible that the large quantity of pyridinic nitrogen detected in the SDD sample is the source of the deformations and bumps on the sphere surfaces. As discussed previously the vacancies and heptagonal rings could be the source of the large amounts of distortion in the SDD sample as well as the formation of protuberances from the surface. Another possibility is the presence of sp^3 hybridisation creating some bonding which is out-of-plane to the graphitic lattice. Growth around these points might then produce the protrusions seen in the SEM images. SDC, by comparison, contains less pyridinic nitrogen and therefore its structures are exclusively graphitic. Smooth spheres with well defined surfaces are formed because the nitrogen is included smoothly in the graphitic lattice. Finally, even though SDB contains a small quantity of nitrogen and the XPS signal is noisy the presence of a few of these structures similar to SDD points to similarities between the samples. This pattern of data is reproduced in the electrical transport measurements in this thesis and points towards the form of nitrogen incorporated in to the sample as relevant to the overall conductivity. The synthesis parameters that encourage the formation of one type of nitrogen over another are not clear from these samples however it is possible that the presence of excessive quantities of nitrogen or different temperature profiles during synthesis may lead to the preference for quaternary over other nitrogen structures.

Chapter 4

Experimental Apparatus Design

In this chapter the apparatus employed to complete the experiments for this thesis will be discussed. A large portion of the equipment had to be designed and fabricated within the laboratory and some of the design choices will be explained where necessary. The sample chamber design and construction will be discussed in detail. Further details regarding the circuitry and computer software developed specifically for this work will be reported in detail in the appendices. The apparatus description is followed by the experimental procedure for data collection for each technique. The data was processed primarily using Microsoft Excel.

4.1 Electron transport apparatus

In 1958 Leo van der Pauw demonstrated a technique for determining the resistivity and Hall coefficient of a material with an arbitrarily shaped sample [102]. A number of conditions however must be met in order for the van der Pauw equation to describe the resistivity of the system. The sample must be

approximately two dimensional, with its thickness being substantially smaller than its length and width [103]. The sample must be simply connected, without holes or areas of inhomogeneity. High quality contacts must be placed on the periphery of the sample with their contact area made as small as possible. Errors contributed by their non-zero size are dependent on the ratio of their diameter to the distance between contact points. Measurement accuracy can be improved and their repeatability checked by using both reciprocal and reverse polarity measurements. To complete these sets of measurements computer controlled equipment performs all the measurements for a specific temperature. The reciprocal and reverse polarity measurements are completed by using a computer controlled physical relay multiplexer.

The requirements to perform the previously described experiments are as follows. Further details of the assembly of the transport station can be found in Appendix A.

Multimeter with 4-wire measurement capabilities.

Power supply with current meter.

Voltmeter

Cryostat to control the sample temperature during experiments

Variable magnet capable of generating a magnetic field perpendicular to the sample.

Multiplexer to perform reciprocal and reverse polarity measurements

Computer for data collection and equipment control during long experiments.

4.1.1 Cryogenic system

Temperature control system

The cryogenic system employed to control the sample temperature during transport measurements consists of an Oxford Instruments CF1200 continuous flow cryostat coupled to the cryogen dewer with an Oxford GFS650 transfer tube. Cryogen flow is controlled with a Oxford GF3 pump and the temperature is monitored via thermocouple by an Oxford ITC503 Temperature Controller connected to a control heater placed within the cryostat. The sample is delivered in to the cryostat environment using two different cryostat inserts, discussed in the following section, depending on the experimental requirements. A Lakeshore CGR-1-500 carbon glass resistance thermometer is connected to a Lakeshore 234D temperature monitor to permit temperature measurements at the sample site in the cryostat.

The cryogenic system is monitored during the experiment by the computer system using custom built LabView code, described in Appendix B. The temperature is set on the Oxford temperature controller which controls the cryostat heater independently. The computer monitors the reported temperatures at the thromocouple and the Lakeshore carbon glass thermometer to ensure the correct operation of the experiment.

Cryostat inserts

The samples are supported in the vertically mounted cryostat via inserts which also carry the electrical signals to the sample. Two cryostat inserts were used, a non motorised insert developed for previous research [104] and a motorised unit developed during this research.

Non motorised unit The non motorised unit consists of a brass end plug designed to seal around the top ring of the cryostat using an o-ring. Placed

on the top of the brass plug are two Oxford 10-pin connectors, sealed with epoxy to prevent cryogen leak, allowing for up to 20 electrical connections. The wires are composed of 0.19mm solid copper wiring encased plastic and entwined in to twisted pairs to reduce noise pickup. A 6.35 mm stainless steel tube section provides the primary structure to the bottom of the cryostat with spacers placed along its length which also act as radiation baffles. Small holes in the baffles allow for cryogen to flow to the sample.

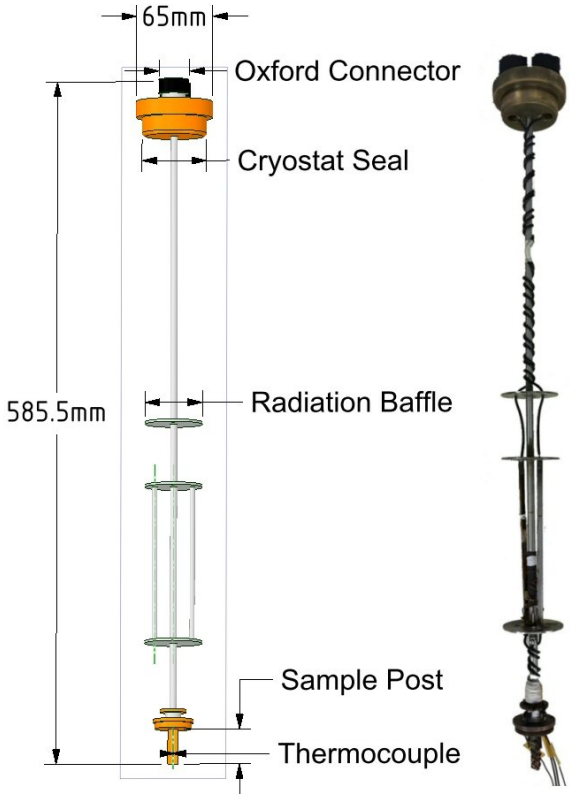

Figure 4.1: The design of the non-motorised probe. 3D model is to scale on the left and the final complete probe on the right.

At the end of the insert the sample was attached to the end post using a small screw through the sample's PLA holder. The carbon glass thermometer was placed within a groove in the copper end post of the insert to reduce any movement of its electrical leads and to provide a large heat sink in contact with the thermometer. All the wires used to connect to the thermometer and the sample were held in place using Oxford epoxy resin.

Motorised unit The motorised insert provided the capability of rotating the sample in the magnetic field during the experiment reversing the applied magnetic field to the sample. At the top of the motorised insert a large brass chamber contains the stepper motor and two Oxford 10 pin connectors on opposing sides. The motor employed is a Fulling Motor Unipolar High Torque stepper motor with a 1.8 degree step size. The brass end chamber is connected to the brass end plug which creates a seal with the cryostat. The main structure of the insert is a 6.35mm stainless steel tube with spacers spaced along its length. These spacers also provide some radiation shielding. A brass rod, which runs within the length of the stainless steel tube, is connected with a brass coupling end to the motor's drive shaft. This permits the motor to rotate the sample chamber at the far end of the insert without rotating the outer tube, the wiring or the spacers.

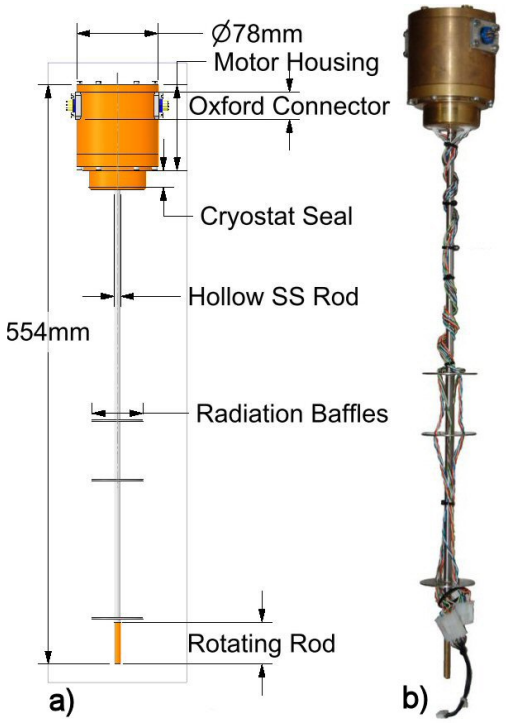

Figure 4.2: Diagram of the motorised cryostat insert. a) To scale, annotated, 3D model of the cryostat insert. b) Photograph of the completed insert with counterwound wiring installed.

At the sample end of the insert a custom connector was designed to hold the sample chambers. Fifteen 22 AWG signal carrying wires run to the bottom of the sample chamber encased in individual plastic sheaths. They are placed in offset twisted pairs to reduce interference and are rated for very low crosstalk by altering the pitch of each cable. The connection functions are marked in the table below. The magnetic field sensors are placed on the sample chamber itself and not on the insert so that they can rotate with the sample. They are discussed in the following sections regarding sample chamber.

Terminal X		Terminal Y	
Oxford Pin	Function	Oxford Pin	Function
A	Hall Sensor Out	A	Motor Supply
B	Hall Voltage +5V	B	Motor Coil 1
C	Hall Sensor Ground	C	Motor Coil 2
D	Sample	D	Motor Coil 3
E	Sample	E	Motor Coil 4
F	Sample	F	Thermocouple I+
H	Sample	H	NC
J	Sample	J	Thermocouple I-
K	Sample	K	Thermocouple V+
L	Sample	L	Thermocouple V-

Table 4.1: Motorised Probe Wiring

4.1.2 Sample chambers

Due to the powder nature of the samples being investigated the packing and contact quality present particular challenges for electrical transport measurements. Inhomogeneity in sample density and large differences in contact quality can cause the measurements to be inaccurate. Furthermore a constant thickness is required to retain the validity of the van der Pauw technique. To this end the samples were placed in a cavity and then a tamper was applied to the sample and bolted in place. Different contact materials were used to determine their impact on measurements. The reciprocal and reverse polarity measurements were monitored to confirm that there was no large scale

inhomogeneity such as voids in the pressed powder. While microscopic inhomogeneity is still present between spheres this would be insignificant at the scales of the sample powder pucks. The sample chambers were manufactured using a RepRap Ormerod 2 3D printer out of Polylactic Acid thermoplastic. The slicing of the 3D models was performed by Cura and Slic3r open-source software and machine control was performed using the built in network interface.

Van der Pauw chambers

Two sample geometries were investigated to determine the resistivity of the samples namely, the Greek cross and the square van der Pauw geometries using two different contact types. The sample thickness was carefully controlled due to its potential impact on the results [103].

Greek cross design The Greek cross sample chamber arm has width of 2 mm [A] and each arm has a length of 12 mm [B]. The sample chamber is 2 mm deep and the tamper area is 1.7 mm tall allowing for 0.3 mm of sample thickness.

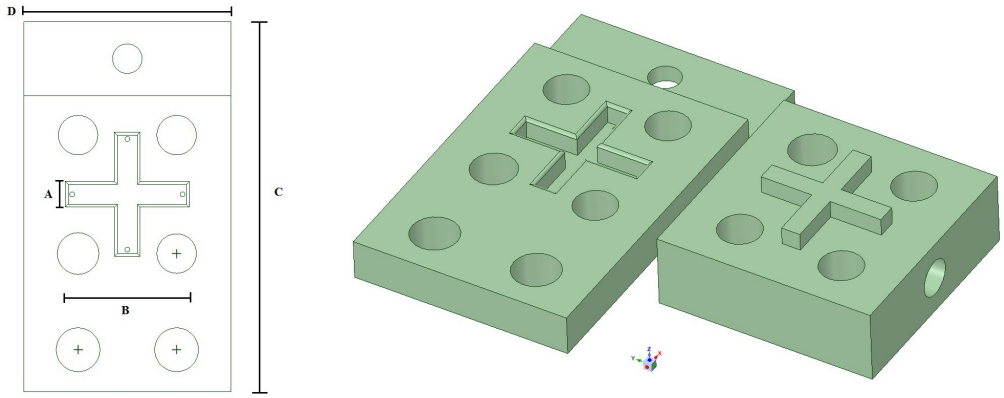

Figure 4.3: Design of the Greek cross Van der Pauw Chamber

The Greek cross samples were equipped with contacts composed of 32AWG copper wires, stripped of their insulation, and placed from the bottom of the cavity to the top along the walls at the ends of the arms of the cross. The contact entry points in to the sample are marked as circles in Figure 4.3 Due to their small diameter they could not be manufactured on the 3D printer directly and were added post production using a needle heated to 400^{o}C. The copper wire was then threaded through these holes and made to loop back to the rear of the cell. They were then directly soldered to the wires on the ends of the cryostat inserts. A small cylinder was designed in to the tamper head behind the tamper to house the carbon glass thermometer. This ensured the thermometer was no more than 3mm from the sample being studied. A new cell was produced for each sample under investigation to remove the possibility of contamination.

Square cell design The Square van der Pauw sample chamber was also produced using the 3D printing technique described above. The sample chamber has a slightly different attachment to the cryostat insert as compared to the Greek cell. The two sides of the cell chamber are 5 mm [A] and the whole cell sides are 21 mm [B]. The cavity is 2 mm deep and the tamper is 1.9 mm high allowing for a sample thickness of 0.1 mm.

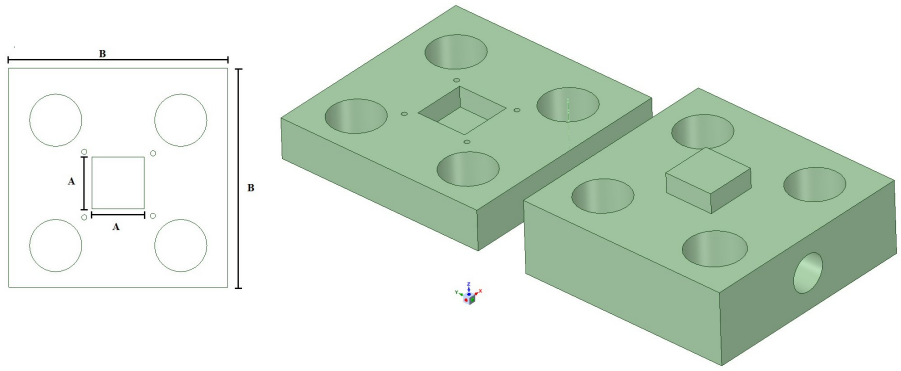

Figure 4.4: Design of the Van der Pauw Square Sample Chamber

The square cell contacts were produced by painting small contact areas on the corner walls of the cell using RS Components Silver Conductive Paint.

Four 32AWG copper wires were allowed to loop on the surface through the holes marked with circles in the design, produced as described above. The wires were then heat set in to the plastic body to prevent any movement. The conductive paste was painted from the inside of the cell to the wires which were set in to the plastic. The conductive paste becomes very rigid upon drying and any movement of the wires breaks the contact. The cavity for the carbon glass thermometer is again present to allow for accurate sample temperature measurements.

The wires that protrude from the base of the sample chamber were then soldered to a printed circuit board. The board facilitated swapping sample chambers by providing large solder pads to connect the sample cryostat insert wires. The circuit boards were also bolted on to the back of the test cell reducing movement in the wires penetrating the central chamber. This was especially important in the motorised sample where any tension in the wires created with a rotation should not be transferred to the wires making contact within the cell. A specific mounting plate with incorporated stand to facilitate sample packing was also designed and manufactured using the 3D printing technique. A new cell was manufactured for each sample test run to remove the possibility of sample contamination.

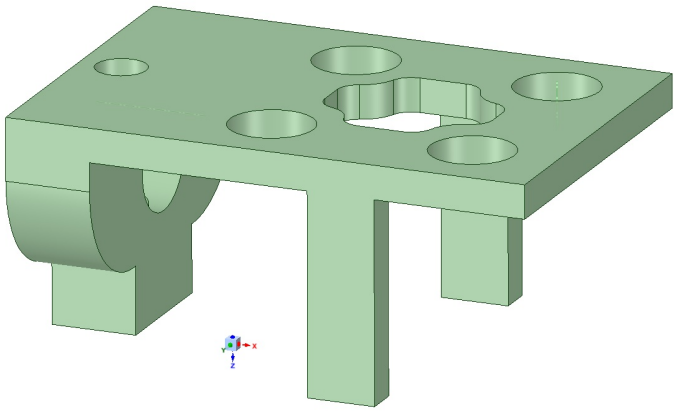

Figure 4.5: Schematic of sample chamber stand designed for packing the samples and mounting the sample chambers on the cryostat inserts.

Hall Effect Chamber

Linear Bar Cell The linear bar cell was produced similarly to the square cell with a slightly altered geometry. It was primarily used to determine the Hall coefficient of the sample using a classic hall arrangement. To allow for balancing of the Hall voltage contact points an extra contact was placed on one side of the sample chamber. A Potentiometer was then used to zero the contact potential prior to measuring the Hall Voltage. The thermal component of the voltage arising from the DC source was removed by inverting the current direction and allowing the system to stabilise thermally using the cryogenic apparatus. The contacts employed in this cell were identical to the contacts used in the Greek cross arrangement, namely copper wires fed through the plastic bed of the sample chamber and running up along the walls of the chamber. The wires were then heat set in to the plastic to reduce movement. The sample chamber is 7 mm [A] long and 2.5 mm [B] wide with a chamber depth of 2 mm. The tamper has a height of 1.9 mm allowing for a sample thickness of 0.1 mm in the chamber. The total size of the sample chamber is 30 mm [C] long and 21 mm [D] wide.

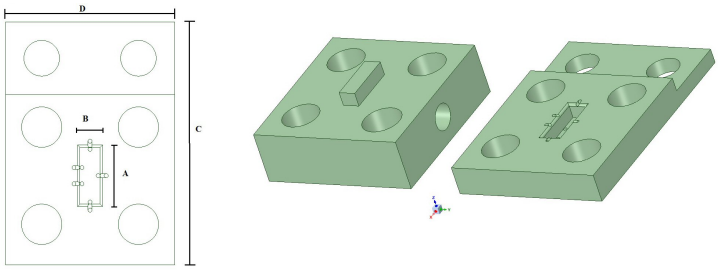

Figure 4.6: Linear Cell employed in Hall Effect measurements.

This cell was also equipped with a printed circuit board to maintain the position of contacts and to provide a support platform for other experimental controls, namely the thermocouple placed within the tamper and a hall effect sensor that was employed to confirm the direction of the magnetic field during hall effect measurements. These were electrically connected to the cryostat insert via a set of PCB connectors. The PCB friction connectors provided an easy way to change sample and provided a measure of fail-safety. Should

the motor over rotate the connector would disconnect before more radical damage was done to the test cell.

4.1.3 Electrical transport station

The electrical transport station is composed of a number of components required to perform the van der Pauw resistivity and Hall Effect measurements. The measurement equipment is composed of a HP3457A multimeter which was used in all Hall effect measurements and a Fluke 8840A multimeter which was used for the resistivity and IV characterisation measurements. A Lakeshore 120 constant current source was used as the current supply. A break out box allowed to interface the 10 pin Oxford connectors used on the top of the cryostat inserts with a computer controlled multiplexer enabling measurement runs to be automated. The multiplexer controlled the connection between the sample cell and the measurement equipment. The reciprocal and reverse polarity measurements require up to eight different orientations of the experiment leads. For each temperature investigated the multiplexer had to cycle between these eight orientations. A brief breakdown of the equipment purpose built for this research follows with greater detail available in the appendix A.

Computer controlled multiplexer

The computer controlled multiplexer provided several functions for the different experiment types that were conducted. It primarily drove a bank of mechanical relays that would change the orientation of the current carrying and voltage sensing leads during a resistivity experiment. It also provided a high accuracy power supply that was employed in IV characterisation experiment. A stepper motor control function was included to drive the motorised cryostat insert during hall effect measurements. Ancillary functions included controlling the cryogen flow pump and relaying experiment status back to

the computer. The multiplexer was constructed and designed as part of this research on veroboard using off the shelf components.

The heart of the multiplexer consists of an ATMEL ATmega328 microprocessor deployed with the standard Arduino open source bootloader. This can be programmed using a C++ language, the code employed in the multiplexer can be found in Appendix B. Due to the limited number of digital outputs native to the microprocessor the outputs were augmented with a pair of 74HC595 shift registers daisy chained to provide a total of over 19 digital output lines controlled via SPI communication protocol.

The relay bank used to switch the orientation of the measurement wiring contained 12 mechanical relays. Each relay would receive one input wire from the measurement equipment and redirect it to 4 possible pins on the multimeter. One additional relay was deployed to switch the voltage supply in to the circuit when required for IV measurements. An additional relay was used to disconnect any signal wires that were not needed for a particular experiment to reduce noise. A ULN2803A Darlington transistor pair array chip was used to drive the relay coils from the shift registers.

The high step accuracy power supply used for IV measurements was interfaced to the microprocessor using the SPI protocol. It consisted of a MCP4921 12 Bit Digital to Analogue Converter (DAC) connected to a LM324N single supply operational amplifier chip in non inverting mode. The Op-Amp circuit was designed for a gain of 6 allowing for steps of 7 mV up to the power supply maximum voltage, in this case 30VDC. The gain setting could be changed for higher accuracy by changing the negative feedback resistor. Voltage steps as low as 2 mV were used in this research.

Stepper motor control was achieved through the prebuilt Arduino stepper code library. Four Field Effect Transistors were used to drive each coil of the unipolar stepper motor in the motorised cryostat insert. An off-board relay controlled the power supply to the cryogen pump effectively allowing

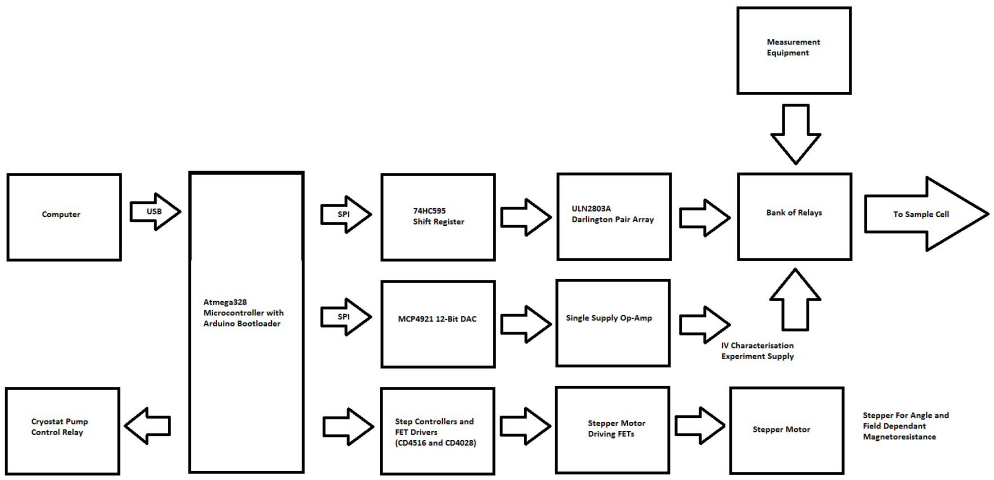

Figure 4.7: Details of the logic layout and functions of the computer controlled multiplexer

the system to automatically shut off the experiment when it concluded. A schematic of the multiplexer system logic is shown below.

Experiment control and data logging computer

The experiment was controlled using an Intel desktop computer running Windows XP. Data processing took place in Microsoft Office Excel. The experiment control and data logging was performed via a LabView program employing standard hardware drivers for the measurement equipment and serial port commands to interface with the multiplexer. Data was collected over GPIB from the measuring equipment and saved to a CSV format data file. Commands to the multiplexer and Oxford temperature controller were issued over Serial connection. The program is capable of initiating the experiment by setting the measurement and control equipment to the correct states. It can actuate the cryogen pump via the multiplexer relay as well as alter the orientations of the wires. The LabView program is also capable of controlling the power supply of the IV characteristics experiment. At the end of the experiment cryogen flow could be shut off, cryostat heaters disabled

and power supplies shut off automatically. This allowed experiments to be conducted overnight without any supervision. The flow controller only has manual controls and could not be operated by the computer system. The system could not monitor the liquid nitrogen used as a thermocouple reference point. Care was taken to ensure enough liquid nitrogen was present to last the duration of the experiment and the flow rate was set to a median level adequate for the experiment.

4.2 Electrical transport experimental procedure

4.2.1 Sample preparation

The samples were prepared in all three transport experiments in a similar manner. The sample cells printed and the contacts added prior to sample packing. The sample chambers were cleaned of any plastic or dust residues. The powder sample was poured in to the cavity and spread equally in to the chamber. The tamper half of the cell was used to press the sample powder and the process was repeated until sufficient powder was pressed in to the chamber. The mass of powder was carefully measured to ensure that the density of the samples would be approximately equal allowing for quantitative analysis of the results to be performed. Equal quantities of powder and identical sample geometry also ensured the packing pressure remained similar for the samples being studied [103] [102]. The contact resistance and sample resistivity are both affected by the packing pressure of the powdered samples. The tamper was then pressed in to the chamber and four brass bolts were used to secure the tamper to the cell chamber through four 4mm holes in the plastic cells. Cells with printed circuit boards would also have the circuit board fastened with the same bolts. Brass bolts were used in order to avoid any magnetisation forming around the sample

during high magnetic field experiments. The samples were then attached to the connection point on the cryostat insert and all the electrical connections were completed. Care was taken when moving any of the samples not to induce any excessive mechanical shock. Previous experiments with older test cells demonstrated that excessive movement could cause powder in the cell to shift, sometimes increasing the contact resistance by up to three orders of magnitude. Samples were then carefully lowered in to the cryostat with the cryostat insert and the electrical contacts were tested for continuity prior to commencement of the experiment. Each sample tested had a pristine cell printed to avoid contamination and the cells were never opened allowing for repeat measurements.

4.2.2 Resistivity measurements

The experimental procedure employed was identical between the square and Greek cross van der Pauw geometries. Once the cryostat insert had been placed within the cryostat and basic electrical connections were tested the LabView program was set up to run the experiment. Measurements were completed on a range of temperatures from 300K to 80K in steps of 20K. An hour and half to two hours was allowed between temperature points to allow the system to come to thermal equilibrium. At each temperature point a set of resistivity readings were taken by passing a current between two adjacent points and measuring the resulting voltage between the next two adjacent points. Ten readings would be taken for each orientation at each data point with five seconds between each reading. Averages and errors could then be calculated. The positions of current input and voltage reading were rotated about the sample in a clockwise direction by the intelligent multiplexer relay assembly and at each new orientation a new set of readings were taken. This provided all the reciprocal measurements required to test van der Pauw validity. During the entire resistivity experiment, in both sample geometries and at all temperatures, the inhomogeneity factor averaged 0.95 and was never lower than 0.89. This indicates that the van der Pauw technique could

be employed on samples prepared using this method. Once a full set of rotation had been completed the current carrying wire contacts were switched in order to take the reverse polarity van der Pauw measurements. The contacts were allowed to rotate about the sample to complete all the reverse polarity measurements for each reciprocal measurement. These measurements would be used to determine and remove the contact resistance. Furthermore all the readings can be used to average out any fluctuations, improving the overall accuracy of the measurements. Upon completion of the experiment the system returned the cryostat to 300K in order to prepare it for a change of sample.

4.2.3 IV characterisation

IV characterisation measurements were performed in a similar manner to the resistivity measurements. All IV characterisation readings were conducted on the square cell design with the current running diagonally across the sample chamber. This was done due to the high quality of the silver paint contacts and the low sample resistance. Readings were taken from 280K to 80K in steps of 20K. Two hours of thermal stabilisation time was allocated to each temperature point. The multiplexer would then switch the relay system to IV mode by connecting the on board power supply to the sample chamber. Readings were taken with various voltage ranges as delivered by the DAC of the computer controlled multiplexer. Voltage measurements were taken on the Fluke 8804A simultaneously to the current reading take from the HP3457A. A small delay of ten seconds was allowed between readings to allow the new current to stabilise in the sample. Once the experiment had reached the maximum voltage the power supply was reset to 0V and the temperature set to a new level. At the conclusion of the experiment the power supply was shut off and the temperature returned to 300K for easy sample change. Once upgrades to the LabView control code were implemented IV and Resistivity measurements could be conducted on the same temperature run, saving cryogen.

4.2.4 Hall Effect measurements

All Hall Effect measurements were conducted using the motorised cryostat insert. The samples were lowered in to the sample chamber with their orientations aligned with the magnetic field coils. The Hall Effect sensor would confirm that the samples were indeed orientated correctly. A number of test movements would be actuated manually to confirm that the movements within the cryostat conformed to expectations. The Hall sensor would confirm the direction of the magnetic field with each movement. Due to the size of the magnetic field the sensor employed, an Allegro Microsystems A1301, would saturate quickly therefore the sensor could only register the 0 field point accurately. It was therefore employed to ensure that any movement of the motor followed by its reverse would return the sensor to the 0 field position. In the 0 field position a current of 10 mA was then allowed to pass through the sample perpendicular to the field direction. The voltage contacts were then balanced with a 100 kΩ potentiometer. The sample was then turned in to the field and a set of 20 measurements 5 seconds apart of the Hall voltage were taken. The sample would then be counter rotated and a set of readings were taken at the zero field point to measure any drift in the zero point voltage. The motor would perform another counter rotation effectively reversing the magnetic field on the sample as compared to the first set of field readings. Another set of readings in this orientation were taken. Finally the probe was rotated back in to the 0 field position to return it to its starting location. This process was repeated 3 times in order to get a good average value of the readings. The current would then be reversed and the entire procedure repeated.

4.3 Electron Paramagnetic Resonance

4.3.1 EPR apparatus

To complete the Electron Paramagnetic Resonance (EPR) experiment a Bruker ESP300E spectrometer was employed. The spectrometer was restricted to continuous wave mode and operated with either a room temperature sample holder or an Oxford continuous flow cryostat for low temperature measurements, described below. Samples were held in the spectrometer within standard Pyrex NMR tubes for all the experiments. Three types of experiments were conducted on the samples described in the experimental methods section.

4.3.2 EPR experimental procedure

Power saturation

In order to determine relaxation time af the paramagnetic defects the power saturation point of the sample may be employed. Samples were placed within the spectrometer and the spectrometer was tuned and calibrated. Microwave power attenuation was adjusted to -30 dB and a signal was acquired. The power was increased to 0 dB in steps of 3 dB with all the spectrometer values maintained between readings. This corresponded to microwave powers of 7.47 μW to 7.47 mW. The sample amplitude was then determined by taking the value of the double integral over the magnetic field sweep for each power value. A plot of the signal amplitude against power level would determine the power level of saturation. The sample's saturation powers could then be compared giving a rough estimate of relaxation times.

Resonance condition

In order to accurately determine the g-values of the samples a well known reference marker was placed within the spectrometer. DPPH (2,2-diphenyl-1-dicrylhydrazyl) was used as a reference g-value marker as it is a well known EPR reference material. The spectrometer would produce a combined signal and the two signals would have to be deconvoluted using using a custom built Matlab code and a curve fitting routine. The magnetic field difference was measured between the sample's and DPPH's signal centres. The large errors in the spectrometer's incident microwave frequency reading prevented direct calculation of the g-value. By comparing the peaks of two samples the frequency could be removed and only the, much more accurate, resonance magnetic field strength used in the calculation. With each sample change the spectrometer would require retuning. Experiments were conducted at room temperature and power levels kept well below saturation.

Low temperature EPR

The low temperature cryostat was mounted in the between the magnetic coils of the spectrometer. A sample was placed within the cryostat and the spectrometer was tuned to the cavity. The cryogen pump was activated and a temperature was set on the Oxford ITC503A and a thermal stabilization time of an hour was allocated between readings. A spectrum was acquired sweeping from 3420 G to 3520 G. Once completed a new temperature point would be entered in to the Oxford temperature controller and the experiment would be repeated. An automated Matlab script was used to extract the parameters to determine the linewidth, signal amplitude and asymmetry ratio. The Matlab code is available in the Appendix B. These were then used to determine some of the properties of the spheres with changing temperature. Measurements were made ranging in temperature from 310 K to 80 K in steps of 10 K with half the readings taken on the lowering the temperature and the other half while rising in order to allow for any hysteresis. Tuning

was required at each temperature level due to the changes in the cavity with changing temperature.

4.4 Raman Spectroscopy

Raman Spectroscopy has been used extensively to study the structure of carbon nanomaterials [105] [106] [107]. The Raman spectra gathered for this research shed light on the structural changes caused by Nitrogen incorporation. Two Raman spectroscopy units were used for different laser frequencies. A brief description of each of them follows.

Jobin-Yvon LabRAM Raman spectra were acquired using the micro-Raman attachment of a Horiba Jobin-Yvon LabRAM HR Raman spectrometer using the 514.5 nm laser line of a Lexel Model 95 argon ion laser. The incident laser beam was focused onto the sample with a 100x objective and the backscattered light dispersed via a 600 lines/mm grating onto a liquid nitrogen cooled CCD detector. LabSpec v5 software was used to capture and store the data. The laser power at the sample was approximately 0.5 mW.

Jobin-Yvon T64000 Raman spectra were acquired using the micro-Raman attachment of a Jobin-Yvon T64000 triple Raman spectrometer operated in single spectrograph mode. The excitation source was the 647.1 nm line of a Spectra-Physics 165 krypton ion laser. The incident beam was focused onto the sample with a 50x LWD objective and the backscattered light was dispersed via a 600 lines/mm grating onto a liquid nitrogen cooled detector. LabSpec v4 software was used to capture and store the data. The power of the laser was within 1 to 2 mW at the sample surface.

Chapter 5

Experimental Results

In this section the results of the various experimental techniques will be presented and discussed. Each technique will be discussed separately and conclusions will be addressed in the final chapter. The dominant conduction phenomena, majority carrier and carrier density are presented in the first section. The structural characteristics of the spheres and their changes with nitrogen incorporation are discussed in the following section. Finally the spin resonance results are discussed in the final section.

5.1 Electrical transport

The electrical transport of the spheres was investigated using a number of techniques. The Van der Pauw [102] method was employed to determine the changes in resistivity with temperature. This allows model fitting to determine which conduction paradigm was applicable to the spheres. IV characterisation at each temperature revealed the conductance of the spheres and their response to increasing bias voltage. Finally Hall effect measurements were used to determine the majority carrier as well the impact of nitrogen doping.

5.1.1 Resistivity experiment

Resistivity data

The resistivity of all four samples was tested using the Van der Pauw method as discussed in the preceding chapter. The results showing the resistivity of the Greek cross and square cell geometries can be found in Fig 5.1 and Fig 5.2 respectively.

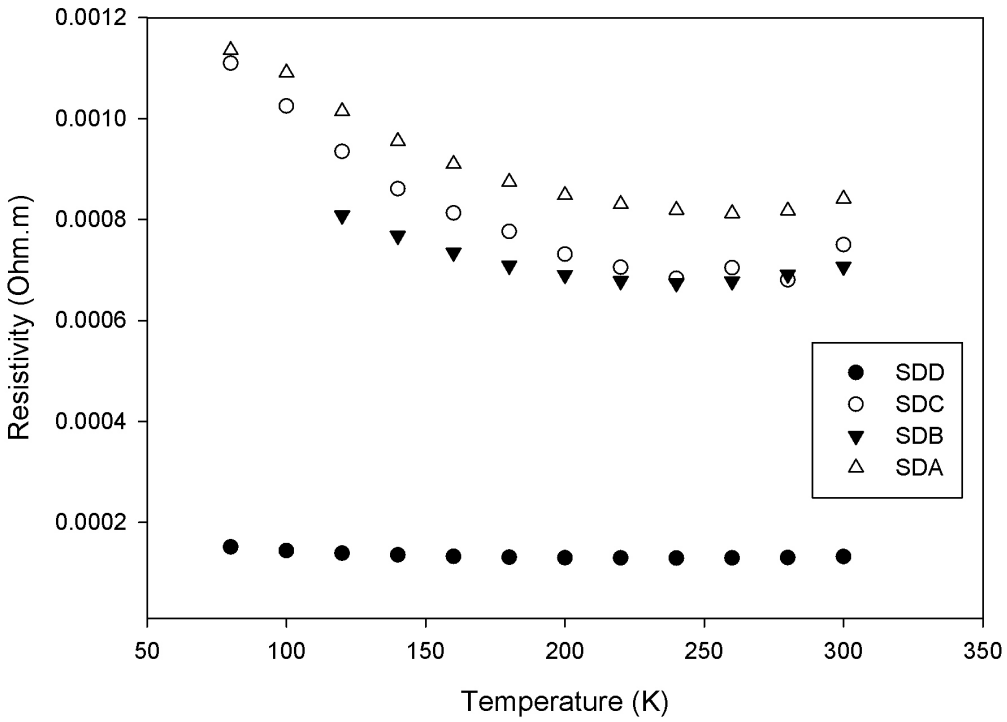

Figure 5.1: The resistivity of each of the samples as determined using the Greek cross VDP geometry.

Firstly, the resistivity is directly proportional to the amount of nitrogen doping in the samples. This is likely due to the extra electron contributed by the nitrogen to the carbon lattice, increasing the number of charge carriers. This was confirmed in the Hall effect measurements. However, this straightforward relationship breaks down as SDB presents a lower resistivity compared

to SDC despite the latter's greater nitrogen content. Clearly, structural elements such as the type of nitrogen functional, their density and the overall carbon sphere order are also contributing to the conduction. Both sample geometries present this pattern.

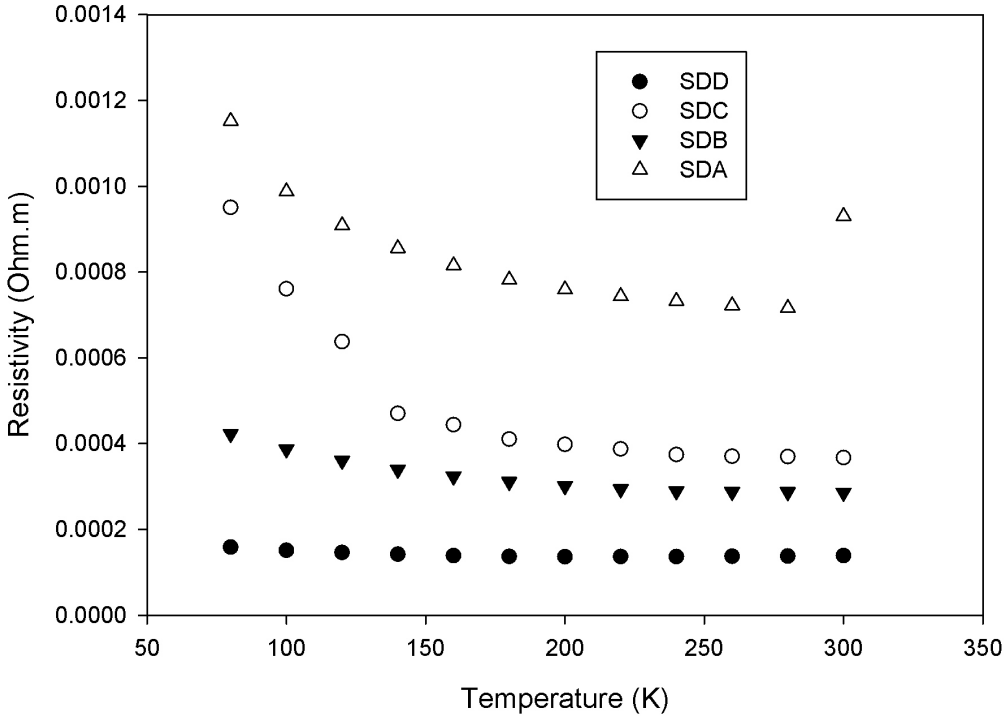

Figure 5.2: The resistivity of each of the samples as determined using the square VDP geometry.

Secondly, the resistivity is inversely proportional to temperature which is characteristic of thermally activated transport such as is described in the models developed earlier. Some of the samples however demonstrate an appreciable upturn at high temperatures. This was previously detected in other CMS samples [60] [108] and carbon mats [51] [49] and represents a metallic transition. Samples with lower nitrogen content have a slightly stronger upturn with temperature. While this may be an intrinsic property of the material, direct conduction measurements on powder samples are affected by the packing quality and the pressure on the sample. In the literature

light compression improved the conduction properties of powder samples as well as moving the characteristic upturn temperatures to a higher range [52]. The presence of stronger upturn in the Greek cross geometry compared to the square is an indication of this phenomenon as the packing quality in the Greek cross cell is more difficult to ensure. Earlier prototype cells with poor packing quality also reproduced this trend.

The results from the two test cell geometries have similar features. The absolute values of the resistivity for SDD agree, however the other samples report a slightly higher resistivity in the Greek cross chamber. This is likely also caused by uneven packing of the cross. One arm of the cross may collect slightly more powder than another causing areas of higher and lower sample density despite controlling the total mass of packed sample. The Greek cross geometry also required more sample and the tamper and cavity are more complicated to match than the simple square. Despite these issues, the disagreement between the geometries is confined to the high temperature results with the low temperatures matching for all the samples. These values therefore represent likely absolute resistivities for bulk nitrogen doped CMS to within one order of magnitude.

Model fitting

The models for conduction discussed in Chapter 2 were all applied to the data collected. An example of some of the fits produced is shown in Fig.5.3 for the square cell geometry packed with SDB sample. The high quality of the fitting is shown by the R^2 values and it is clear that no model can be definitively excluded based on the quality of this fit alone, especially in carbon based compounds [109]. This is a common issue that occurs in the literature as the temperature dependence of the samples is relatively low [110]. In addition, carbon heat treated at varying temperatures possessed ever decreasing temperature dependence.

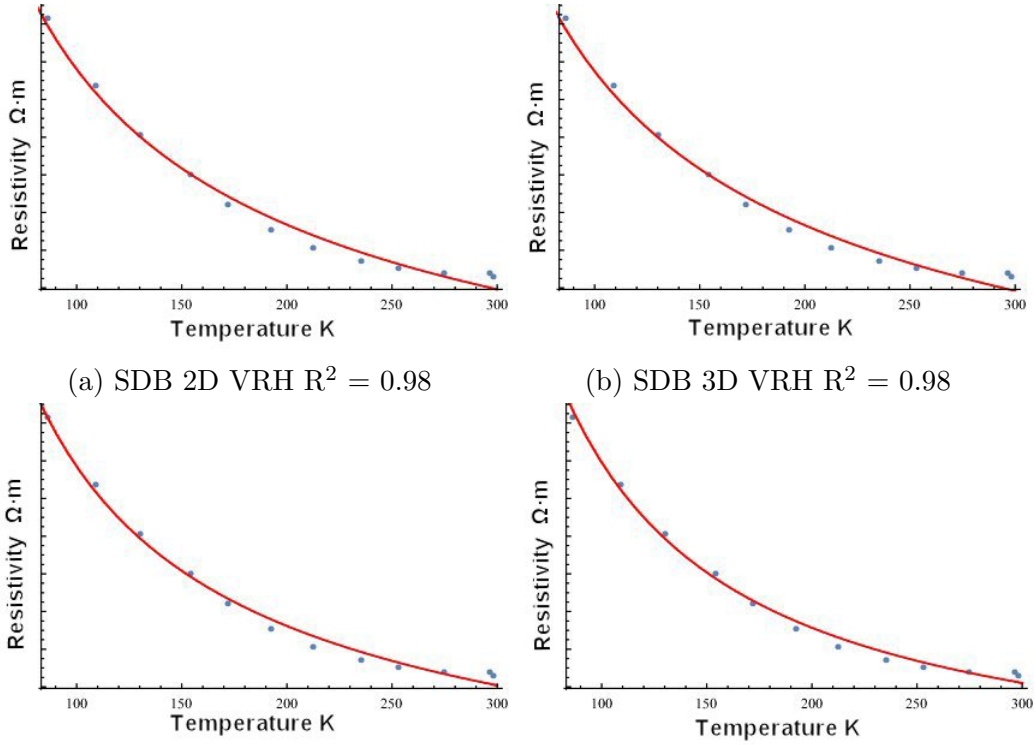

(a) SDB 2D VRH $R^2 = 0.98$

(b) SDB 3D VRH $R^2 = 0.98$

(c) SDB ES VRH $R^2 = 0.99$

(d) SDB FAT $R^2 = 0.97$

Figure 5.3: Examples of some curve fitting to resistivity vs. temperature data and resulting R^2 values applied to SDB.

Of particular interest in the paper by Raj et al [110] is that the onset of deviation from the VRH model occurs at approximately the same temperature for those samples of disordered carbon as the spheres studied here. The heat treatment of the disordered carbons that produced the deviation from VRH in their research matches the synthesis temperature of the carbon spheres, namely approximately 1200K. This indicates that the spheres behave like highly graphitised disordered carbon, which in turn implies the hap-hazard arrangement of the graphitic flakes plays an important part in the conduction mechanism of the spheres. The upturn was modelled by a high temperature quasi-metallic term of the form:

$$\rho_{metal} = Qe^{\left(\frac{-T_m}{T}\right)} \tag{5.1}$$

This term has been used in other electron transport investigations of carbon structures such as CNT macrostructures and in preceding work on carbon spheres [60]. Pietronero first used this term to describe the conduction caused by the phonons present in graphite layers [111]. It is usually associated with 1D conduction and it likely finds applicability here due to the large graphitic nature of the spheres. It dies out at low temperatures as the contribution of phonons dissipates. FAT also makes provision for the presence of a metallic component to the resistivity which becomes more significant at higher temperatures as electrons no longer need to tunnel through the barriers and have sufficient energy to surmount them. This is also an explanation for the observed relationship between packing quality and the resistivity upturn temperature. Improved packing is likely encouraging the creation of differing inter-sphere contacts which either can promote or suppress this metallic conduction mechanism. Further research at higher temperatures is needed to investigate the metallic term, something that is not possible with the PLA test cells due to their low melting point. An example of a Variable Range Hopping fit with the metallic term is shown in Fig.5.4.

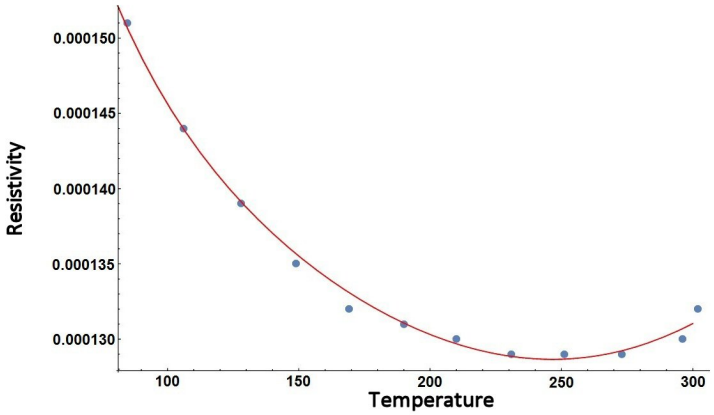

Figure 5.4: An example of a fit of ESVRH and the 1D quasi-metallic conduction term to resistivity data of SDD sample in the Greek cross chamber.

All the semiconducting models modified with the metallic term fit the data well with R^2 values greater than 0.98. Selecting the most likely model for the low temperature conductivity requires an additional test. As discussed in the literature [109] even fitting a straight line to a given VRH model by plotting the resistivity against a $T^{-1/4}$ scale is insufficient to guarantee that a given model is responsible for the conductivity. This can be seen in Fig. 5.3 where all three VRH dimensionality parameter choices produce excellent fits at low temperatures. The dimensionality exponent must be determined empirically in order to ascertain which, if any, of the VRH paradigms are responsible for the charge transport. A logarithmic derivative can be determined from Eqn. 2.10 as follows:

$$W = -\frac{\partial \ln(\rho(T))}{\partial \ln(T)} = p \times \left(\frac{T_0}{T}\right)^p \tag{5.2}$$

This derivative can then determine empirically the exponential term in the general VRH equation by finding the gradient of a $\ln(W)$ vs $\ln(T)$ plot. This was completed numerically and the plots are shown for the samples shown in Fig.5.5.

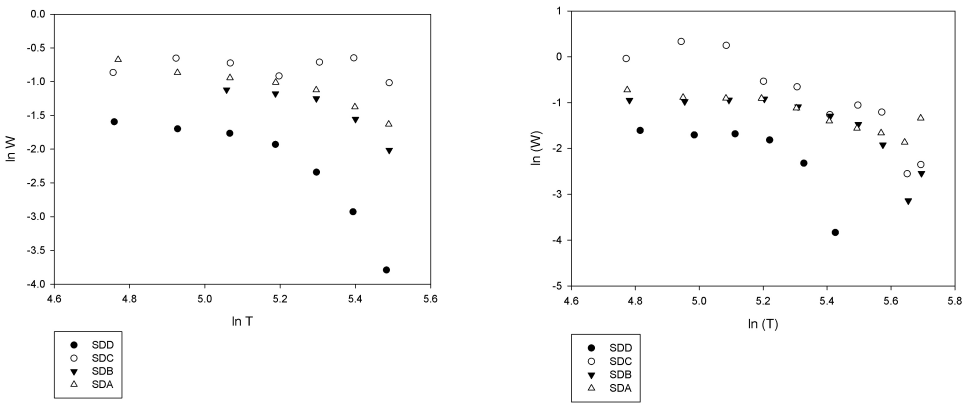

(a) Greek cross cell

(b) Square cell

Figure 5.5: Plots of $\ln(W)$ vs $\ln(T)$ for all the samples in a) the Greek cross and b) Square sample chambers. Non-linear dependence is evident in all the samples studied.

From the Fig 5.5 it is clear that the non linear behaviour is a feature added to the graphs by the metallic term at higher temperatures. The metallic term appears to have a stronger effect on the high conductivity samples while its onset appears to become significant at around 120K. SDA displays some anomalous fits in both sample geometries. At low temperatures the gradient appears linear however more data points are required to truly confirm the gradient and therefore the dominant conduction mechanism. Consequently, two samples were selected for low temperature resistivity measurements using liquid Helium as a refrigerant.

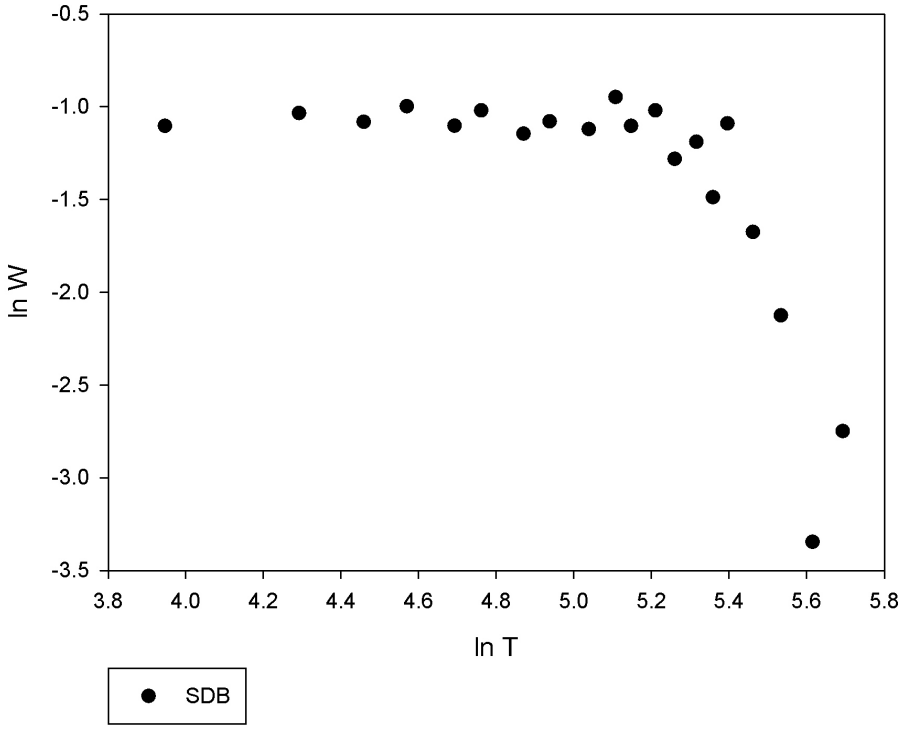

Figure 5.6: Plot showing an example lnW vs lnT plot using liquid helium as a cryogen for SDB in the square cell sample chamber. A very steep gradient change shown is indicative of diverse conduction mechanisms becoming dominant in different temperature regimes.

Fig.5.6 confirms the continuation of the linear component down to 30K. The derivative of this line does not correspond to any of the VRH mechanisms discussed previously, likely ruling out VRH as the dominant conduction mechanism between 120K and 30K. This is further illustrated in Fig.5.7 where the gradient of the VRH models does not match the gradient of the sample in question. Alternative VRH models produce steeper gradients and therefore can also be excluded at these temperature ranges. FAT appears to dominate due to conduction electrons moving easily on some graphitic flakes but encountering barriers such as gaps between flakes, specific flakes of low conductivity or gaps between spheres. Each barrier type may contribute differently to the overall FAT model as the final results are formed by the collection of all the junctions between metallic and insulating regions.

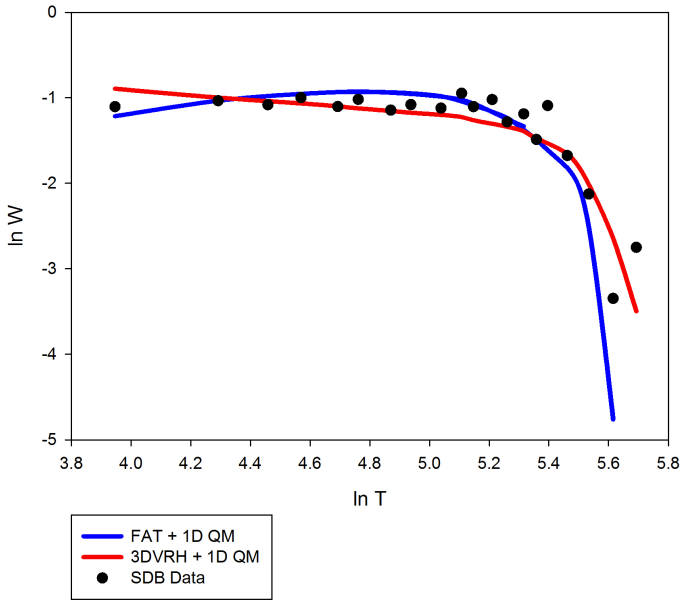

Figure 5.7: The best fits of the models discussed to the data are shown with the data points themselves. Note how the VRH model has a fixed gradient at low temperatures which does not match the gradient of the data points. This reduced the likelyhood that any of the VRH models are exclusively responsible for the conductivity of the samples.

As an alternative option a weak localisation correction to the VRH hopping conduction was attempted. This has been reported in the literature, albeit at lower temperatures than those investigated here [112] [113]. Weak localisation is identified by a logarithmic temperature dependant term correction to other conduction phenomena at low temperatures. It is caused by the reflection of the electron wavefunction in the forward and reverse directions, around a looped random walk which interferes with itself at the point of departure [114]. This is a quantum effect and requires well ordered samples. It did not successfully describe the conduction in these samples, likely due to the disorder in the CMS and relatively high temperature range in this study.

The results of fitting the FAT model to the data are shown in Tbl 5.1 and Tbl 5.2 for the square and Greek cross sample chambers respectively. The two data samples both point to a number of interesting conclusions. The β value in both cases decreases gradually with increasing nitrogen content. Given that the geometries were kept constant for each of the different cells it is expected that this quantity will change primarily due to a lowering of the barrier height. This could be driven by the nitrogen incorporation reducing the effective band gap in the nanographitic flakes, creating more areas of metallic conduction for a given temperature.

	T_s (K)	T_b (K)	β
SDA	22.30 ± 3.53	76 ± 12.8	0.000549
SDB	30.50 ± 4.10	79 ± 13.2	0.000219
SDC	21.05 ± 3.39	183 ± 19.2	0.000171
SDD	17.53 ± 2.22	33 ± 2.3	0.000117

Table 5.1: Results of model fitting on square sample cell data.

The T_b quantity is indicative of the shape and height of the potential barriers. In this case, the low nitrogen samples present values around 70K however SDC and SDD have double and half the baseline value respectively. This is interesting when compared to the SEM data with SDC presenting the a well ordered structure and SDD showing signs of disorder and many smaller spheres. This may indicate that either the sphere morphology or their pack-

ing factor primarily determine the barrier shape. The presence of smaller spheres could also be contributing to the shape of the barrier, improving the packing factor and increasing the coupling between larger spheres. SDD presented the greatest proportion of smaller spheres while SDC presented very few small spheres. SDD and SDB also present protuberances on the surfaces of the larger spheres which might be improving the electrical coupling between spheres. The fact that this does not follow the same pattern as the β value is indicative of the competing factors determining conduction. It is possible that the decreasing β value suggests a decrease in the number of junctions within the spheres, making the intersphere junctions more significant to the shape of the FAT curve as nitrogen makes the spheres ever more conductive. Conduction experiments on single spheres would confirm which junctions are the most pertinent to the overall conduction.

	T_s (K)	T_b (K)	β
SDA	6.58 ± 1.59	60.28 ± 5.94	0.000644
SDB	14.43 ± 3.58	64.76 ± 6.03	0.000514
SDC	55.32 ± 7.85	148.3 ± 15.33	0.000414
SDD	27.66 ± 4.44	34.22 ± 3.55	0.000111

Table 5.2: Results of model fitting on Greek cross sample cell data.

T_s values are indicative of the temperature at which thermal fluctuations become significant to the tunnelling probabilities. It remains below the range of the fits for all the samples and therefore is not directly detectable. It follows a similar pattern to the T_b conduction in most cases as the barrier height and shape will also determine the level of thermal excitation needed to activate the fluctuation assisted tunnelling.

Given the large number of variables, a self-consistent way was needed to determine the initial values for the fits. To do this the numerical derivative of the natural logarithm was used. This eliminated the β value, a scaling factor, as follows:

$$\ln \rho = \ln \beta + \frac{T_b}{T_s + T} \tag{5.3}$$

$$\frac{d\ln\rho}{dT} = -\frac{T_b}{(T_s+T)^2} \tag{5.4}$$

An initial fit of equation 5.4 to the data provided the initial estimates to the variables used in the fits of the full equation and the metallic term. An example is shown in Fig 5.8.

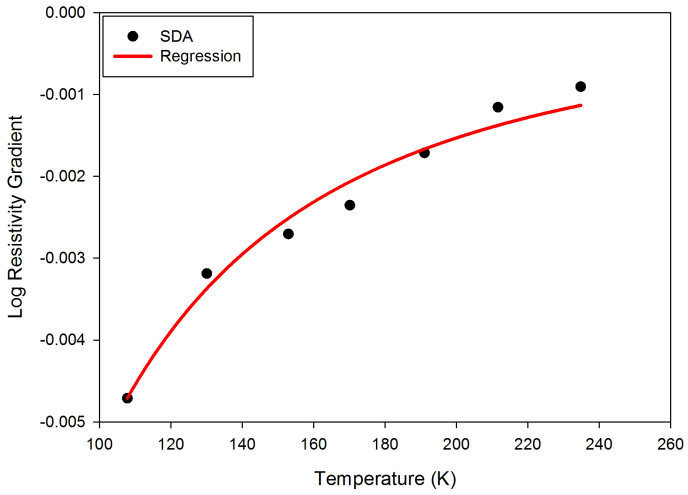

Figure 5.8: A method for providing the initial guess values for the full fitting function in a self consistent manner across all the samples.

5.1.2 IV Characterisation

In order to confirm the presence of fluctuation assisted tunnelling, IV characterisation curves were captured for samples SDB and SDC. A number of difficulties were encountered during the experiment. These samples presented very low resistances compared to previous attempts due to the improvements to the sample chambers. As a result, some samples were damaged due to excessive heating, likely centred around the point of contact with the powder. This invalidated the data and required the sample to be replaced. In response to this the IV curves remain limited in the potential which could

be applied to the sample. Phenomena which might occur at higher applied voltages are therefore not considered here.

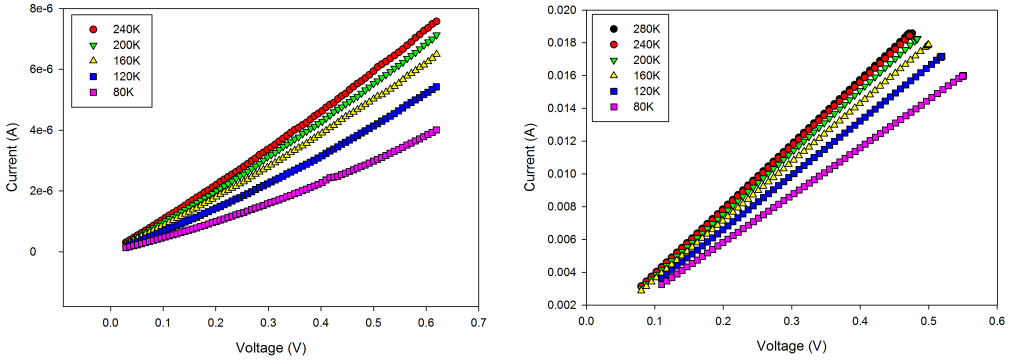

(a) SDC (b) SDB

Figure 5.9: IV Characterisation curves for a)SDC and b)SDB samples using the square sample chamber. As temperature decreases the IV curves become more non-linear in some samples.

Kaiser and Roth [46] [52] showed that the dependence of current on the applied voltage followed the following expression:

$$G = \frac{I}{V} = G_0 \frac{e^{V/V_0}}{1 + h(e^{V/V_0} - 1)} \tag{5.5}$$

Equation 5.5 provides insight into the conduction of the electron in fluctuation assisted tunnelling. G_0 is the low field conductance. The scaling factor V_0 is strongly correlated to the barrier height and is determinant of the saturation of the current at very high fields. Data for the SDC and SDB nitrogen samples were taken as shown in Fig 5.9. This confirmed qualitatively the presence of FAT as the non-linearity of the sample increases with decreasing temperature. Subsequent experiments with a liquid helium cryogen produced the data shown in Fig 5.10. The metallic upturn is highlighted by the inset of Fig 5.10 as the gradient of the high temperature IV curves increases with decreasing temperature.

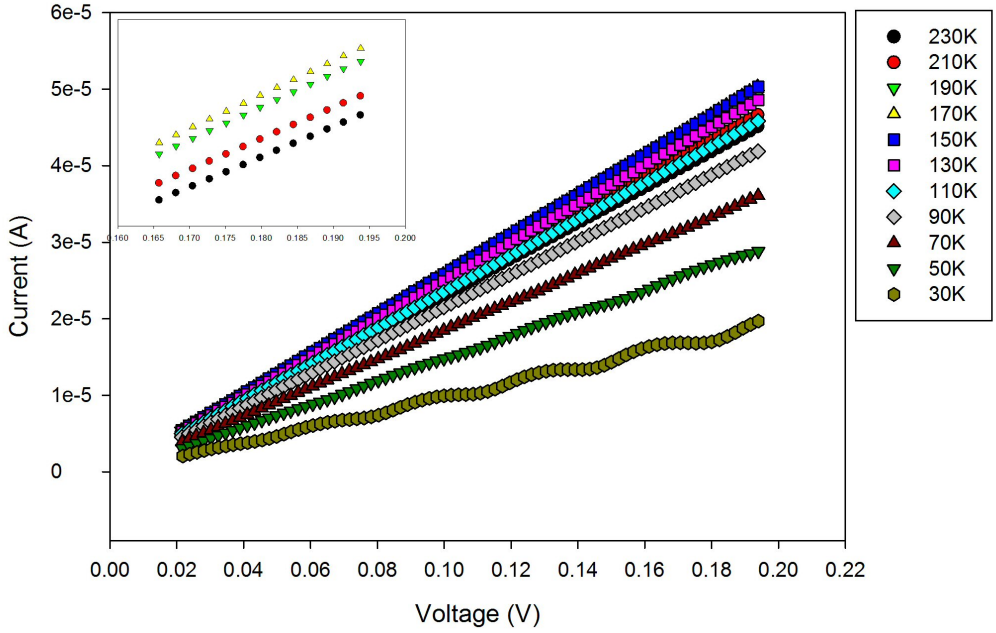

Figure 5.10: IV Characterisation of SDC at low temperatures. The inset shows the high field voltage part of the high temperatures confirming the upturn detected in the resistivity experiments. The 30K data oscillates due to the instability in temperature.

5.1.3 Hall Effect

A basic investigation of the number of charge carriers was conducted using the Hall effect apparatus described in Chapter 4. Given the limitations of the voltmeter and magnetic field, the Hall voltage was detected at the limit of the voltmeter's resolution. Larger magnetic fields would help create a stronger hall voltage and reduce the error. Despite measures to control the thermal voltage, during the experiment the signal would drift continuously even in positions of 0 magnetic field. To eliminate this baseline drift, a 0 field reading was taken between each rotation of the stepper motor creating a linear baseline which could be removed during data processing. Two examples of this process are shown in Fig 5.11. The same procedure was applied with the current reversed and the results were averaged out to improve the

errors. The non-zero voltage readings with 0 applied field are evidence of the thermal hall voltage. Given the limitations of the equipment and the numerical method required to remove the thermally induced voltage the errors in the readings were quite large. Consequently the data is only used to indicate general trends between samples.

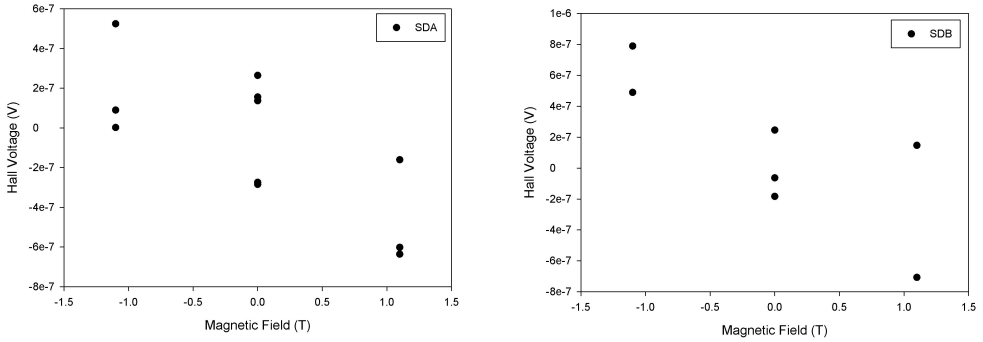

(a) SDA (b) SDB

Figure 5.11: Example plots of Hall effect data collected for samples SDA and SDB. Each point represents a collection of points averaged out for clarity. The constant drift causes the points to shift to lower voltages with each iteration.

The results for the Hall effect experiment are shown in Tbl 5.3. Electrons are the majority carrier in these CMS samples. As one might expect, the sample with the highest nitrogen concentration reported the highest charge carrier concentration. Each incorporated nitrogen is likely to contribute an electron to the carbon lattice which will participate in conduction when bound graphitically. Pyridinic nitrogen would not contribute an electron as its electron pair is not hybridised and would likely impede conduction by creating vacancies and areas of localisation. It is interesting to note that SDC has a lower charge carrier concentration than SDB. This follows the pattern reported in the resistivity, where SDC had slightly poorer conductivity than SDB. Sample SDC reports a more regular distribution of spheres via the SEM images and one of the smallest lattice sizes detected via Raman spectroscopy. Clearly, the nano-structure of the sphere has a greater impact on the number of charge carriers than the total number of nitrogen atoms introduced into the lattice. The XPS data shows that SDC contains the highest percent-

age of pyridinic nitrogen, a non-doping nitrogen functional, as opposed to quaternary nitrogen which contributes directly to the electrons at the Fermi level [115].

	SDA	SDB	SDC	SDD
R_h (m^3/C)	-6.4*10^{-8}	-5.39*10^{-8}	-9.05*10^{-8}	-4.34*10^{-8}
n (m^{-3})	9.77*10^{25}	1.16*10^{26}	6.90*10^{25}	1.44*10^{26}
ΔR_h (m^3/C)	3.22*10^{-8}	2.71*10^{-8}	4.56*10^{-8}	2.18*10^{-8}
Δn (m^{-3})	4.91*10^{25}	5.83*10^{25}	3.47*10^{25}	7.23*10^{25}

Table 5.3: Results from Hall effect experiment showing the relatively large errors present which render the information indicative only and not a definitive description of these samples.

Sample SDA reports a higher charge carrier concentration than SDC despite reporting the lowest conductivity of all the samples. One potential explanation is that the other impurities in SDA, also detected during the ESR and XPS experiments, are contributing a significant number of charge carriers. The resistivity is also a function of charge carrier mobility which may be more closely connected to the β value discussed earlier.

5.2 Raman Spectroscopy

5.2.1 Raman data

The Raman spectra were collected using a red laser at 647 nm and a green laser operating at 514.5 nm wavelengths. Each sample had multiple Raman spectra collected and the least noisy of these was selected for analysis. The background baseline was removed in post-processing. At all wavelengths the samples present two major peaks, namely the D and the G peaks. Some of the samples irradiated with the green laser also show the two smaller peaks around $\approx$1100 cm^{-1} and $\approx$2000 cm^{-1}. In order to extract the structural information from the data, multiple peaks were fitted with various combinations of Gaussian, Lorentzian and Breit-Wigner-Faro (BWF). The preference for

Gaussian peaks in these samples is indicative of a disordered material where there is a random distribution of phonon lifetimes [79]. The BWF peak is a common choice for the G peak [116] [117] [118] [119] due to its asymmetry accounting for more of the spectrum. A BWF fitted G peak can impact extensively on the interpretation of the Raman information due to its long asymmetric tail reducing the intensity of the D peak. For example, in a BWF fit the D peak position is inversely rather than directly proportional to the disorder of the system [120]. In the case of these samples the BWF peak provided the best fit to the available data with the highest R^2 values. Using alternative peaks produce broadly the same trends with slightly worse peak fitting parameters.

When comparing G peak position using a BWF fit, a small modification to the position must be implemented in order to correct for the BWF asymmetry. The following expression has been used by Ferrari et al [79] in their discussion of G peak position and will be used here in order to maintain consistency between this work and the amorphitization trajectory discussed in the Chapter 2.

$$\omega_{max} = \omega_0 + \frac{\Gamma}{2Q} \tag{5.6}$$

Where ω_0 is the fitted peak centre, Γ is a factor of the width of the peak and Q is the coupling coefficient. All the G peak positions fitted with a BWF function reported further have been corrected in this way.

The Raman spectra recorded with 647 nm laser source are shown in Fig 5.12 along with their fits. The properties of the best fits are recorded in Tbl. 5.4. The best fits are those where a Gaussian is fitted for the D peak and a BWF is fitted for the G peak with R^2 values greater than 0.98. The spectra and their respective data tables are shown in Fig 5.12 and Tbl 5.4.

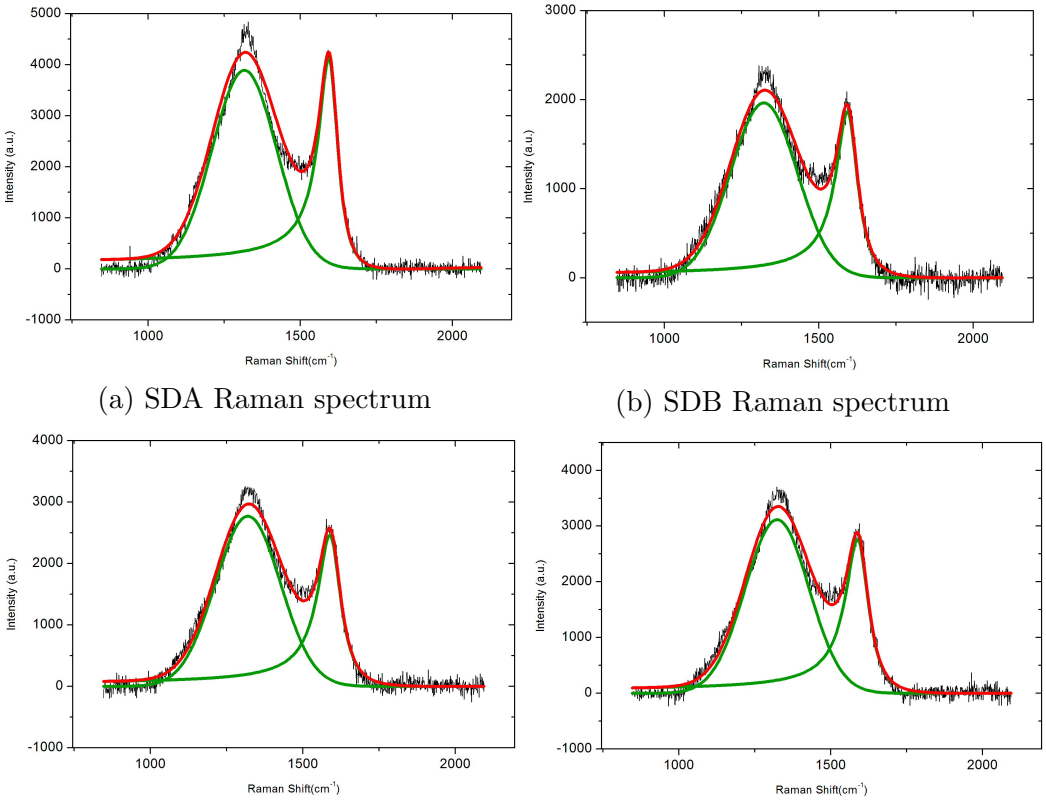

(a) SDA Raman spectrum

(b) SDB Raman spectrum

(c) SDC Raman spectrum

(d) SDD Raman spectrum

Figure 5.12: Raman spectra collected at with a 647 nm laser showing the Gaussian and BWF peaks fitted.

647 nm	Peak	Fit Type	Peak Centre	FWHM	I(D)/I(G)	R^2
SDA - 0% N	D	Gaussian	1315.88	248.98	0.939	0.985
	G	BWF	1590.37	81.17		
SDB - 0.41% N	D	Gaussian	1321.70	254.21	1.053	0.981
	G	BWF	1589.37	89.83		
SDC - 2.39% N	D	Gaussian	1319.48	251.20	1.125	0.985
	G	BWF	1585.48	94.69		
SDD - 3.84% N	D	Gaussian	1323.07	246.90	1.129	0.986
	G	BWF	1585.26	95.86		

Table 5.4: Quality and results of peak fitting performed on red laser Raman spectra

The 647 nm laser wavelength results show a steadily increasing I(D)/I(G) ratio as measured with respect to peak heights. This is indicative of the increasing disorder of the samples as more nitrogen is introduced. The increasing size of the D peak is driven by the increase in the number of defects present. The dispersion of the D peak with laser energy ensures the peak produced here is much larger than the G peak. The data collected with the 514 nm laser shows broadly the same features, however the incident laser wavelength creates a much smaller D peak [121]. Nitrogen induced disorder was also found in MWCNTs where sp^2 bonded nitrogen caused the formation of vacancies and deformed rings [122]. A similar process is driving the I(D)/I(G) ratio in the CMS samples.

The movement of the G peak centre to lower Raman shifts while the I(D)/I(G) ratio is increasing does not fit the amorphitization trajectories proposed by Ferrari et al. The G peak position is affected by two opposing movements. The peak should move to higher Raman shifts due to the increased clustering caused by the disorder. This is potentially caused by the appearance of a small D' peak at the base of the G peak which is not large enough or shifted enough from the main G peak to be discernible. The broadening of the G peak identified by its increasing FWHM is evidence of a possible increasing bond disorder, which would shift the G peak to lower wave numbers. When this combines with the presence of the D' peak the G peak would appear stretched. Some sp^3 bonding could encourage also the G peak to move to lower Raman shifts by introducing greater bond disorder and softening the VDOS of the graphite lattice [79] [123] [121]. These competing processes promote the G peak position to change very slowly or remain fixed. This phenomenon is also present in the 514.5 nm data.

Results for the 514 nm experiments are shown in Fig 5.13 and Tbl 5.5. The small I peak at $\approx$1150 nm is a common feature which was large enough to be deconvoluted and fitted separately to the main D peak. It has been identified with the presence of sp^3 carbon bonds associated with the presence of trans-polyacetylene, a likely possibility given the use of acetylene as a precursor

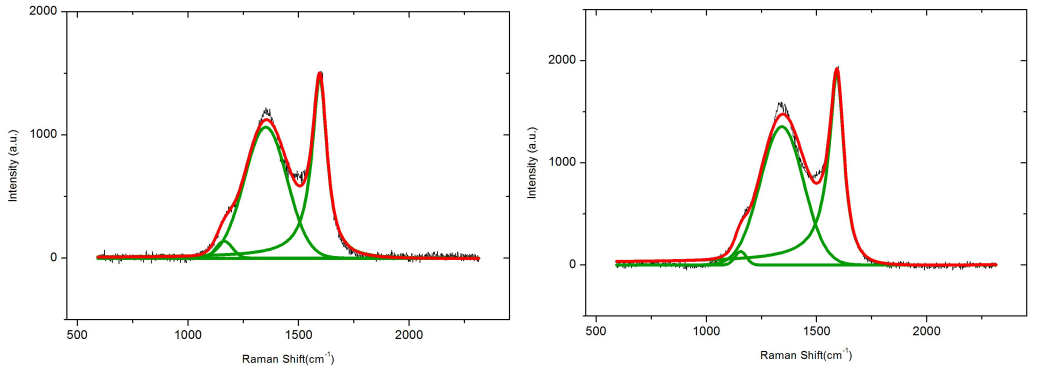

(a) SDA

(b) SDB

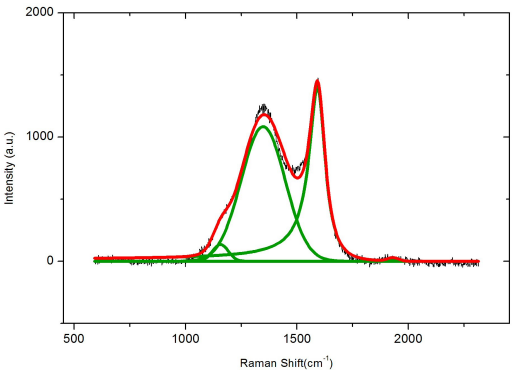

(c) SDC

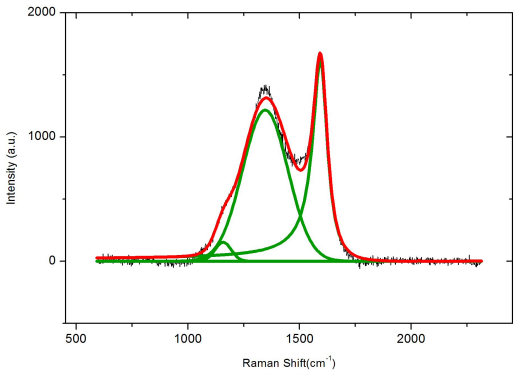

(d) SDD

Figure 5.13: Raman spectra collected at with a 514.5 nm laser showing the multiple fitted peaks

514 nm	Peak	Fit Type	Peak Centre	FWHM	I(D)/I(G)	R^2
SDA - 0% N	D	Gaussian	1351.18	226.56	0.72434	0.992
	G	BWF	1594.89	82.78		
	I	Gaussian	1163.20	86.81		
SDB - 0.41% N	D	Gaussian	1342.14	230.26	0.72256	0.993
	G	BWF	1590.38	84.06		
	I	Gaussian	1155.12	61.20		
SDC - 2.39%N	D	Gaussian	1348.02	231.52	0.77095	0.993
	G	BWF	1590.35	89.01		
	I	Gaussian	1156.16	83.60		
SDD - 3.84%N	D	Gaussian	1346.05	239.45	0.75175	0.992
	G	BWF	1591.47	81.77		
	I	Gaussian	1157.35	86.57		

Table 5.5: Quality and results of peak fitting performed on green laser Raman spectra

during the CVD synthesis [124]. The FWHM of the D peak steadily increases with nitrogen content and is a sign of a greater distribution of phonon modes driven by disorder in the sample [123]. The G peak position appears to remain relatively stable across the samples and is only substantially different for SDA. The most interesting feature of the data is the changes in I(D)/I(G) ratio. The ratio retains the overall direction demonstrated in the red laser results, with increasing I(D)/I(G) ratio with nitrogen content which is also in good agreement with the literature [107]. Interestingly however the samples SDB and SDD show slight decreases in the ratio as compared to their immediate predecessors. This could be driven by increased sp^3 bonding increasing the bond disorder which can reduce the number of active RBM sites. The protrusions from the spheres in both these samples lend credence to this hypothesis.

5.2.2 Characteristic lattice size

As a consequence of the D peak's source being tied to the edge defects of a graphitic lattice, the average lattice size is a quantity that can be derived

directly from the I(D)/I(G) ratio. Two mathematical regimes exist for calculating the diameter of lattice sites depending on their size. When I(D)/I(G) is increasing with increasing disorder i.e. the disorder is activating more rings than it is destroying, the equation that describes the lattice site size L_a is given by:

$$\frac{I(D)}{I(G)} = \frac{C(\lambda)}{L_a} \tag{5.7}$$

This is known as the Tuinstra Koening (TK) equation [77] where $C(\lambda)$ is a constant that is dependent on the incident laser energy. In the case of a green laser C(514 nm) = 4.4 nm. A more general equation was developed for the lattice site size by Cançado et al [80] which accounts for the dispersion caused by the laser energy given by:

$$L_a = (2.4 \times 10^{-10})\lambda_{laser}^4 \left(\frac{A_D}{A_G}\right)^{-1} \tag{5.8}$$

In this case, the quantity A_D/A_G is the integrated intensity of the D and G peaks. In this case the formula applies to the ratios of integrated areas of the peaks. The area ratios and intensity ratio, while related, can sometimes be driven by slightly different mechanisms. For example Ferrari et al [79] points out how in amorphous carbon, distortions to the aromatic rings broaden the D peak while its height is only a factor of the ordered rings. Rings of non-hexagonal structure tend to broaden the D peak while not contributing to its height. The presence of pyridinic heptagonal rings would therefore be accounted for by the area ratios and not by the intensity ratio. Another important point when using the area ratios is that the BWF function is inappropriate to use due to the asymmetry of the peak which would overemphasise the size of the G peak. The BWF fits are appropriate when discussing I(D)/I(G) ratios as the heights of the peaks are correctly represented. The choice of function used for fitting is driven by accurate data reproduction and does not contain any physical meaning. In general when

Sample	I(D)/I(G)	TK L_a	A_D/A_G	Cançado L_a
SDA	0.724	6.07 nm	2.64	6.34 nm
SDB	0.723	6.09 nm	2.74	6.12 nm
SDC	0.771	5.71 nm	2.90	5.77 nm
SDD	0.752	5.85 nm	3.01	5.57 nm

Table 5.6: Table of Lattice size as calculated via the TK and Cançado equations. The fits chosen used in the calculations were a BWF+Gaussian for the TK calculation and a Gaussian+Gaussian for the Cançado due to the symmetry requirement for this equation. This calculation was performed using the 514 nm laser data

doing calculations with Eqn. 5.8 a symmetric peak is required. The crystal lattice sizes are calculated using both methods with the peak results shown in Tbl. 5.6.

As can be seen from the table, the two calculations are in close agreement. These lattice sizes are also in good agreement with the sphere surface flake sizes in the literature which are generally reported to be between 2 nm and 10 nm [4]. This implies that Raman spectroscopy can be used to determine the quality of the flakes produced on carbon spheres during synthesis.

While the above calculation is indicative of the general size of the flakes, the results should be viewed with some qualifications. The TK equation was developed to describe increasing disorder from a pure graphite to a nanocrystalline graphite, effectively restricting it to exclusively sp^2 hybridised carbon samples, which would not factor in sp^3 hybridisation. The ratios can also be driven by the other impurities and disorder which are not tied strictly to edge defects. Nevertheless, this calculation shows that it is likely that the flake sizes are slightly reduced by nitrogen incorporation. TEM imaging could be used to confirm the effect of nitrogen on the graphitic flakes. The classic TK equation shows lattice sizes for SDB>>SDA and SDD>>SDC contrary to the Cançado equation. As discussed previously, this is likely due to the intensity ratio not accounting for the presence of pyridinic defects, which are significant in SDB and SDD as shown in Tbl 3.2.

5.3 Electron Paramagnetic Resonance spectroscopy

5.3.1 Room temperature characterisation

The CMS samples were characterised at room temperature using continuous wave EPR. The samples were carefully measured to ensure equal quantities were placed in to the sample tubes. This allowed the determination of the relative spin density for each of the samples. This in turn created a calibration curve for the spectrometer signal strength vs sample spin density which was used to estimate the nitrogen content of unknown samples [125]. A set of signal examples is shown in Fig 5.14 showing the relative sizes of the ESR signals. One feature which is clearly visible is that the size of the signal appears to decrease with decreasing nitrogen content. The nitrogen functional groups create paramagnetic spin sites through the addition of an extra electron to the carbon lattice. SDA represents an exception, likely caused by the presence of alternative functional groups. The elemental analysis data in Tbl 3.1 does point to this possibility as SDA has the greatest mass unaccounted for by carbon or nitrogen, which could be due to oxygen functionalities.

The g value shift of each of the samples was determined using an EPR marker DPPH which was introduced using a second NMR quartz tube inserted within the tube containing the sample. This created a second paramagnetic signal in proximity to the signal from the samples themselves. Deconvolution was achieved with a code developed with Matlab in-house as shown in appendix B. A second deconvolution was also completed using peak fitting software on the integral of the EPR signal in order to ensure the software was performing correctly. An example of a convoluted signal is shown in Fig 5.15.

The resulting g value was calculated by noting that both samples must be experiencing the same incident excitation radiation frequency. The expression for the new g value can be determined from the difference in centres of the

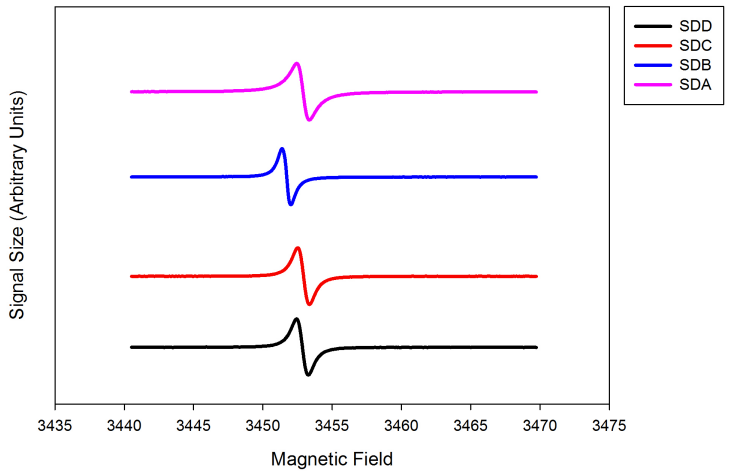

Figure 5.14: Example ESR spectra for the four CMS samples being studies.

	g value	Δ B (G)	A/B
SDA	2.00281	0.9385	1.0081
SDB	2.00272	0.6451	1.0247
SDC	2.00274	0.8799	1.0086
SDD	2.00281	0.8211	1.0299

Table 5.7: ESR spectral elements of CMS sample at room temperature. The assymetry ratio follows the same pattern as the conductivity presented earlier as is consistent with Dyson's theory regarding conductive samples.

resonance lines. The g-value appears to shift further from the free electron g value.

$$g_{cms} = g_{DPPH}\frac{B_{DPPH}}{B_{cms}} \tag{5.9}$$

The combination of all the spectral elements are presented in Tbl 5.7.

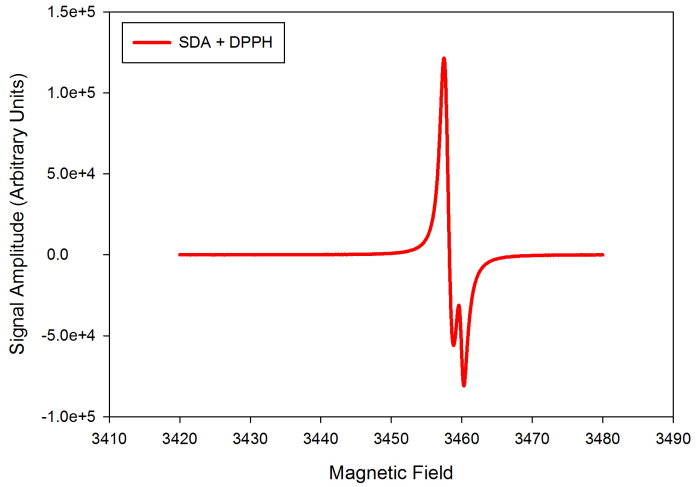

Figure 5.15: A combination of SDA and DPPH ESR spectra taken with one sample placed within the other. Deconvolution allows for a precise determination of the unknown samples g-value.

5.3.2 Power Saturation

A power saturation experiment was completed at room temperature to determine the relaxation rate of the spins in the CMS samples. It also represents preliminary work for a set of power saturation measurements at lower temperatures, which may be used to further elucidate the results of electron transport measurements, as shown in the literature [126]. Limitations of the low temperature resonant cavity did not allow for power of the saturation experiments at low temperatures.

Power saturation behaviour is determined by the rate at which the sample relaxes after excitation. The sample becomes saturated when the number of excited spins is maximised. This occurs when the relaxation rate is smaller than the rate of incoming microwave photons. As such it is a useful technique to probe the relaxation rates of samples in the absence of pulsed ESR spectroscopy.

Samples can undergo either homogeneous or inhomogeneous broadening depending on the source of the EPR signal. A theoretically derived example of a homogeneously broadening signal is shown in Fig. 5.16 where X is defined as:

$$X = \gamma B_1 \sqrt{T_1 T_2} \tag{5.10}$$

γ and B_1 are the gyromagnetic ratio and the magnetic field of the incident microwave radiation.

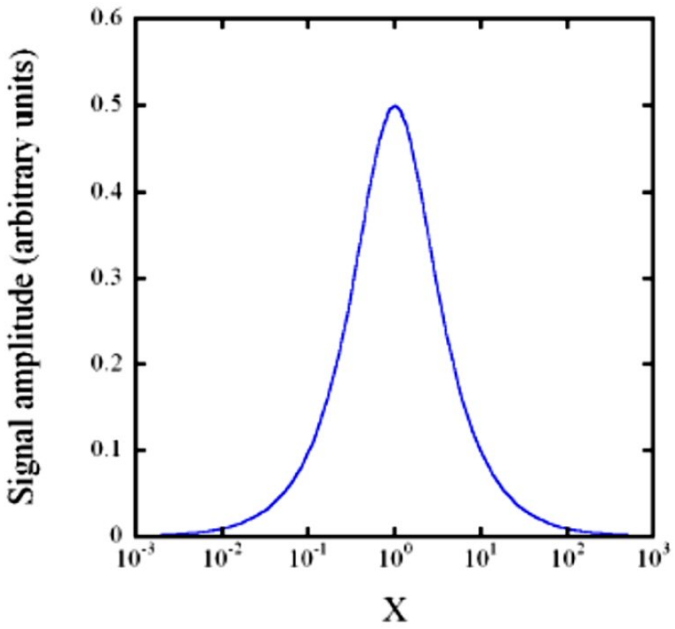

Figure 5.16: A theoretical model of a homogeneously broadening EPR signal [127].

Room temperature results for the CMSs are shown in Fig 5.17. It is clear that within the power levels explored, full saturation did not occur and that the samples are divergent. At lower power levels the response of the sample with increasing power is linear. At higher power levels saturation begins to slow the response until the sample appear to tend towards a constant value. No

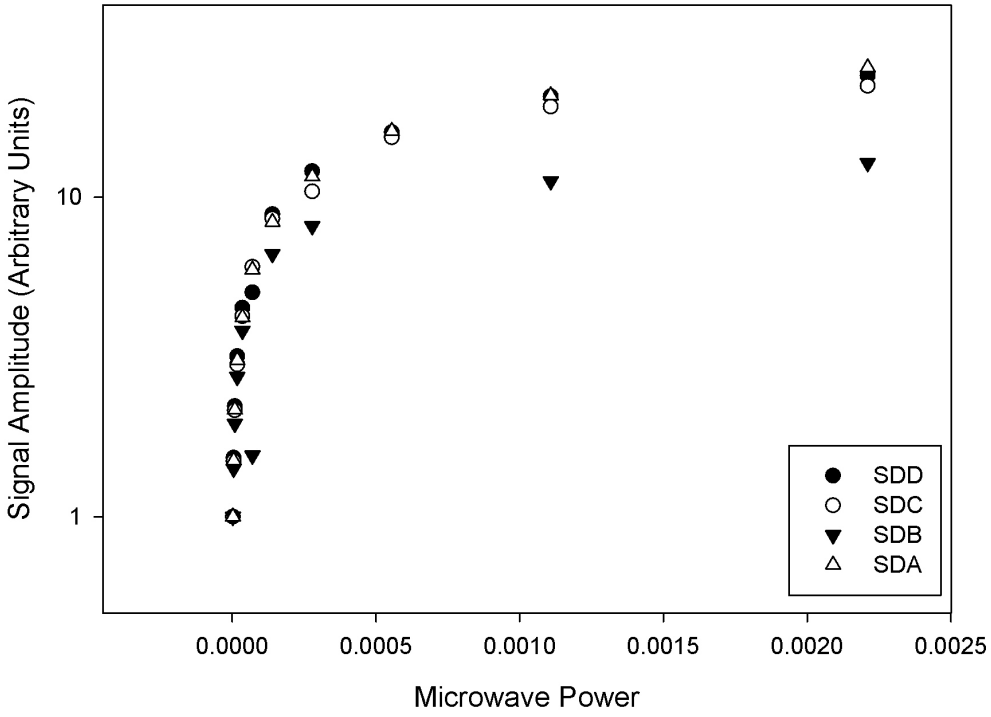

Figure 5.17: The signal response of the CMS samples with increasing incident microwave power. SDB saturates more sharply than the other samples.

maximum is present, which would allow for the calculation of the relaxation rates.

$$\Delta M(T) = \frac{X}{(1+X^2)^{1/2}} \tag{5.11}$$

Castner et al [127] described the inhomogeneous broadening mathematically with Eqn 5.11. Unfortunately without complete saturation a determination of the relaxation times is not possible. A set of low temperature readings would still be relevant, firstly because the changes in T_1 would significantly change the saturation profile, and secondly the susceptibility can be used to determine the number of carrier spins. This provides another methodology

to understand the conduction mechanisms involved outlined by Rice et al [126].

5.3.3 Low temperature

In preparation for low temperature ESR experiments equal quantities by mass of CMS samples were packed in NMR quartz glass tubes. Spectral parameters were obtained at each temperature by using an in-house data processing code built in Matlab, available in Appendix B. Spectrometer parameters and incident microwave power were kept constant at all temperatures investigated.

Signal amplitude

The signal amplitude (ΔM) was extracted from each spectra and normalised with respect to 300K. The results are shown in Fig 5.18 for 3 samples with nitrogen present on a 1/T scale. At high temperatures the amplitude changes linearly against 1/T. This is consistent with the Curie law where:

$$\Delta M(T) = A + B_z \left(\frac{1}{T}\right) \tag{5.12}$$

The gradient of the linear component is related to the resonant spin density. Since equal quantities of sample were packed within the each NMR tubes, the ratio of B_z value represent the ratios of paramagnetic spins. A comparison of the spin density with the XPS data demonstrates that the nitrogen incorporation is largely the source of the EPR signal. Other functional groups, such as those based on oxygen, can also contribute to the ESR signal hence the B_z ratio is comparable to the quantity of non-carbon atoms detected via XPS. The results of the linear regressions are shown in Tbl 5.8. The ESR ratios appear slightly less than the XPS ratios presented. A likely cause is

that the nitrogen and oxygen can form ESR silent functionalites. For example, molecular interstitial forms of the elements should not present any ESR signal while still being included in the elemental analysis data. Another potential source of discrepancy could be due to the changes in skin depth due to the changes in conductivity of the samples w.r.t. temperature. As discussed earlier, this may have more to do with the structure of the doping rather than its quantity. This phenomenon may be the cause of the under reported doping level in SDC as compared to SDB and SDD given its lower conductivity. Lastly, the split level in the linear portion, shown in more detail in Fig 5.19, is due to hysteresis with the lower set of values (even temperatures) representing the downward run while the upper values (odd temperatures) are the returning upward run.

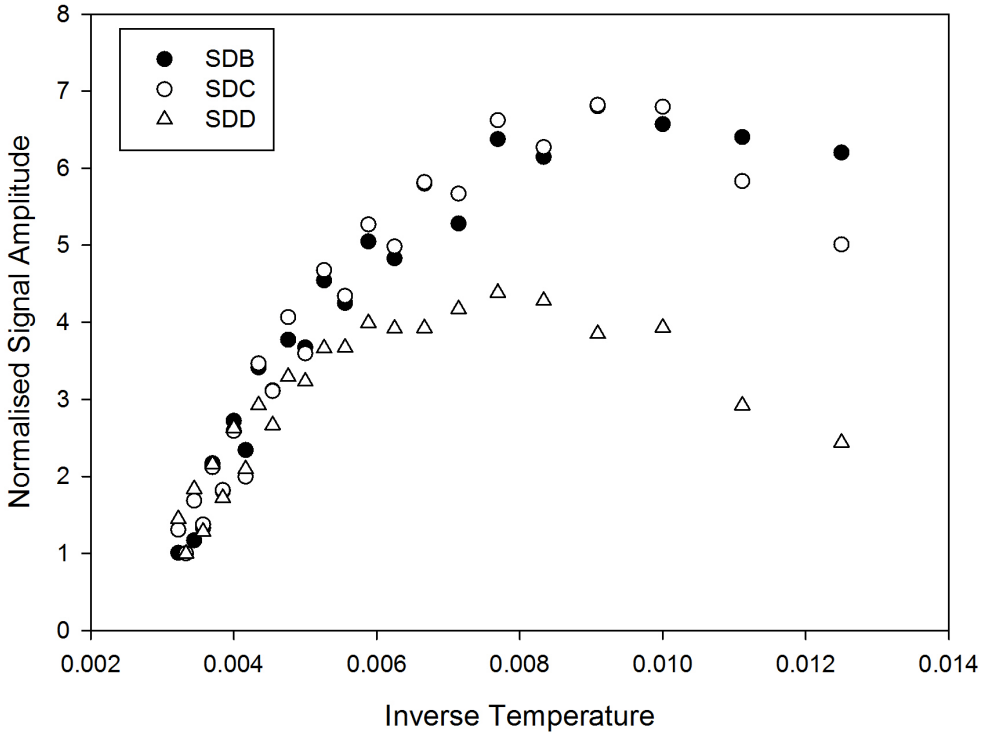

Figure 5.18: The normalised signal amplitude change with respect to temperature of nitrogen doped CMS samples

	SDB	SDC	SDD
ESR	558.24 ± 91.2 1±0.16	1056.34±95.5 1.89±0.09	1203.21±172 2.16±0.15
XPS	3 % 1	7 % 2.33	8 % 2.66

Table 5.8: Curie Law B_z ratios compared to the percentage non-carbon elements detected via XPS. This shows that a majority of non-carbon doping elements contribute to the ESR response.

The low temperature saturation is due to the spin-lattice relaxation rate decreasing with decreasing temperature. The samples with higher functionalite content are affected at higher temperatures and have a steeper decline in signal strength. This hints at the possibility that the samples with greater paramagnetic defects have relaxation rates which are larger than their undoped counterparts. A full set of pulsed EPR measurements would confirm this.

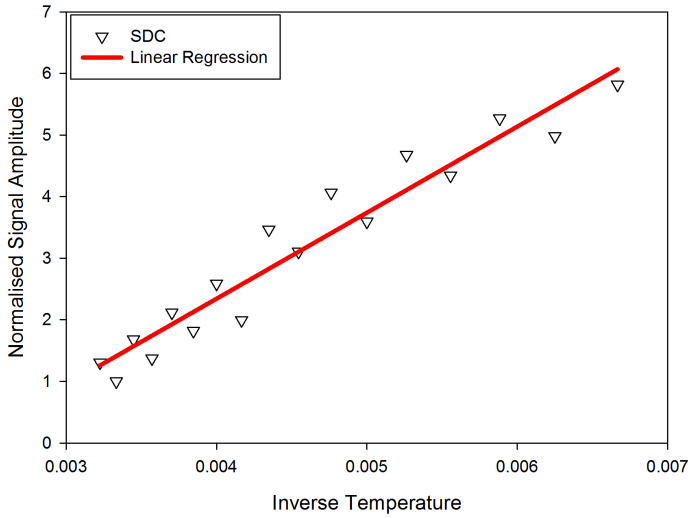

Figure 5.19: An example of the linear regression applied to the high T data from SDC ESR measurements.

Linewidth

As previously discussed the linewidth is related to the effective relaxation time, which itself is composed of the contributions of all the relaxation mechanisms present in a sample. The dominant relaxation mechanism responsible for the observable changes in the linewidth is likely to be the spin-lattice relaxation. The Korringa relation governs this process:

$$\Delta B = 1/T_{eff} \tag{5.13}$$

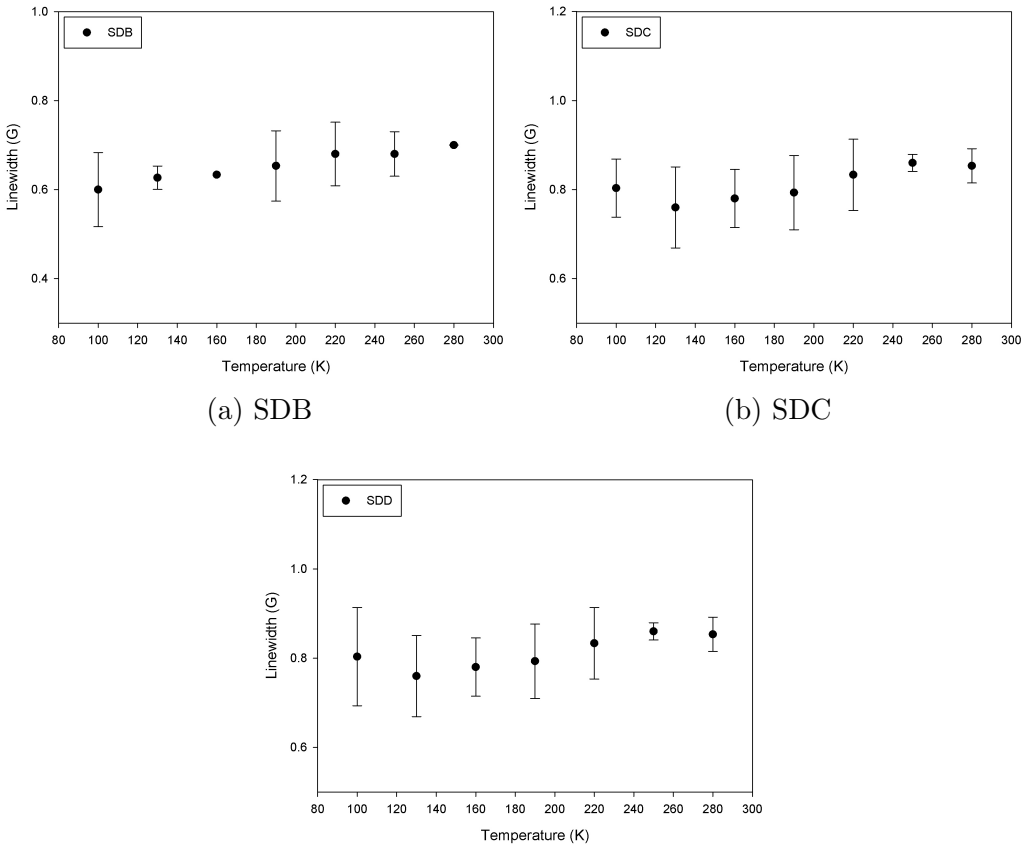

(a) SDB

(b) SDC

(c) SDD

Figure 5.20: The linewidth of ESR signal for 3 CMS samples against temperature.

The results for the samples in question are shown in Fig 5.20. Large error bars are present due to the difficulty in tuning the low temperature spectrometer cavity, the settings were selected such that they would not need changing during the experiment. The signal drift, caused by shifting g-values with lower temperatures, forced the use of a wide sweep to keep the signal in the detection range. This reduced the resolution causing large errors in the measured linewidth. The linewidth appear to remain relatively fixed throught the temperature range with only a very slight downward trend. The two samples with greater nitrogen content do appear to show a slight upturn to the linewidth at low temperatures however due to the large errors present no firm conclusions may be drawn.

Asymmetry ratio

The asymmetry of the samples is shown in Fig 5.21. The asymmetry is indicative of the number of charge carriers in the system, as described in Chapter 2, and characterises the Dysonian lineshape [85]. At high temperatures the asymmetry decreases rapidly approaching 1. The ratio then appears to turn upwards, albeit at a slower rate below 140K.

Of note, the increased nitrogen incorporation causes a steeper "U" shape to the asymmetry which indicates improved conduction at high temperatures. The resistivity, however increases with increasing temperature due to metallic scattering, shown in Fig 5.4. A possible explanation for this apparent contradiction between resistivity and asymmetry ratio is the location of the conduction being measured. The asymmetry ratio arises from conduction of spins on the surface of a sample, characterised by its skin depth, as described by Dyson et al [85]. In this case, skin depth is probably restricted to the graphitic flakes which compose the sphere. An increase in nitrogen content causes the conduction to increase, probably due to the extra electron donated by the nitrogen dopant, which is supported by the g-values in Tbl

5.7. Higher temperatures are likely aiding in delocalising these spins from their nitrogen atoms, thus increasing the conductivity with temperature.

On the other hand, resistivity is measured over the bulk of the sample by applying an external electric field. Therefore, the conduction being probed involves both the movement of electrons over the sphere as well as their ability to travel between them. While nitrogen incorporation does improve the overall conductivity as shown in 5.2 the response of the conductivity with temperature is opposite to that shown by the asymmetry ratio. The metallic upturn reduces the conductivity of the spheres. It is therefore probable that the metallic upturn is related to the intersphere conduction mechanisms and not the intrinsic conduction of the individual spheres. The same process is likely taking place in the CNT networks reported in the literature [49] [128].

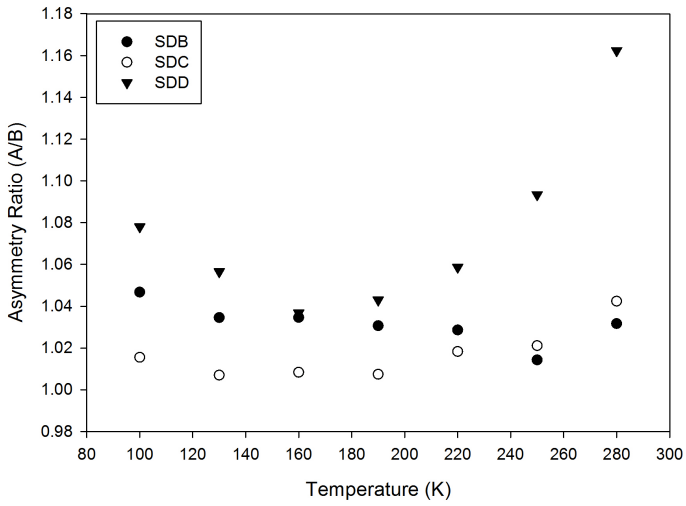

Figure 5.21: The asymmetry of the resonance line vs. temperature for all the 3 samples. The high nitrogen samples present greater asymmetry than those with low nitrogen incorporation.

Previous research on carbonaceous materials has showed that the assymetry ratio of a graphitic compound decreases with compression and grinding. This was due to the particulates reducing the effective skin depth of the sample [129] as shown in Fig. 5.22. The CMS samples represent a highly "ground"

material as particles range in size from 100 nm to 1 μm. The asymmetry may potentially be indicative of average sphere size in the sample. If the conclusion derived above is true, a reduction in spin conductivity with grinding is driven by increasing the number of interparticle contacts by increasing the number of edges present.

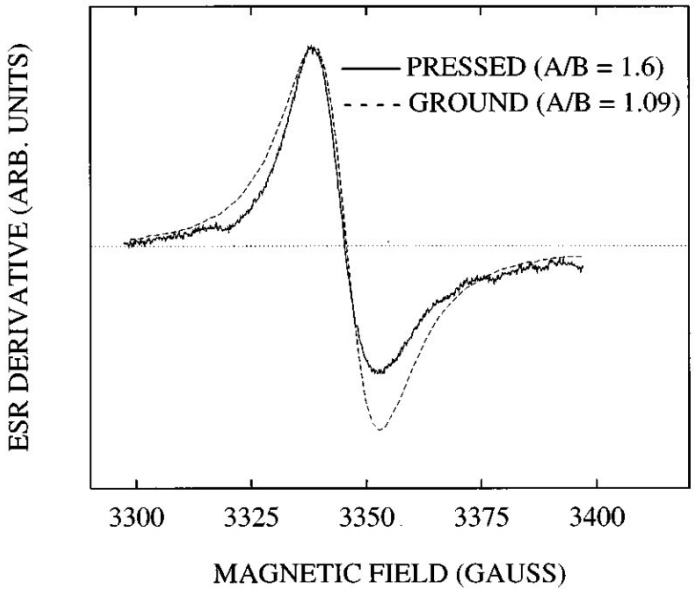

Figure 5.22: The reduction of the assymetry ratio of a CNT sample with grinding from research conducted by Petit et al [129].

Chapter 6

Conclusion

This chapter will summarise the data collected, along with the conclusions that have been drawn for each technique separately. By combining the information from the different techniques some overall conclusions can be reached. Possible future research will be discussed, along with alternative research directions.

6.1 Summary of results

Four samples of nitrogen doped CMSs were successfully synthesised by Sibongile Dube in the school of Chemistry at the University of the Witwatersrand using a horizontal CVD reactor. The samples were prepared with varying quantities of acetonitrile precursor present to provide a source of nitrogen, producing varying levels of doping. Preliminary characterisation of the samples using XPS and SEM techniques confirmed the spherical shape of the carbon samples and the quantity of nitrogen doping.

XPS data, produced by the School of Chemistry, showed that increasing the number of nitrogen doping atoms caused the proportion of pyridinic nitrogen

to increase in all the samples. At low nitrogen incorporation some pyrollic nitrogen could be present, however none was detected in samples with higher concentration. It is likely that the ambiguity surrounding the pyrollic nitrogen is due to the signal-to-noise ratio present in samples with low nitrogen content. The diminished peak fitting accuracy renders definitive exclusion of pyrollic nitrogen impossible, however, given its absence in nitrogen rich samples, its presence is unlikely.

Images of the samples were created using a Scanning Electron Microscopy, confirming the presence of spheres and the success of the synthesis technique, with average sphere diameters around 1 μm. Varying levels of disorder did not correlate with doping level. A possible connection between the proportion of pyridinc nitrogen and structural disorder exists, however this would require further investigation. This lack of correlation suggests that other synthesis parameters are more significant than the acetonitrile precursor level in determining sphere quality. In samples with greater disorder, the presence of small spheres (<100 nm) was also detected, possibly indicating a change in the availability of curved graphitic flakes which are necessary to the formation of larger spheres. Protrusions from the spheres of SDB and SDD were also detected.

Raman spectroscopy was completed at two laser wavelengths, namely 514 nm and 637 nm. The evolution of Raman spectral elements with increasing nitrogen dopant reveal that changes in structure do occur with nitrogen doping. An increase in the RBM in the graphitic lattices, detected as an increase in the I(D)/I(G) ratio, indicates increasing edge defects in the samples. This was matched to a possible decrease in the average graphitic flake size caused by the nitrogen incorporation. Nitrogen incorporation also encourages the formation of non-hexagonal rings which would also contribute to the Raman spectral elements. A lack of movement of the G peak could be indicative of some sp^3 hybridised bond formation with nitrogen incorporation. The G peak's natural tendency to move to higher Raman shifts with sp^3 incorporation is opposed by the increased clustering as more edge defects are created.

The broadening of the G peak could be attributable to the formation of a D' peak but this peak was not large enough to be distinguishable.

Electron Paramagnetic Resonance technique were used to probe the spin sites present in the samples to better understand the chemical environment of the nitrogen incorporation. While alternative spin sites are present in structured carbon materials such as oxygen functionals and dangling bonds, a large proportion of the spin paramagnetism is sourced from the nitrogen doping. This is confirmed by the fit of the Curie Law to the data correlating with the number of non-carbon elements detected via XPS. The asymmetry ratio, an indication of the sample's conductivity, qualitatively matches the conduction results with the appearance of a "U" shape change with temperature. Spin relaxation times were probed with power saturation measurements, however a lack of saturation at room temperature prevented their estimation, and pulsed EPR techniques will have to be employed.

Room temperature EPR experiments also show that the g value of the samples moves away from the free electron g-value with nitrogen incorporation. One possible cause is the localisation of the electrons around nitrogen sites, increasing the interaction between the electron and the lattice. The asymmetry ratio also confirms the conductivity results between the samples, with the lower conduction samples presenting less asymmetry than higher conduction samples. An important point to note is that the lack of hyperfine structure shown in the results is due to the powder nature of the sample and the random orientation of the spin sites generating an averaged signal.

Electrical transport measurements were conducted using equipment assembled for the purpose as part of this study. The electrical transport station was designed to perform the Van der Pauw, IV and Hall effect measurements with integrated temperature control and automated data acquisition. A Labview program monitored the overall experiment and interfaced with the measurement equipment to record the data. An Arduino controlled multiplexer controlled the orientations of the connecting leads through a bank of relays as well as the movement of a stepper motor in the cryostat insert. The

Arduino controlled multiplexer also contained a high precision operational amplifier circuit to deliver the voltage for the IV characterisation curves which could be controlled from the Labview control code over the serial connection. Custom designed cryostat inserts were constructed in the School of Physics mechanical workshop. Custom sample chambers were designed and constructed on a 3D printer to achieve consistency and reproduceability of results for all samples and uniform pressure throughout the test lamella.

Resistivity measurements showed that the powder samples were semiconducting in the temperature ranges investigated. While not immediately obvious, the samples also reproduced a metallic upturn at higher temperatures which was also detected in previous research on similar samples. Good agreement between the two VDP sample chamber geometries and the reproducibility of the results showed that the experiment was successful in measuring the intrinsic resistivity of the powders. A number of models were tested against the data, namely VRH, ESVRH and FAT with and without the low temperature weak localisation correction. Due to the low temperature dependence of the resistivity of the samples, an effect likely caused by the synthesis temperatures of the spheres, all the models investigated produced excellent fits to the experimental data. To isolate a likely candidate for the conduction mechanism the logarithmic derivative of the resistivity was compared to the logarithm of the temperature. If any of the variable range hopping models were dominant a specific gradient would highlight which was active in the sample, and any transitions. The gradient did not match any of the VRH models while Fluctuation Assisted Tunnelling accurately described the data. FAT is therefore the most likely conduction mechanism in CMSs. Qualitative comparison of IV curves matches those of previous work on the subject, characterised by increasing non-linearity with decreasing temperature. This further confirmed the likelihood that FAT is the dominant conduction mechanism. The possibility that multiple models are active in the samples cannot be excluded and it is likely that different models describe the intersphere and intrasphere conduction.

The fit of the FAT model showed that the nitrogen incorporation can improve or impede the conduction electrons by changing the shape and height of the potential barriers in the material. This is likely connected to the structure of the spheres and the way in which electrons transfer between spheres. In general the inclusion of nitrogen appears to reduce the number of insulating areas, likely by doping the graphitic flakes which form the spheres. It also increases the temperature at which thermal fluctuations become significant, likely due to its localising effect on the wave function. High accuracy measurements performed around the T_s temperatures may reveal what the conduction mechanism dominates below the FAT activation temperature.

Hall Effect measurements determined that the increase in nitrogen dopant increased the number of majority charge carriers, in this case electrons. This matches what is expected with nitrogen substitution in to a graphitic lattice, with the nitrogen contributing an extra electron to the system. Limits to the sensitivity of the equipment used and the upper limit of the applied magnetic field of 1.1 T resulted in large errors, permitting only a qualitative understanding of the majority carrier behaviour.

6.2 Inter-technique conclusion

Many of the techniques discussed above investigate different elements of the samples however many of them complement each other. What follows is a discussion of where the various techniques corroborate each other and what their combined data reveals.

Raman spectroscopy and XPS are often combined in understanding the structure of a sample and how it is influenced by the bonds which are present. The increasing proportion of pyridinic nitrogen is paralleled in the Raman data as an increasing I(D)/I(G) ratio. Pyridinic nitrogen is an edge defects while graphitic nitrogen can be found within the graphite flakes. The presence of pyridinic nitrogen may be causing the growth of the flakes to be stunted as it

impedes growth beyond its formation. This could then cause the crystallite size of the flakes to be limited. The presence of protrusions from the SDB and SDD samples, observed via SEM, is mirrored in the Raman I(D)/I(G) ratio and the higher proportion of pyridinic nitrogen compared to SDC in the XPS data. This points to the synthesis conditions of SDB and SDD encouraging the formation of less graphitic bonds, both pyridinic and sp^3 "diamond-like" bonds could encourage out-of-plane growth from the graphitic lattice. These samples also possess lower resistivity than SDC, suggesting that the out-of-plane bonds assist with conduction, likely by improving the ability of electrons to pass between spheres. Disruptions to graphitic lattices can also improve the interlayer coupling, also improving the conduction between layers of graphite. Investigations at low Raman shifts would be invaluable in determining the coupling between layers. The above conjecture is further supported by the ESR measurements. The assymmetry ratio, an indication of the conductivity of the spins, highlights the source of the metallic upturn in resistivity as the intersphere conduction.

In conclusion the results collected point towards the sphere's individual structure determining their bulk properties. Creating spheres with specific properties cannot be achieved via nitrogen doping alone. Isolating the synthesis parameters which create the protruding structures and the associated internal changes of the spheres is fundamental to tuning their properties for industrial applications.

6.3 Future work

While this research reveals some of the relationship between the nitrogen doping of CMSs, their structure and their electrical transport mechanisms many avenues of future investigation exist.

High temperature conductivity experiments should be conducted to determine the exact nature of the metallic term. The data only records its early

onset and therefore any deeper understanding would require a larger range of temperatures. Sample chambers for use in high temperature settings would need to be constructed from a different material due to the melting point of PLA.

High accuracy low temperature (<10K) investigation would reveal the exact onset of FAT model producing an improved estimation of the T_s term for the FAT model. Low temperature readings could also reveal if other conduction mechanisms are present in the spheres.

Adding an AC source to the Hall Effect apparatus would reduce thermal drift and allow for the majority carrier species and density to be determined more accurately.

The most useful experiment to determine the source of the FAT conduction would be to measure the resistivity and IV behaviour of a single sphere placed between two contacts. The possibility exists to do this with two nanomanipulators in an SEM with electrical leads attached. Alternatively a bath of mercury as has been used to measure the ballistic transport of CNTs [43] and can be employed for CMSs. The relatively large size of the spheres renders this experiment facile.

Low Temperature power saturation EPR experiments would help indicate the relaxation rates and more importantly discern if the resonant spins are indeed the conduction electrons, as shown in other work on carbon structures [126]. This was not possible due to the limitations of the low temperature resonant cavity.

Raman spectroscopy at additional laser wavelengths can sometimes reveal further structural information. Of particular interest would be the behaviour of the G' peak as it is composed of a combination of the D and G peaks and can confirm the speculation regarding the G peak position. Investigations of the LBM of graphene currently underway [130] could be used to determine the quantity of nitrogen intercalated between layers.

The same techniques employed in this thesis can be applied to hollow CMSs. Such an investigation would confirm whether the internal structure of the sphere has a significant impact on the macroscopic properties of the material.

References

[1] S. Iijima. Helical microtubules of graphitic carbon. *Nature*, 1991.

[2] Y. Z. Jin, Y. J. Kim, C. Gao, Y. Q. Zhu, A. Huczko, M. Endo, and H. W. Kroto. High temperature annealing effects on carbon spheres and their applications as anode materials in Li-ion secondary battery. *Carbon*, 44(4):724–729, April 2006.

[3] H. Kroto, J. Heath, S. O'Brien, R. Curl, and R. Smalley. C60: Buckminsterfullerene. *Nature*, 1985.

[4] Amit A. Deshmukh, Sabelo D. Mhlanga, and Neil J. Coville. Carbon spheres. *Materials Science and Engineering: Reports*, 70(1-2):1–28, September 2010.

[5] F. Su, X. S. Zhao, Y Wang, L. Wang, and J. Y. Lee. Hollow carbon spheres with a controllable shell structure. *Journal of Materials Chemistry*, 16(45):4413, 2006.

[6] V. G. Pol, M. Motiei, A. Gedanken, J. Calderon-Moreno, and M. Yoshimura. Carbon spherules: synthesis, properties and mechanistic elucidation. *Carbon*, 42(1):111–116, January 2004.

[7] M. Inagaki. Discussion of the formation of nanometric texture in spherical carbon bodies. *Carbon*, 35:711–713, 1997.

[8] S. V. Pol, V. G. Pol, D. Sherman, and A. Gedanken. A solvent free

process for the generation of strong, conducting carbon spheres by the thermal degradation of waste polyethylene terephthalate. *Green Chemistry*, 11(4):448, 2009.

[9] H. Kristianto, C. D. Putra, A. A. Arie, M. Halim, and J. K. Lee. Synthesis and Characterization of Carbon Nanospheres Using Cooking Palm Oil as Natural Precursors onto Activated Carbon Support. *Procedia Chemistry*, 16:328–333, 2015.

[10] J. Qiu, Y. Li, Y. Wang, C. Liang, T. Wang, and D. Wang. A novel form of carbon micro-balls from coal. *Carbon*, 41(4):767–772, January 2003.

[11] W. M. Qiao, Y. Song, S. Y. Lim, S. H. Hong, S. H. Yoon, I. Mochida, and T. Imaoka. Carbon nanospheres produced in an arc-discharge process. *Carbon*, 44(1):187–190, January 2006.

[12] X. He, F. Wu, and M. Zheng. The synthesis of carbon nanoballs and its electrochemical performance. *Diamond and Related Materials*, 16(2):311–315, February 2007.

[13] Z. L. Wang and Z. C. Kang. Pairing of Pentagonal and Heptagonal Carbon Rings in the Growth of Nanosize Carbon Spheres Synthesized by a Mixed-Valent Oxide-Catalytic Carbonization Process. *J. Phys. Chem.*, 3654(001):17725–17731, 1996.

[14] H. Kroto and K. McKay. The formation of quasi-icosahedral spiral shell carbon particles. *Nature*, 331:328–331, 1988.

[15] S. Iijima. Direct observation of the tetrahedral bonding in graphitized carbon black by high resolution electron microscopy. *Journal of Crystal Growth*, 35:675–683, 1980.

[16] Z. L. Wang and Kang Z. C. On accretion of nanosize carbon spheres. *J. Phys. Chem.*, 100, 1996.

[17] M. Wissler. Graphite and carbon powders for electrochemical applications. *Journal of Power Sources*, 156(2):142–150, June 2006.

[18] K. C. Mondal, A. M. Strydom, R. M. Erasmus, J. M. Keartland, and N. J. Coville. Physical properties of CVD boron-doped multiwalled carbon nanotubes. *Materials Chemistry and Physics*, 111(2-3):386–390, October 2008.

[19] Kartick C. Mondal, N. J. Coville, M. J. Witcomb, G. Tejral, and J. Havel. Boron mediated synthesis of multiwalled carbon nanotubes by chemical vapor deposition. *Chemical Physics Letters*, 437(1-3):87–91, March 2007.

[20] Y. Li, W. Zhou, H. Wang, L. Xie, Y. Liang, F. Wei, J.-C. Idrobo, S. J. Pennycook, and H. Dai. An oxygen reduction electrocatalyst based on carbon nanotube-graphene complexes. *Nature nanotechnology*, 7(6):394–400, June 2012.

[21] G. Lalande, R. Côté, D. Guay, P. Bertrand, L. T. Weng, and J. P. Dodolet. Is nitrogen important in the formulation of fe-based catalysts for oxygen reduction in solid polymer fuel cells. *Electrochimica Acta*, 42(9):1379–1388, 1997.

[22] D.-W. Wang and D. Su. Heterogeneous nanocarbon materials for oxygen reduction reaction. *Energy & Environmental Science*, 7(2):576, 2014.

[23] E. N. Nxumalo, P. J. Letsoalo, L. M. Cele, and N. J. Coville. The influence of nitrogen sources on nitrogen doped multi-walled carbon nanotubes. *Journal of Organometallic Chemistry*, 695(24):2596–2602, 2010.

[24] S. Majeed, J. Zhao, L. Zhang, S. Anjum, Z. Liu, and G. Xu. Synthesis and electrochemical applications of nitrogen-doped carbon nanomaterials. *Nanotechnology Reviews*, 2(6):615–635, January 2013.

[25] T. Kondo, S. Casolo, T. Suzuki, T. Shikano, M. Sakurai, Y. Harada, M. Saito, M. Oshima, M. I. Trioni, G. F. Tantardini, and J. Nakamura. Atomic-scale characterization of nitrogen-doped graphite: Effects of dopant nitrogen on the local electronic structure of the surrounding carbon atoms. *Physical Review B - Condensed Matter and Materials Physics*, 86(3):1–37, 2012.

[26] Y. Shao, S. Zhang, M. H. Engelhard, G. Li, G. Shao, Y. Wang, J. Liu, I. Aksay, and Y. Lin. Nitrogen-doped graphene and its electrochemical applications. *Journal of Materials Chemistry*, 20(35):7491, 2010.

[27] V. V. Strelko, V. S. Kuts, and P. A. Thrower. On the mechanism of possible influence of heteroatoms of nitrogen , boron and phosphorus in a carbon matrix on the catalytic activity of carbons in electron transfer reactions. *Carbon*, 38:1499–1503, 2000.

[28] S.-F. Huang, K. Terakura, T. Ozaki, T. Ikeda, M. Boero, M. Oshima, J.-I. Ozaki, and S. Miyata. First-principles calculation of the electronic properties of graphene clusters doped with nitrogen and boron: Analysis of catalytic activity for the oxygen reduction reaction. *Physical Review B*, 80(23):235410, December 2009.

[29] D. Yuan, J. Chen, J. Zeng, and S. Tan. Preparation of monodisperse carbon nanospheres for electrochemical capacitors. *Electrochemistry Communications*, 10(7):1067–1070, July 2008.

[30] F.-B. Zhang and H. Li. Synthesis of hollow carbon microspheres in ionic liquids and their electrochemical capacitance characteristics. *Materials Chemistry and Physics*, 98(2-3):456–458, August 2006.

[31] C.-W. Huang, C.-H. Hsu, P.-L. Kuo, C.-T. Hsieh, and H. Teng. Mesoporous carbon spheres grafted with carbon nanofibers for high-rate electric double layer capacitors. *Carbon*, 49(3):895–903, March 2011.

[32] Q. Li, R. Jiang, Y. Dou, Z. Wu, T. Huang, D. Feng, J. Yang, A. Yu, and

D. Zhao. Synthesis of mesoporous carbon spheres with a hierarchical pore structure for the electrochemical double-layer capacitor. *Carbon*, 49(4):1248–1257, April 2011.

[33] S. Han, Y. Yun, K.-W. Park, Y.-E. Sung, and T. Hyeon. Simple Solid-Phase Synthesis of Hollow Graphitic Nanoparticles and their Application to Direct Methanol Fuel Cell Electrodes. *Advanced Materials*, 15(22):1922–1925, November 2003.

[34] J. H. Kim, B. Fang, M. Kim, and J.-S. Yu. Hollow spherical carbon with mesoporous shell as a superb anode catalyst support in proton exchange membrane fuel cell. *Catalysis Today*, 146(1-2):25–30, August 2009.

[35] H.-J. Liu, S.-H. Bo, W.-J. Cui, F. Li, C.-X. Wang, and Y.-Y. Xia. Nano-sized cobalt oxide/mesoporous carbon sphere composites as negative electrode material for lithium-ion batteries. *Electrochimica Acta*, 53(22):6497–6503, September 2008.

[36] J. Schuster, G. He, B. Mandlmeier, T. Yim, K. T. Lee, T. Bein, and L. F. Nazar. Spherical ordered mesoporous carbon nanoparticles with high porosity for lithium-sulfur batteries. *Angewandte Chemie (International ed. in English)*, 51(15):3591–5, April 2012.

[37] Y. Liu, C. Cao, and J. Li. Enhanced electrochemical performance of carbon nanospheres–LiFePO4 composite by PEG based sol–gel synthesis. *Electrochimica Acta*, 55(12):3921–3926, April 2010.

[38] Y. Song, G. Zhai, G. Li, J. Shi, Q. Guo, and L. Liu. Carbon/graphite seal materials prepared from mesocarbon microbeads. *Carbon*, 42(8-9):1427–1433, January 2004.

[39] L. Nyemba. *Reinforcement of synthetic rubber with carbon nanoballs to produce nanocomposite ion exchange membrane*. PhD thesis, Faculty of Engineering and the Built Environment, 2010.

[40] Q. Xu, F. Yan, J. Lei, C. Leng, and H. Ju. Disposable electrochemical immunosensor by using carbon sphere/gold nanoparticle composites as labels for signal amplification. *Chemistry (Weinheim an der Bergstrasse, Germany)*, 18(16):4994–8, April 2012.

[41] M. Bockrath. Single-Electron Transport in Ropes of Carbon Nanotubes. *Science*, 275(5308):1922–1925, 1997.

[42] M. W. Bockrath, D. H Cobden, J. Lu, A. G. Rinzler, R. E. Smalley, L. Balents, and P. L. McEuen. Letters To Nature. *Transport*, 397(6720):4–7, 1999.

[43] Stefan Frank, Philippe Poncharal, Z L Wang, and Walt A De Heer. Carbon Nanotube Quantum Resistors. *Science*, 280(June):1744–1746, 1998.

[44] J. E. Fischer, H. Dai, A. Thess, R. Lee, N. M. Hanjani, D. L. Dehaas, and R. E. Smalley. Metallic resistivity in crystalline ropes of single-wall carbon nanotubes. *Physical Review B*, 55(8):R4921–R4924, 1997.

[45] J. Vavro, J. Kikkawa, and J. Fischer. Metal-insulator transition in doped single-wall carbon nanotubes. *Physical Review B*, 71(15):155410, April 2005.

[46] A. B. Kaiser, G. C. Mcintosh, K. Edgar, J. L. Spencer, H. Y. Yu, and Y. W. Park. Some problems in understanding the electronic transport properties of carbon nanotube ropes. *Current Applied Physics*, 1:50–55, 2001.

[47] D. P. Wang, D. E. Feldman, B. R. Perkins, A. J. Yin, G. H. Wang, J. M. Xu, and A. Zaslavsky. Hopping conduction in disordered carbon nanotubes. *Solid State Communications*, 142(5):287–291, 2007.

[48] V. K. Ksenevich, V. B. Odzaev, Z. Martunas, D. Seliuta, G. Valusis, J. Galibert, A. A. Melnikov, A. D. Wieck, D. Novitski, M. E.

Kozlov, and V. A. Samuilov. Localization and nonlinear transport in single walled carbon nanotube fibers. *Journal of Applied Physics*, 104(7):073724, 2008.

[49] V. Skákalová, A. B. Kaiser, Z. Osváth, G. Vértesy, L.P. Biró, and S. Roth. Ion irradiation effects on conduction in single-wall carbon nanotube networks. *Applied Physics A*, 90(4):597–602, January 2008.

[50] T. M. Barnes and J. L. Blackburn. Reversibility, dopant desorption, and tunneling in the temperature-dependent conductivity of type-separated, conductive carbon nanotube networks. *Physics Letters A*, 2(9), 2008.

[51] V. Skákalová, A. B. Kaiser, Y.-S. Woo, and S. Roth. Electronic transport in carbon nanotubes: From individual nanotubes to thin and thick networks. *Physical Review B*, 74(8):085403, August 2006.

[52] A. B. Kaiser, G. Düsberg, and S. Roth. Heterogeneous model for conduction in carbon nanotubes. *Physical Review B*, 57(3):1998–2001, 1998.

[53] M. Shiraishi and M. Ata. Conduction mechanisms in single-walled carbon nanotubes. *Synthetic metals*, 2002.

[54] M. Harada, T. Inagaki, S. Bandow, and S. Iijima. Effects of boron-doping and heat-treatment on the electrical resistivity of carbon nanohorn-aggregates. *Carbon*, 46(5):766–772, April 2008.

[55] J. Macutkevic, R. Adomavicius, A. Krotkus, J. Banys, V. Kuznetsov, S. Moseenkov, A. Romanenko, and O. Shenderova. Localization and electrical transport in onion-like carbon based composites. *Journal of Applied Physics*, 111(10):103701, 2012.

[56] A. I. Romanenko, O. B. Anikeeva, A. V. Okotrub, L. G. Bulusheva, and V. L. Kuznetsov. The Temperature Dependence of the Electrical Re-

sistivity and the Negative Magnetoresistance of Carbon Nanoparticles. *Physics of the Solid State*, 44(3):487–489, 2002.

[57] R. Avriller, S. Roche, F. Triozon, X. Blase, and S. Latil. Low-Dimensional Quantum Transport Properties of Chemically-Disordered Carbon Nanotubes: From Weak To Strong Localization Regimes. *Modern Physics Letters B*, 21(29):1955–1982, 2007.

[58] L. El Mir, S. Kraiem, M. Bengagi, E. Elaloui, a. Ouederni, and S. Alaya. Synthesis and characterization of electrical conducting nanoporous carbon structures. *Physica B: Condensed Matter*, 395(1-2):104–110, May 2007.

[59] K. C. Mondal, A. M. Strydom, Z. Tetana, S. D. Mhlanga, M. J. Witcomb, J. Havel, R. M. Erasmus, and N. J. Coville. Boron-doped carbon microspheres. *Materials Chemistry and Physics*, 114(2-3):973–977, April 2009.

[60] W. P. Wright, V. D. Marsicano, J. M. Keartland, R. M. Erasmus, S. M.a. Dube, and N. J. Coville. The electrical transport properties of nitrogen doped carbon microspheres. *Materials Chemistry and Physics*, 147(3):908–914, October 2014.

[61] H. Bottger and V.V. Bryksin. *Hopping Conduction in Solids*. Number ISBN 3-527-26451-5. VCH Publishers, 1985.

[62] A. Miller and E. Abrahams. Impurity conduction at low concentrations. *Physical Review*, 257, 1960.

[63] V. Ambegaokar, B. I. Halperin, and J. S. Langer. Hopping conductivity in disordered systems. *Physical review B*, 4:2612–2620, 1971.

[64] N. F. Mott. Conduction in non-crystalline materials. *Philosophical Magazine*, 19:835–852, apr 1969.

[65] A. Efros and B. Shklovskii. Coulomb gap and low temperature con-

ductivity of disordered systems. *J. Phys. C*, 8:49–51, 1975.

[66] P. Sheng. Fluctuation-induced tunneling conduction in disordered materials. *Physical Review B*, 21(6):2180–2195, 1980.

[67] T. Belin and F. Epron. Characterization methods of carbon nanotubes: a review. *Materials Science and Engineering: B*, 119(2):105–118, May 2005.

[68] E. F. Antunes, Lobo, E. J. Corat, V. J. Trava-Airoldi, A. A. Martin, and C. Veríssimo. Comparative study of first- and second-order Raman spectra of MWCNT at visible and infrared laser excitation. *Carbon*, 44(11):2202–2211, September 2006.

[69] M. J. Sobkowicz, J. R. Dorgan, K. W. Gneshin, A. M. Herring, and J. T. McKinnon. Controlled dispersion of carbon nanospheres through surface functionalization. *Carbon*, 47(3):622–628, March 2009.

[70] M. Galambos, G. Fábián, F. Simon, L. Ćirić, L. Forró, L. Korecz, a. Rockenbauer, J. Koltai, V. Zólyomi, Á. Rusznyák, J. Kürti, N. M. Nemes, B. Dóra, H. Peterlik, R. Pfeiffer, H. Kuzmany, and T. Pichler. Identifying the electron spin resonance of conduction electrons in alkali doped SWCNTs. *Physica Status Solidi (B)*, 246(11-12):2760–2763, December 2009.

[71] A. C. Ferrari, J. C. Meyer, V. Scardaci, C. Casiraghi, M. Lazzeri, F. Mauri, S. Piscanec, D. Jiang, K. S. Novoselov, S. Roth, and A. K. Geim. Raman spectrum of graphene and graphene layers. *Physical Review Letters*, 97(18):187401, 2006.

[72] Y. Z. Jin, C. Gao, Wen K. H., Y. Zhu, A. Huczko, M. Bystrzejewski, M. Roe, C. Y. Lee, S. Acquah, H. Kroto, and D. R.M. Walton. Large-scale synthesis and characterization of carbon spheres prepared by direct pyrolysis of hydrocarbons. *Carbon*, 43(9):1944–1953, August 2005.

[73] J.-Y. Miao, D. W. Hwang, K. V. Narasimhulu, P. Lin, Y.-T. Chen, S.-H. Lin, and L.-P. Hwang. Synthesis and properties of carbon nanospheres grown by CVD using Kaolin supported transition metal catalysts. *Carbon*, 42(4):813–822, January 2004.

[74] Y.a. Kim, T. Hayashi, K. Osawa, M.S. Dresselhaus, and M. Endo. Annealing effect on disordered multi-wall carbon nanotubes. *Chemical Physics Letters*, 380(3-4):319–324, October 2003.

[75] L. L. Zhang, X. Zhao, H. Ji, M. D. Stoller, L. Lai, S. Murali, S. Mcdonnell, B. Cleveger, R. M. Wallace, and R. S. Ruoff. Nitrogen doping of graphene and its effect on quantum capacitance, and a new insight on the enhanced capacitance of N-doped carbon. *Energy & Environmental Science*, 5(11):9618, 2012.

[76] R. P. Vidano and D. B. Fischbach. Observation of Raman band shifting with excitation wavelength for carbons and graphites. *Solid State Communications*, 39:341–344, 1981.

[77] F. Tuinstra. Raman Spectrum of Graphite. *The Journal of Chemical Physics*, 53(3):1126, 1970.

[78] M. Matthews, M. Pimenta, G. Dresselhaus, M. Dresselhaus, and M. Endo. Origin of dispersive effects of the Raman D band in carbon materials. *Physical Review B*, 59(10):R6585–R6588, March 1999.

[79] A. Ferrari and J. Robertson. Interpretation of Raman spectra of disordered and amorphous carbon. *Physical Review B*, 61(20):14095–14107, May 2000.

[80] L. G. Cancado, K. Takai, and T. Enoki. General equation for the determination of the crystallite size La of nanographite by Raman spectroscopy. *Applied Physics Letters*, 88(16):163106, 2006.

[81] M. A. Pimenta, G. Dresselhaus, M. S. Dresselhaus, L. G. Cançado,

A. Jorio, and R. Saito. Studying disorder in graphite-based systems by Raman spectroscopy. *Physical chemistry chemical physics : PCCP*, 9(11):1276–91, March 2007.

[82] D. M. Murphy. *Metal Oxide Catalysis, Volume 1*. WILEY-VCH Verlag GmbH & Co., 2009.

[83] G. Feher and A. F. Kip. Electron spin resonance absorption in metals. I. Experimental. *Physical Review*, 98(2):337, 1955.

[84] M. Bourbin, Y. Le Du, L. Binet, and D. Gourier. Implementing a new EPR lineshape parameter for organic radicals in carbonaceous matter. *Source code for biology and medicine*, 8(1):15, 2013.

[85] F. J. Dyson. Electron spin resonance absorption in metals. II. Theory of electron diffusion and the skin effect. *Physical Review*, 98:349–359, 1955.

[86] S. Mrozowski. Electron spin resonance in neutron irradiated and in doped polycrystalline graphite—Part I. *Carbon*, 3:308–320, 1965.

[87] S. Mrozowski. Electron spin resonance in neutron irradiated and in doped polycrystalline graphite—Part II. *Carbon*, 4(2):227–242, 1966.

[88] S. Mrozowski. ESR of carbons in the transition range—I. *Carbon*, 17(3):227–236, January 1979.

[89] F. Beuneu, C. L'Huillier, J. P. Salvetat, J. M. Bonard, and L. Forró. Modification of multiwall carbon nanotubes by electron irradiation: An ESR study. *Physical Review B*, 59(8):5945–5949, 1999.

[90] M. Kosaka, T. W. Ebbesen, H. Hiura, and K. Tanigaki. Annealing effect on carbon nanotubes. An ESR study. *Chemical Physics Letters*, 233(1-2):47–51, 1995.

[91] V. Likodimos, S. Glenis, and C. L. Lin. Electronic properties of boron-

doped multiwall carbon nanotubes studied by ESR and static magnetization. *Physical Review B*, 72(4):045436, July 2005.

[92] V. G. Pol, S. V. Pol, A. Gedanken, M.-G. Sung, and S. Asai. Magnetic field guided formation of long carbon filaments (sausages). *Carbon*, 42(12-13):2738–2741, January 2004.

[93] B. Corzilius, K.-P. Dinse, and K. Hata. Single-wall carbon nanotubes and peapods investigated by EPR. *Physical chemistry chemical physics : PCCP*, 9(46):6063–72, December 2007.

[94] M. B. Dubazane. *Magnetic Properties of Nitrogen Doped Carbon Nanospheres*. PhD thesis, School of Physics, 2012.

[95] V. D. Marsicano, Wright W. P., Keartland J. M., Erasmus R. M., Dube S.a., and Coville N.J. Characterisation of carbon microspheres using electron paramagnetic resonance spin-concentration techniques. *Proceedings of the South African Institute of Physics Conference 2013*, 30:2013, 2013.

[96] H. Xiong, M. Moyo, M. A. Motchelaho, Z. N. Tetana, S. M. A. Dube, L. L. Jewell, and N. J. Coville. Fischer-Tropsch synthesis: Iron catalysts supported on N-doped carbon spheres prepared by chemical vapor deposition and hydrothermal approaches. *Journal of Catalysis*, 311:80–87, 2014.

[97] P. G. Collins. Extreme Oxygen Sensitivity of Electronic Properties of Carbon Nanotubes. *Science*, 287(5459):1801–1804, mar 2000.

[98] T. Susi, T. Pichler, and P. Ayala. X-ray photoelectron spectroscopy of graphitic carbon nanomaterials doped with heteroatoms. *Beilstein Journal of Nanotechnology*, 6(1):177–192, 2015.

[99] K. N. Wood, R. O'Hayre, and S. Pylypenko. Recent progress on nitrogen/carbon structures designed for use in energy and sustainability

applications. *Energy & Environmental Science*, 7(4):1212, 2014.

[100] X. Li, H. Wang, J. T. Robinson, H. Sanchez, G. Diankov, and H. Dai. Simultaneous Nitrogen Doping and Reduction of Graphene Oxide. *J. Am. Chem. Soc.*, 131(43):15939–15944, 2009.

[101] G. Jian, Y. Zhao, Q. Wu, L. Yang, X. Wang, and Z. Hu. Structural and compositional regulation of nitrogen-doped carbon nanotubes with nitrogen-containing aromatic precursors. *Journal of Physical Chemistry C*, 117(15):7811–7817, 2013.

[102] L. J. van der Pauw. A method of measuring specific resistivity and hall effect of discs of arbitrary shape. *Philips research reports*, 1958.

[103] C. Kasl and M. Hoch. Effects of sample thickness on the van der pauw technique for resistivity measurements. *Rev. Sci. Instrum.*, 2005.

[104] C. Kasl. *Electric transport investigations on the trivalent-ion doped tungsten bronzes YxWO 3 and LAxWO3 near the metal – insulator transition.* PhD thesis, Physics, 2010.

[105] S. Dhall and N. Jaggi. Structural Studies of Functionalized Single-Walled Carbon Nano-Horns. *Fullerenes, Nanotubes and Carbon Nanostructures*, 23(11):942–946, 2015.

[106] C. T. Cioffi. *Functionalization and application of carbon nanohorns and carbon onions.* PhD thesis, School of Physics, 2008.

[107] L. G. Bulusheva, A. V. Okotrub, I. A. Kinloch, I. P. Asanov, A. G. Kurenya, A. G. Kudashov, X. Chen, and H. Song. Effect of nitrogen doping on Raman spectra of multi-walled carbon nanotubes. *Physica Status Solidi (B) Basic Research*, 245(10):1971–1974, 2008.

[108] W. P. Wright. *The electrical transport properties of nitrogen doped carbon microspheres.* PhD thesis, School of Physics, 2013.

[109] D. Joung and S. I. Khondaker. Efros-Shklovskii variable-range hopping in reduced graphene oxide sheets of varying carbon sp2 fraction. *Physical Review B - Condensed Matter and Materials Physics*, 86(23):29–32, 2012.

[110] K. G. Raj and P. A. Joy. Cross over from 3D variable range hopping to the 2D weak localization conduction mechanism in disordered carbon with the extent of graphitization. *Phys. Chem. Chem. Phys.*, 17(24):16178–16185, 2015.

[111] L. Pietronero. Ideal conductivity of carbon polymers and intercalation compounds. *Synthetic Metals*, 8(3):225 – 231, 1983.

[112] B. L. Altshuler, G. W. Martin, D. L. Maslov, V. M. Pudalov, A. Prinz, G. Brunthaler, and G. Bauer. Weak-localization type description of conduction in the "anomalous" metallic state. 2008.

[113] C. K. Lee, J. Cho, J. Ihm, and K. H. Ahn. Ballistic corrections to weak-localization conductance of carbon nanotubes. *Physical Review B - Condensed Matter and Materials Physics*, 69(20):1–5, 2004.

[114] G. Bergmann. Weak Localization in Thin Films. *Physica Scripta*, T14:99–99, 2007.

[115] J. Roberts. Hard amorphous (dimond-like) carbon. *Prog. Solid St. Chem*, 21:199–333, 1991.

[116] D. G. McCulloch, S. Prawer, and A. Hoffman. Structural investigation of xenon-ion-beam-irradiated glassy carbon. *Physical Review B*, 50(9):5905–5917, 1994.

[117] D. G. McCulloch and S. Prawer. The effect of annealing and implantation temperature on the structure of C ion-beam-irradiated glassy carbon. *Journal of Applied Physics*, 78(5):3040–3047, 1995.

[118] S. Prawer, K. W. Nugent, Y. Lifshitz, G. D. Lempert, E. Grossman,

J. Kulik, I. Avigal, and R. Kalish. Systematic variation of the Raman spectra of DLC films as a function of sp2:sp3 composition. *Diamond and Related Materials*, 5(3-5):433–438, 1996.

[119] W. G. Cui, Q. B. Lai, L. Zhang, and F. M. Wang. Quantitative measurements of sp3 content in DLC films with Raman spectroscopy. *Surface and Coatings Technology*, 205(7):1995–1999, 2010.

[120] M. A. Tamor and W. C. Vassell. Raman "fingerprinting" of amorphous carbon films. *Journal of Applied Physics*, 76(6):3823–3830, 1994.

[121] S. Reich and C. Thomsen. Raman spectroscopy of graphite. *Philosophical transactions. Series A, Mathematical, physical, and engineering sciences*, 362(1824):2271–2288, 2004.

[122] S. Boncel, S. W. Pattinson, V. Geiser, M. S. P. Shaffer, and K. K. Koziol. En route to controlled catalytic CVD synthesis of densely packed and vertically aligned nitrogen-doped carbon nanotube arrays. *Beilstein Journal of Nanotechnology*, 5(1):219–233, 2014.

[123] A. C. Ferrari. Raman spectroscopy of graphene and graphite: Disorder, electron-phonon coupling, doping and nonadiabatic effects. *Solid State Communications*, 143(1-2):47–57, 2007.

[124] A C Ferrari and J Robertson. Origin of the 1150-cm Raman mode in nanocrystalline diamond. *Physical Review B - Condensed Matter and Materials Physics*, 63:2–5, 2001.

[125] V. D. Marsicano. Characterisation of carbon microspheres using electron paramagnetic resonance spin-concentration techniques. *in Proceedings of SAIP2013: the 58th Annual Conference of the South African Institute of Physics*, 2013.

[126] W. D. Rice, R. T. Weber, P. Nikolaev, S. Arepalli, V. Burka, and J. Kono. Spin Relaxation Times of Single-Wall Carbon Nanotubes.

Phys. Rev. B, 88:1–6, 2013.

[127] T. G. Castner. Saturation of the Paramagnetic Resonance of a v Center. *Physical Review*, 115(6):1506–1515, 1959.

[128] Z. J. Han and K. Ostrikov. Controlled electronic transport in single-walled carbon nanotube networks: Selecting electron hopping and chemical doping mechanisms. *Applied Physics Letters*, 96(23):233115, 2010.

[129] P. Petit, E. Jouguelet, a. G. Rinzler, and R. E. Smalley. Electron spin resonance and microwave resistivity of single-wall carbon nanotubes. *Physical Review B*, 56(15):9275–9278, 1997.

[130] J. B. Wu, Z. X. Hu, X. Zhang, W. P. Han, Y. Lu, W. Shi, X. F. Qiao, M. Ijis, S. Milana, W. Ji, A. C. Ferrari, and P. H. Tan. Interface Coupling in Twisted Multilayer Graphene by Resonant Raman Spectroscopy of Layer Breathing Modes. *ACS Nano*, 9(7):7440–7449, 2015.

Appendix A

Appendix - Equipment

A.1 Electrical Transport Station

The system employed in acquiring the electrical transport was assembled in the laboratory using commercially available components. The heart of the system is an Intel based personal computer running a student version of LabView. The computer interfaces with the measurement equipment via GPIB and Serial connection. The custom built multiplexer is connected via USB to the LabView computer. The test leads, from the sample chamber placed within the cryostat, are accessed via a breakout box. From there the signals are passed to the multiplexer which routes the signals to the measurement equipment as directed by the computer. Over the duration of the experiment the computer logs the data collected from the multimeters, temperature controllers and thermometers. Ancillary functions such as activating the cryostat pump and initiating cryogen flow are also handled by the computer via the multiplexer. Fig A.1 is a schematic of the overall system and its functions.

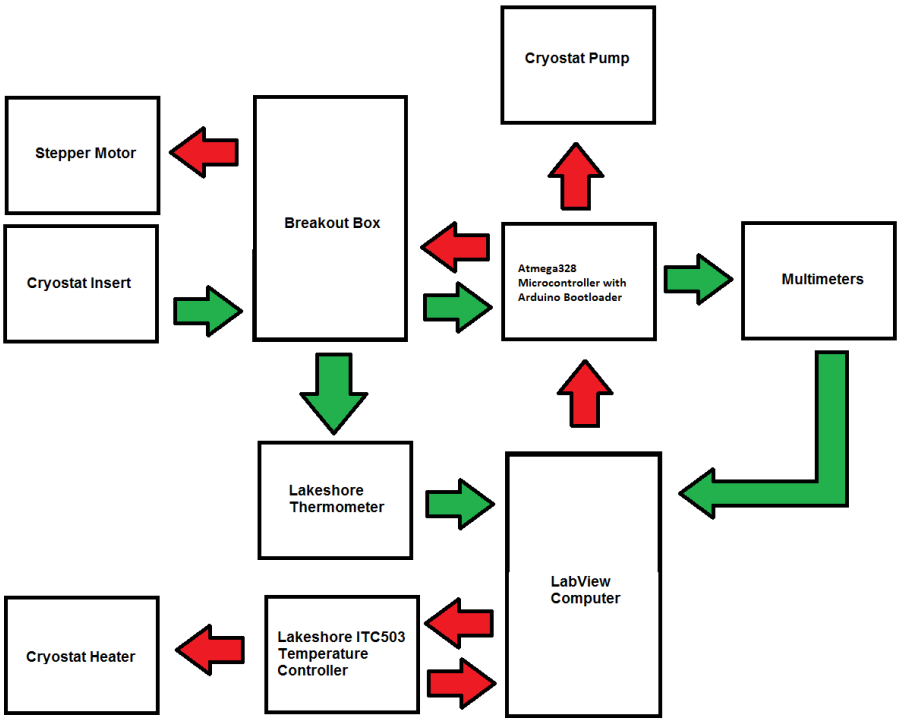

Figure A.1: Overview of the electrical transport station system. Green arrows denote the experiment data while red arrows denote system control commands.

A.2 Multiplexer

As shown in Fig A.1, the Arduino controlled multiplexer was crucial in controlling both the flow of data and the experimental parameters. The circuit diagram for the system is shown in Fig A.2. Only one example relay bank is shown for clarity, three other triplets of relays are present allowing each input to be switched to the four input ports of the multimeters. Not shown are the relays which switch the IV power supply in to the circuit or the relays which control the cryostat pump. The complete Bill of Materials is shown in Tbl A.1. Finally the physical contruction of the multiplexer on perforated board is shown in Fig A.3.

U6	ATMEGA328-PU Microcontroller
C1	Ceramic Capacitor 22pF
C2	Ceramic Capacitor 22pF
C3	Ceramic Capacitor 100nF
C4	Ceramic Capacitor 100nF
D1	Diode 1N4001
D2	Diode 1N4001
D3	Diode 1N4001
D4	Diode 1N4001
U5	MCP4921 DAC
Q1	IRL520N FET
Q2	IRL520N FET
Q3	IRL520N FET
Q4	IRL520N FET
X1	LM324N Op-Amp
RL1	N4100F
RL2	N4100F
RL3	N4100F
R1	Variable Resistor
R2	Variable Resistor
U3	SN74HC595N Shift Register
U4	SN74HC595N Shift Register
U1	ULN2803A Darlington Array
U2	ULN2803A Darlington Array
XTAL1	16Mhz Crystal

Table A.1: Arduino controlled multiplexer Bill Of Materials

Arduino Controlled Multiplexer and IV Power Supply

Vincent Derek Marsicano 2014

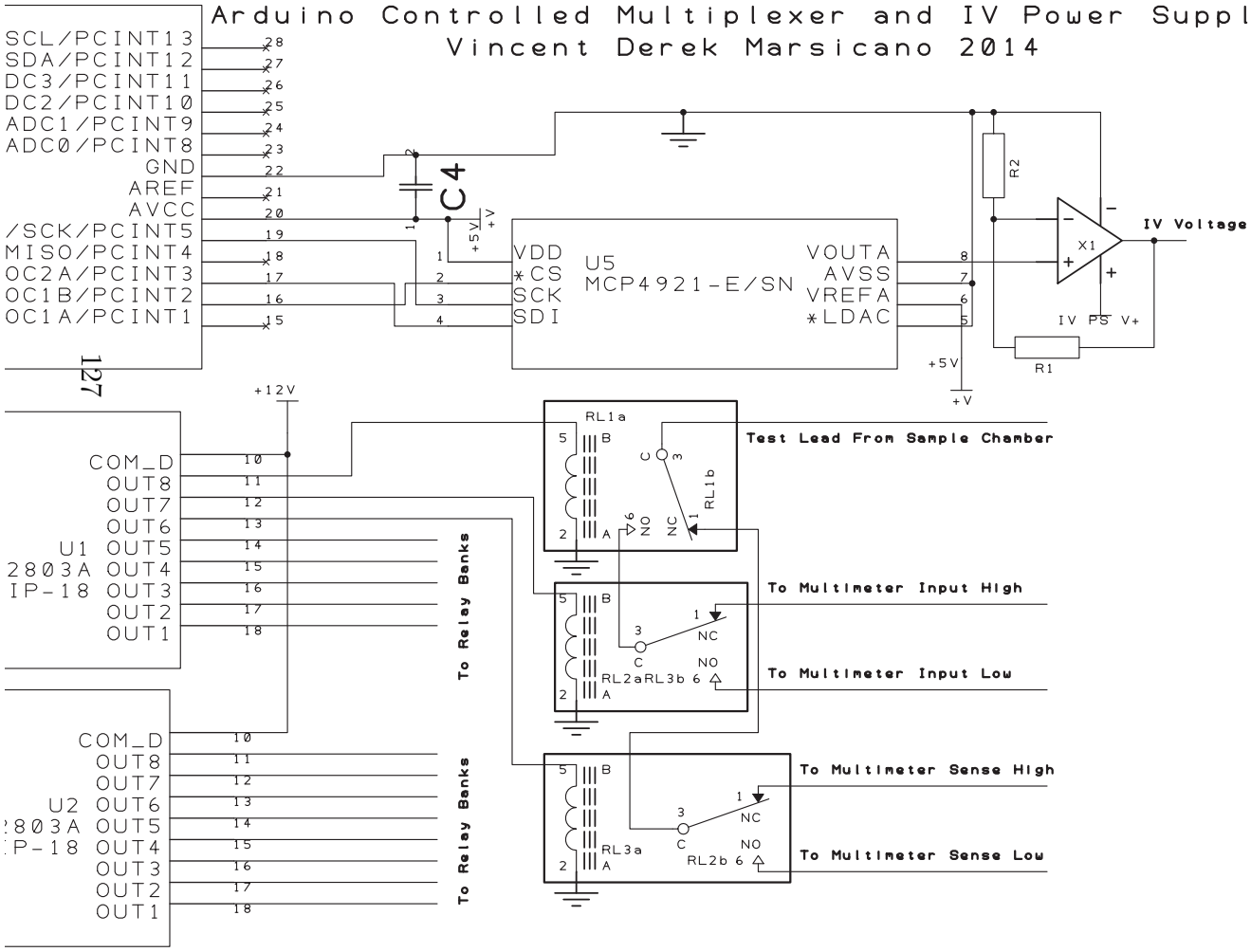

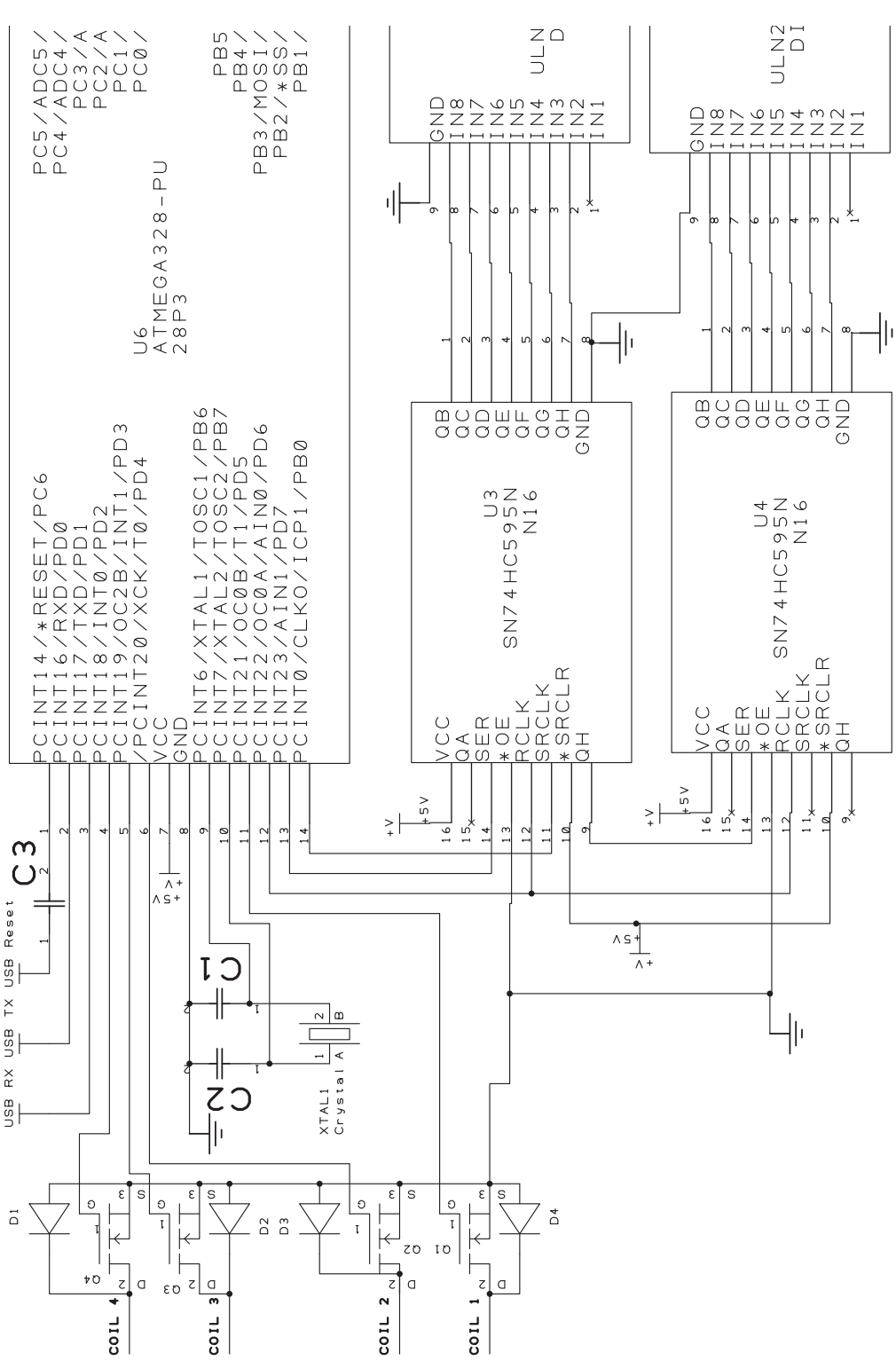
U6
ATMEGA328-PU
28P3
PC5/ADC5/
PC4/ADC4/
PC3/A
PC2/A
PC1/
PC0/
PB5
PB4/
PB3/MOSI/
PB2/*SS/
PB1/
PCINT14/*RESET/PC6
PCINT16/RXD/PD0
PCINT17/TXD/PD1
PCINT18/INT0/PD2
PCINT19/OC2B/INT1/PD3
/PCINT20/XCK/T0/PD4
VCC
GND
PCINT6/XTAL1/TOSC1/PB6
PCINT7/XTAL2/TOSC2/PB7
PCINT21/OC0B/T1/PD5
PCINT22/OC0A/AIN0/PD6
PCINT23/AIN1/PD7
PCINT0/CLKO/ICP1/PB0
U3
SN74HC595N
N16
VCC
QA
SER
*OE
RCLK
SRCLK
*SRCLR
QH
QB
QC
QD
QE
QF
QG
QH
GND
U4
SN74HC595N
N16
ULN
D
ULN2
DI
GND
IN8
IN7
IN6
IN5
IN4
IN3
IN2
IN1
+5V
+V
C3
C1
C2
XTAL1
Crystal A
USB RX
USB TX
USB Reset
D1
D2
D3
D4
Q1
Q2
Q3
Q4
COIL 1
COIL 2
COIL 3
COIL 4

Figure A.2

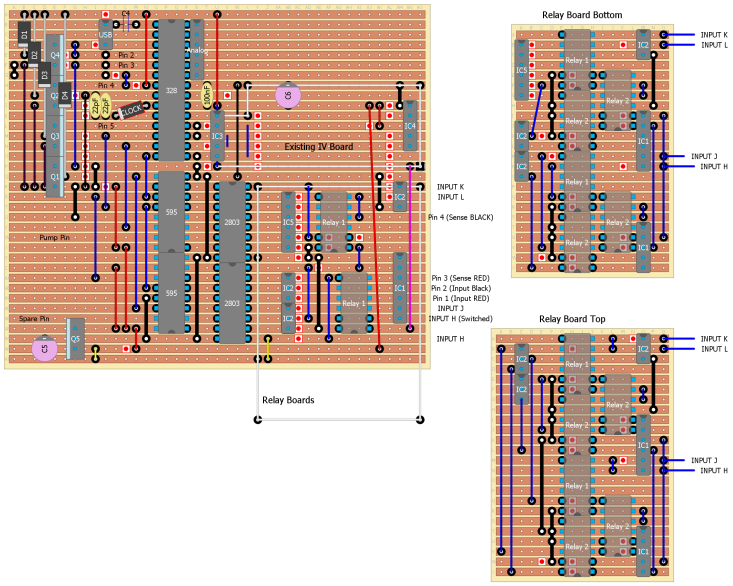

Figure A.3: Veroboard schematic of the multiplexer.

Appendix B

Appendix - Code Developed

The code developed for this thesis includes microcontroller logic used to control the multiplexer, Labview data acquisition and experiment control code and data processing code. Each will be discussed in detail further.

B.1 Arduino Code - Multiplexer

The microcontroller deployed in the multiplexer is easily programmable using the Integrated Development Enviroment (IDE) available as open source code from Arduino. The IDE is based on the Processing programming language and is uploaded to the microcontroller via USB. The microcontroller is preloaded with the Arduino bootloader which can accept the new program as it is uploaded. This microntroller can then control the rest of the multiplexer circuitry as described in Appendix A.

The code that follows was designed to allow for the completion of the electron transport experiment. The commands controlling the multiplexer are sent over serial and detailed in Tbl. B.1. The comments for the code have been highlighted in red. Communication with some of the external chips such as

ASCII Command	Action
A	Set to VDP Resistivity Experiment
B	Set for IV Experiment
C	Set for Magnetoresistance/Hall Effect
a,b,c,d	4 "Positive" orientations of the VDP wiring
e,f,g,h,	4 "Negative" orientations of the VDP wiring
P	Turn on flow cryostat pump
p	Turn off flow cryostat pump
(B mode) 4	Decrease IV voltage by 1 DAC step
(B mode) 6	Increase IV voltage by 1 DAC step
(B mode) 3	Decrease IV voltage by 66 DAC steps
(B mode) 7	Increase IV voltage by 66 DAC steps
(B mode) 2	Decrease IV voltage by 132 DAC steps
(B mode) 8	Increase IV voltage by 132 DAC steps
(B mode) 0	0 IV Voltage, set DAC to 0 point
(B mode) 9	Max IV Voltage, set DAC 4095 point
(C mode) 4	Rotate cryostat Motor by 1 step (1.8°)
(C mode) 6	Rotate cryostat Motor by -1 step (-1.8°)
(C mode) 3	Rotate cryostat Motor by 25 step (45°)
(C mode) 7	Rotate cryostat Motor by -25 steps (-45°)
(C mode) 1	Rotate cryostat Motor by 50 step (90°)
(C mode) 9	Rotate cryostat Motor by -50 step (-90°)

Table B.1: Table of commands available for Arduino controlled multiplexer.

the DAC and shift registers was handled via SPI interface. Various pieces of open-source code were used to develop the multiplexer code such as the SPI and Stepper libraries provided by Arduino under the LGPL license.

"../Appendix B/Multiplex2.ino"

```
#include <Stepper.h>  // Stepper Motor Library
#include "SPI.h"      // SPI power supply library

//Stepper Motor Parameter Definition
  Stepper myStepper = Stepper(200, 2, 4, 5, 3);

// 75HC595 Shift Register Parameters
  int SER_Pin = 7;   //pin 14 on the 75HC595
  int RCLK_Pin = 6;  //pin 12 on the 75HC595
```

```
    int SRCLK_Pin = 8; //pin 11 on the 75HC595
11    //No. of Shift Registers
      #define number_of_74hc595s 2
13    //No. of Outputs per Register
      #define numOfRegisterPins number_of_74hc595s * 8
15    // Register Vector
      boolean registers[numOfRegisterPins];
17
  int del=30;              // used for various delays
19 word outputValue = 0;   // a word is a 16-bit number
  byte data = 0;           // and a byte is an 8-bit number
21 int incomingByte = 0;   //Serial Communication variable
  int a = 0;               //
23 int CNTRpin = 9;        // The CNTR pin of the SPI protocol
  int Mode = 1;            // Mode Variable of the Multiplexer
25
  void setup()
27 {
    //set pin(s) to input and output
29  pinMode(9, OUTPUT); // SPI CNTR pin

31  //Shift Register Pins
    pinMode(SER_Pin, OUTPUT);
33  pinMode(RCLK_Pin, OUTPUT);
    pinMode(SRCLK_Pin, OUTPUT);
35  pinMode(13, OUTPUT);

37  //Stepper Motor Pins
    pinMode(2, OUTPUT);
39  pinMode(3, OUTPUT);
    pinMode(4, OUTPUT);
41  pinMode(5, OUTPUT);
    myStepper.setSpeed(20);
43
    //reset all register pins
45  clearRegisters();
    writeRegisters();
47
    // wake up the SPI bus.
```

```
49    SPI.begin();
      SPI.setBitOrder(MSBFIRST);
51
      // Wake up Serial Communication
53    Serial.begin(9600);
  }
55
  //set all register pins to LOW
57 void clearRegisters(){
      for(int i = numOfRegisterPins - 1; i >=  0; i--){
59       registers[i] = LOW;
      }
61 }

63 // Defined Functions used in this code.

65 //Set and display registers
  //Only call AFTER all values are set how you would like (slow
      otherwise)
67 void writeRegisters(){

69    digitalWrite(RCLK_Pin, LOW);

71    for(int i = numOfRegisterPins - 1; i >=  0; i--){
        digitalWrite(SRCLK_Pin, LOW);
73
        int val = registers[i];
75
        digitalWrite(SER_Pin, val);
77      digitalWrite(SRCLK_Pin, HIGH);

79    }
      digitalWrite(RCLK_Pin, HIGH);
81
  }
83
  //set an individual pin HIGH or LOW
85 void setRegisterPin(int index, int value){
      registers[index] = value;
```

```
87 }

89 // Primary Code Loop

91 void loop()
   {
93
     // Serial Communication Command Structure
95   //3 Modes possible:

97                         //A = 4 wire Resistance
                                // a to d = 4 Orientations of the 4
     wires
99
                           //B = IV mode
101                             // 4 = Reduce Voltage by 1 step
                                // 6 = Raise Volatge by 1 step
103
                                // 3 = Reduce Voltage by 66 step
105                             // 7 = Raise Voltage by 66 step

107                             // 2 = Reduce Voltage by 132 step
                                // 8 = Raise Voltage by 132 step
109
                                // 0 = Zero the Voltage
111                             // 5 = Center the Voltage at 2048
     steps
                                // 9 = Max the Voltage at 4095 steps
113
                           //C = Magnetoresistance
115                          // 4 = 1 step "negative"
                             // 6 = 1 step positive
117
                             // 3 = 25 steps negative (45 degrees)
119                          // 7 = 25 steps positive (45 degrees)

121                          // 1 = 50 steps negative (90 degrees)
                             // 9 = 50 steps positive (90 degrees)
123
```

```
                    // General Commands
125                   // P = Turn on Pump
                      // p = Turn off Pump
127
    if (Serial.available() > 0) {
129                 // read the incoming byte:
                    incomingByte = Serial.read();
131                 switch(incomingByte){

133                   // Numerical Case Structure
                      case 48: // 0
135                       if (Mode == 1) a = 0;
                      break;
137
                      case 49: // 1
139                       if (Mode == 2) myStepper.step(-50);
                      break;
141
                      case 51: // 3
143                       if (Mode == 1) {
                            if (a > 65) a = a - 66;
145                         }
                          if (Mode == 2) myStepper.step(-25);
147                   break;

149                   case 52: // 4
                          if (Mode == 1) {
151                       if (a > 0) a = a - 1;
                          }
153                       if (Mode == 2) myStepper.step(-1);
                      break;
155
                      case 53: // 5
157                       if (Mode == 1) a = 2048;
                      break;
159
                      case 54: // 6
161                       if (Mode == 1){
                          if (a < 4095) a = a + 1;
```

```
163                     }
                        if (Mode == 2) myStepper.step(1);
165                 break;

167                 case 55: // 7
                        if (Mode == 1) {
169                       if (a < 4029) a = a + 66;
                          }
171                     if (Mode == 2) myStepper.step(25);
                    break;
173
                    case 57: //9
175                    if (Mode == 1) a = 4095;
                       if (Mode == 2) myStepper.step(50);
177                 break;

179                 // Shift Register Commands

181                 case 97: //a
                      if (Mode == 0){
183                         setRegisterPin(1, LOW);
                            setRegisterPin(2, LOW);
185                         setRegisterPin(3, LOW);

187                         setRegisterPin(4, HIGH);
                            setRegisterPin(5, LOW);
189                         setRegisterPin(6, LOW);

191                         setRegisterPin(9, LOW);
                            setRegisterPin(10, HIGH);
193                         setRegisterPin(11, LOW);

195                         setRegisterPin(12, LOW);
                            setRegisterPin(13, HIGH);
197                         setRegisterPin(14, HIGH);
                      }
199                   break;

201                   case 98: //b
```

```
                if (Mode == 0){
203                     setRegisterPin(4, LOW);
                        setRegisterPin(5, LOW);
205                     setRegisterPin(6, LOW);

207                     setRegisterPin(9, HIGH);
                        setRegisterPin(10, LOW);
209                     setRegisterPin(11, LOW);

211                     setRegisterPin(12, LOW);
                        setRegisterPin(13, HIGH);
213                     setRegisterPin(14, LOW);

215                     setRegisterPin(1, LOW);
                        setRegisterPin(2, HIGH);
217                     setRegisterPin(3, HIGH);
                }
219             break;

221             case 99: //c
                if (Mode == 0){
223                     setRegisterPin(9, LOW);
                        setRegisterPin(10, LOW);
225                     setRegisterPin(11, LOW);

227                     setRegisterPin(12, HIGH);
                        setRegisterPin(13, LOW);
229                     setRegisterPin(14, LOW);

231                     setRegisterPin(1, LOW);
                        setRegisterPin(2, HIGH);
233                     setRegisterPin(3, LOW);

235                     setRegisterPin(4, LOW);
                        setRegisterPin(5, HIGH);
237                     setRegisterPin(6, HIGH);
                }
239             break;
```

```
241                     case 100: //d
                        if (Mode == 0){
243                             setRegisterPin(12, LOW);
                                setRegisterPin(13, LOW);
245                             setRegisterPin(14, LOW);

247                             setRegisterPin(1, HIGH);
                                setRegisterPin(2, LOW);
249                             setRegisterPin(3, LOW);

251                             setRegisterPin(4, LOW);
                                setRegisterPin(5, HIGH);
253                             setRegisterPin(6, LOW);

255                             setRegisterPin(9, LOW);
                                setRegisterPin(10, HIGH);
257                             setRegisterPin(11, HIGH);
                        }
259                     break;

261                     case 101: //e
                        if (Mode == 0){
263                             setRegisterPin(1, LOW);
                                setRegisterPin(2, LOW);
265                             setRegisterPin(3, LOW);

267                             setRegisterPin(9, HIGH);
                                setRegisterPin(10, LOW);
269                             setRegisterPin(11, LOW);

271                             setRegisterPin(4, LOW);
                                setRegisterPin(5, HIGH);
273                             setRegisterPin(6, LOW);

275                             setRegisterPin(12, LOW);
                                setRegisterPin(13, HIGH);
277                             setRegisterPin(14, HIGH);
                        }
279                     break;
```

```
281                     case 102: //f
                        if (Mode == 0){
283                             setRegisterPin(4, LOW);
                                setRegisterPin(5, LOW);   //H
285                             setRegisterPin(6, LOW);

287                             setRegisterPin(12, HIGH);
                                setRegisterPin(13, LOW);
289                             setRegisterPin(14, LOW);

291                             setRegisterPin(9, LOW);
                                setRegisterPin(10, HIGH);
293                             setRegisterPin(11, LOW);

295                             setRegisterPin(1, LOW);
                                setRegisterPin(2, HIGH); //L
297                             setRegisterPin(3, HIGH);
                        }
299                     break;

301                     case 103: //g
                        if (Mode == 0){
303                             setRegisterPin(4, LOW);
                                setRegisterPin(5, LOW);
305                             setRegisterPin(6, LOW);

307                             setRegisterPin(12, HIGH);
                                setRegisterPin(13, LOW);
309                             setRegisterPin(14, LOW);

311                             setRegisterPin(1, LOW);
                                setRegisterPin(2, HIGH);
313                             setRegisterPin(3, LOW);

315                             setRegisterPin(9, LOW);
                                setRegisterPin(10, HIGH);
317                             setRegisterPin(11, HIGH);
                        }
```

```
319                     break;

321                     case 104: //h
                        if (Mode == 0){
323                             setRegisterPin(9, LOW);
                                setRegisterPin(10, LOW);
325                             setRegisterPin(11, LOW);

327                             setRegisterPin(1, HIGH);
                                setRegisterPin(2, LOW);
329                             setRegisterPin(3, LOW);

331                             setRegisterPin(4, LOW);
                                setRegisterPin(5, HIGH);
333                             setRegisterPin(6, LOW);

335                             setRegisterPin(12, LOW);
                                setRegisterPin(13, HIGH);
337                             setRegisterPin(14, HIGH);
                        }
339                     break;

341

343

345                 // Mode Setting
                    case 65:  //Case A (Resist mode)
347                 Mode = 0;
                    setRegisterPin(1, LOW);
349                 setRegisterPin(2, LOW);
                    setRegisterPin(3, LOW);
351
                    setRegisterPin(4, HIGH);
353                 setRegisterPin(5, LOW);
                    setRegisterPin(6, LOW);
355
                    setRegisterPin(7, LOW);     // Enables Other
    Pins
```

```
357
                    setRegisterPin(9, LOW);
359                 setRegisterPin(10, HIGH);
                    setRegisterPin(11, LOW);
361
                    setRegisterPin(12, LOW);
363                 setRegisterPin(13, HIGH);
                    setRegisterPin(14, HIGH);
365
                    setRegisterPin(15, HIGH);     // Disconnects
    Voltage
367
                    a = 0;                        // Turn Off IV power
    Supply
369
                    digitalWrite(2, LOW);
371                 digitalWrite(3, LOW);
                    digitalWrite(4, LOW);    // Set Motor windings
    off
373                 digitalWrite(5, LOW);

375                 break;

377                 case 66: // Case B (IV Mode)
                    Mode = 1;
379                 setRegisterPin(1, LOW);
                    setRegisterPin(2, HIGH);
381                 setRegisterPin(3, HIGH);

383                 setRegisterPin(4, LOW);
                    setRegisterPin(5, HIGH);
385                 setRegisterPin(6, HIGH);

387                 setRegisterPin(7, HIGH);     // Disables Other
    Pins

389                 setRegisterPin(9, LOW);
                    setRegisterPin(10, HIGH);
391                 setRegisterPin(11, HIGH);
```

```
393                 setRegisterPin(12, HIGH);
                    setRegisterPin(13, LOW);
395                 setRegisterPin(14, LOW);

397                 setRegisterPin(15, LOW);     // Connects
    Voltage

399                 digitalWrite(2, LOW);
                    digitalWrite(3, LOW);
401                 digitalWrite(4, LOW);    // Set Motor windings
    off
                    digitalWrite(5, LOW);
403

405                 break;
                    case 67: // Case C (Magneto Resistance Mode)
407                 Mode = 2;

409

                    setRegisterPin(1, LOW);
411                 setRegisterPin(2, LOW);
                    setRegisterPin(3, LOW);
413
                    setRegisterPin(4, HIGH);
415                 setRegisterPin(5, LOW);
                    setRegisterPin(6, LOW);
417
                    setRegisterPin(9, LOW);
419                 setRegisterPin(10, HIGH);
                    setRegisterPin(11, LOW);
421
                    setRegisterPin(12, LOW);
423                 setRegisterPin(13, HIGH);
                    setRegisterPin(14, HIGH);
425
                    a = 0;
427
                    break;
```

```
429
                    //Pump Control
431                 case 80:
                    setRegisterPin(0, HIGH);
433                 break;
                    case 112:
435                 setRegisterPin(0, LOW);
                    break;
437
                  }
439               // say what you got:
                  Serial.print("I received: ");
441               Serial.println(a);
      }
443   outputValue = a;
      digitalWrite(CNTRpin, LOW);
445   data = highByte(outputValue);
      data = 0b00001111 & data;
447   data = 0b00110000 | data;
      SPI.transfer(data);
449   data = lowByte(outputValue);
      SPI.transfer(data);
451   digitalWrite(CNTRpin,HIGH);


453
    writeRegisters();
455
}
```

B.2 LabView Code

LabView is a graphical programming language developed by National Instruments and used especially in experiment control and data acquisition. National Instruments also provides drivers for the most popular equipment and communication protocols. Communication with the measurement equipment was achieved over a GPIB interface while the experiment was controlled over Serial RS232 for the Oxford temperature controller and a USB to Serial converter for the multiplexer.

B.2.1 Hall Effect

An example of the user interface for the Hall effect code is shown in Fig. B.1. The user inputs allows the customisation of experiment parameters and saves the data to a customised file in the CSV format. The angle of the motors rotation, which changes the effective magnetic field apparent on the sample, can be customised. The number of readings of the Hall Voltage to perform after each rotation and how many repetitions of the experiment are available user inputs. The most current values received from the measurement equipment is also displayed for ease of access.

B.2.2 Resistivity and IV

The GUI for the LabView code which controlled the resistivity experiment is shown in Fig B.2. After assigning the correct communication ports for the correct equipment, called in this context VISA assignments the code allows a number of experimental parameters to be controlled. The code is designed to set a desired temperature to the temperature controller, wait a prescribed period for thermal equilibrium to be achieved, proceed with experiment and continue to a new temperature. At each temperature point the code completes a Van der Pauw experiment by taking 4 wire readings with the Fluke

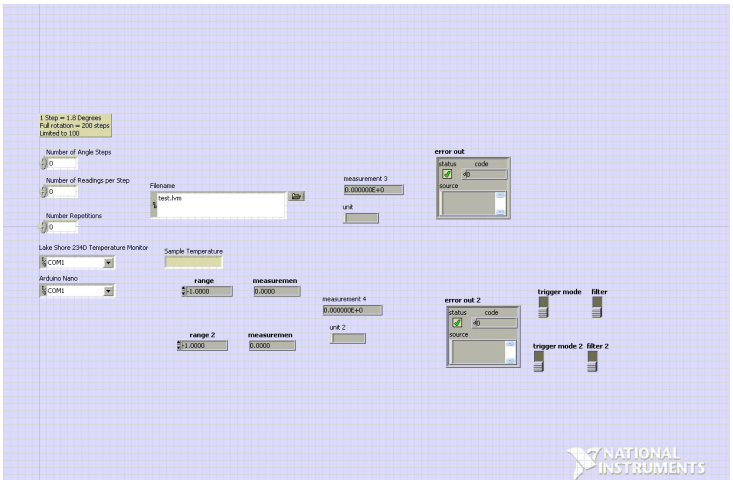

Figure B.1: GUI of Labview automation code for the Hall Effect Experiment

multimeter and subsequently rotating the contacts around the sample using the relay bank constructed in to the Arduino multiplexer. A full set of rotation is completed, with a user defined number of readings for each orientation, then the current leads are reversed and the process is again repeated in the 4 orientations creating the "reversed" Van der Pauw readings. This is done to eliminate the contact resistance and other experimental factored from the data. Subsequent to this the multiplexer is set in to IV mode and the code issue an instruction to the voltage source to increase the voltage by a user defined number of steps, then a set of current and voltage readings are written to the data file. The voltage is then increased again and the process is repeated to the user defined end point. The experiment at this particular temperature being completed the system can then set the IV voltage to 0 and set the temperature controller to a new temperature. The current state of the experiment can be read on the leftmost column of the GUI with information such as the current temperature, the current VDP orientation, the last readings taken from all the measurement equipment and the current voltage the IV power supply is set to. This code was developed with the assistance of William Patrick Wright who wrote the base code for the VDP experiment which was expanded to include the IV experiment simultaneously. The num-

ber of readings and the direction of the temperature during the experiment are also configurable from the GUI.

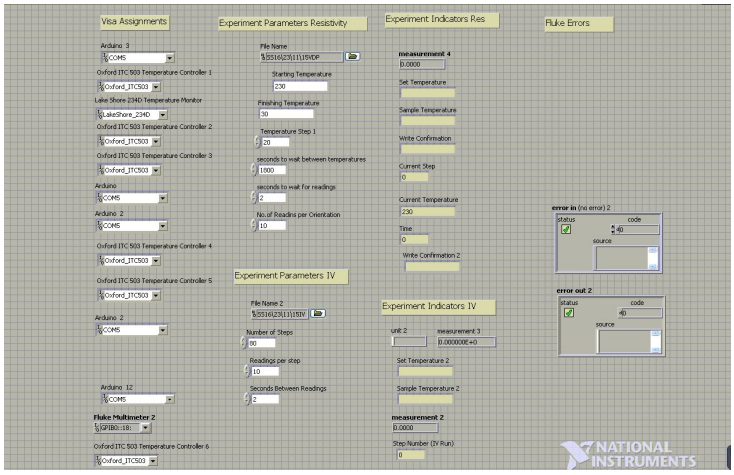

Figure B.2: GUI of LabView automation code for the Resistivity and IV experiment.

B.3 Matlab Code - Low Temperature ESR

Matlab code was developed to quickly and easily produce results for the low temperature ESR experiment. A fast readout of the signal amplitude, linewidth and assymetry were produced. Further processing was completed using Microsoft Excel. The code scans the raw data file, converted from the proprietary Bruker format into a tab delimited data file, for the peaks of the ESR signal. It deduces their positions and heights and records them in a new data file in comma delimited format. This is repeated for all the entire temperature range under investigation and creating a file of all the peak parameters for each temperature.

"../Appendix B/Temprun.m"

```
TempNo = 24;
Data = zeros(TempNo,1);

THING = csvread('XINF.csv');

Mins = zeros(TempNo,1);
Maxs = zeros(TempNo,1);
FieldMin = zeros(TempNo,1);
FieldMax = zeros(TempNo,1);


for index = 1:TempNo;

    file = 'sdct';
    b = THING(index);
    a = num2str(b);

    if index == 1;
        name = strcat(file,'0','80','ps25.asc');
    elseif index == 2;
        name = strcat(file,'0','90','ps25.asc');
    else
        name = strcat(file,a,'ps25.asc');
```

```
        end
26
        Data1 = dlmread(name);
28      W1X = Data1(:,1);
        W1Y = Data1(:,2);
30
        [A,B] = min(W1Y);
32      Mins(index) = A;
        FieldMin(index) = W1X(B);
34      [C,D] = max(W1Y);
        Maxs(index) = C;
36      FieldMax(index) = W1X(D);
        InvT(index) = (1/THING(index));
38
    end
40
    DeltaM = Maxs - Mins;
42  plot((THING),(DeltaM))

44  Final = zeros(length(DeltaM),6);
    Final(:,1) = THING;
46  Final(:,2) = InvT;
    Final(:,3) = Maxs;
48  Final(:,4) = FieldMax;
    Final(:,5) = Mins;
50  Final(:,6) = FieldMin;
    csvwrite('OUT.csv',Final);
```

B.4 Matlab Code - Resonance Condition

Custom designed code was developed in an attempt to deconvolute the compound ESR signals of the CMS sample and the DPPH marker. The code iteratively shifts and scales a reference DPPH signal and subtracts it from the compound signal. The result is then compared to a known CMS signal. The result of the sum of the residuals is then recorded. The process is repeated and the new sum of the residuals is compared to the recorded value from the previous iteration. If the similarity of the signals, defined by a reduction in the sum of the residuals, improves the new shift and scale parameters are recorded. If the process converges the result is displayed on a user friendly GUI in order and small corrections can be manually input. The difference between centre of the DPPH signal and CMS signal can then be easily acquired from the data. This determines the g-value more accurately than what could be achieved by direct calculation from the spectrometer due to the limitations in the accuracy of the microwave photon frequency. The sample code and an image of the GUI are presented here. The GUI code was modified from a GUI tutorial file available from Mathworks and imported in to this code to facilitate the construction of the GUI.

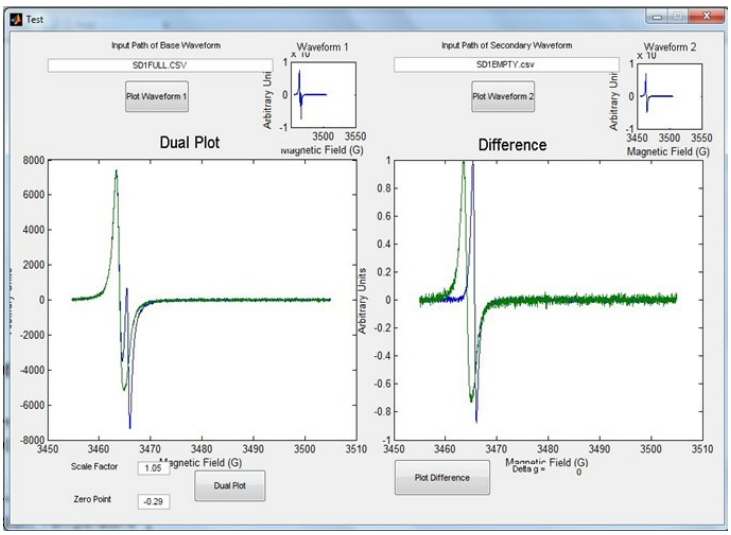

Figure B.3: GUI of Matlab ESR Deconvolution Program

"../Appendix B/Test.m"

```
function varargout = Test(varargin)

gui_Singleton = 1;
gui_State = struct('gui_Name',       mfilename, ...
                   'gui_Singleton',  gui_Singleton, ...
                   'gui_OpeningFcn', @Test_OpeningFcn, ...
                   'gui_OutputFcn',  @Test_OutputFcn, ...
                   'gui_LayoutFcn',  [] , ...
                   'gui_Callback',   []);
if nargin && ischar(varargin{1})
    gui_State.gui_Callback = str2func(varargin{1});
end

if nargout
    [varargout{1:nargout}] = gui_mainfcn(gui_State, varargin{:})
    ;
else
    gui_mainfcn(gui_State, varargin{:});
end
% End initialization code - DO NOT EDIT


% --- Executes just before Test is made visible.
function Test_OpeningFcn(hObject, eventdata, handles, varargin)

% Choose default command line output for Test
handles.output = hObject;

% Update handles structure
guidata(hObject, handles);

% UIWAIT makes Test wait for user response (see UIRESUME)
% uiwait(handles.figure1);


% --- Outputs from this function are returned to the command
    line.
function varargout = Test_OutputFcn(hObject, eventdata, handles)
```

```
37
% Get default command line output from handles structure
39 varargout{1} = handles.output;

41 function edit1_Callback(hObject, eventdata, handles)

43 % --- Executes during object creation, after setting all
    properties.
function edit1_CreateFcn(hObject, eventdata, handles)
45
if ispc && isequal(get(hObject,'BackgroundColor'), get(0,'
    defaultUicontrolBackgroundColor'))
47     set(hObject,'BackgroundColor','white');
end
49
function edit5_Callback(hObject, eventdata, handles)
51
guidata(hObject, handles);
53
% --- Executes during object creation, after setting all
    properties.
55 function edit5_CreateFcn(hObject, eventdata, handles)

57 if ispc && isequal(get(hObject,'BackgroundColor'), get(0,'
    defaultUicontrolBackgroundColor'))
     set(hObject,'BackgroundColor','white');
59 end

61 function edit2_Callback(hObject, eventdata, handles)

63 % --- Executes during object creation, after setting all
    properties.
function edit2_CreateFcn(hObject, eventdata, handles)
65
if ispc && isequal(get(hObject,'BackgroundColor'), get(0,'
    defaultUicontrolBackgroundColor'))
67     set(hObject,'BackgroundColor','white');
end
69
```

```
function edit3_Callback(hObject, eventdata, handles)

handles.zeropoint = get(handles.edit_zero,'String');
handles.scalefactor = get(handles.edit_scale,'String');
handles.W2YC = (handles.W2Y * str2num(handles.scalefactor));
handles.W2XC = (handles.W2X + str2num(handles.zeropoint));


axes(handles.axes1);
plot(handles.W1X, handles.W1Y, handles.W2XC, handles.W2YC);

handles.inter = interp1(handles.W2XC, handles.W2YC, handles.W1X,'
    linear');
axes(handles.axes4);
plot(handles.W1X,(handles.W1Y - handles.inter));
xlabel('Magnetic Field (G)');
ylabel('Arbitrary Units');

guidata(hObject, handles);

% --- Executes during object creation, after setting all
    properties.
function edit3_CreateFcn(hObject, eventdata, handles)

if ispc && isequal(get(hObject,'BackgroundColor'), get(0,'
    defaultUicontrolBackgroundColor'))
    set(hObject,'BackgroundColor','white');
end

% --- Executes on button press in wave2_pushbutton.
function wave2_pushbutton_Callback(hObject, eventdata, handles)


ed2 = get(handles.edit_wave2,'String');
nam2 = ed2{1};
Data2 = csvread(nam2,4,0);
handles.W2X = Data2(:,1);
handles.W2Y = Data2(:,2);

```

```
    set(handles.edit_zero,'String','0');
107 set(handles.edit_scale,'String','1');

109 axes(handles.axes2);
    plot(handles.W2X,handles.W2Y);
111 xlabel('Magnetic Field (G)');
    ylabel('Arbitrary Units');
113
    guidata(hObject, handles);
115
    % --- Executes on button press in wave1_pushbutton.
117 function wave1_pushbutton_Callback(hObject, eventdata, handles)

119 ed1 = get(handles.edit5,'String');
    nam1 = ed1{1};
121 Data1 = csvread(nam1,4,0);
    handles.W1X = Data1(:,1);
123 handles.W1Y = Data1(:,2);


125
    set(handles.edit_zero,'String','0');
127 set(handles.edit_scale,'String','1');

129 axes(handles.axes3);
    plot(handles.W1X,handles.W1Y);
131 xlabel('Magnetic Field (G)');
    ylabel('Arbitrary Units');
133
    guidata(hObject, handles);
135
    % --- Executes on button press in difference_pushbutton.
137 function difference_pushbutton_Callback(hObject, eventdata,
        handles)

139 %Constants
    mu = 9.274*10^-24;
141 h = 6.626*10^-34;
    nu = 9.77*10^9;
143
```

```
tic
trigger = 0;
refdata = csvread('GREF.csv',4,0);
handles.refdatX = refdata(:,1);
handles.refdatY = refdata(:,2);

a = max(handles.refdatY);
handles.refdatYC = handles.refdatY;
handles.refdatY = handles.refdatY / a;

t = 0;
preresidavg = 10000000000000;
beta = 0;
BETA = 0;

for i = 0.5:0.1:2.5
    for j = -5:0.1:5

        scalenum = i;
        zeronum = j;

        handles.W2YC = (handles.W2Y * scalenum);
        handles.W2XC = (handles.W2X + zeronum);
        if (zeronum == -3.5) && (scalenum == 0.9);
            trigger = 1;
            scalenum;
            zeronum;
        else
            trigger = 0;
        end

        t = 0;

        handles.inter = interp1(handles.W2XC, handles.W2YC,
    handles.W1X, 'linear');
        diffY = handles.W1Y - handles.inter;

        b = max(diffY);
        diffYC = diffY;
```

```
        diffY = diffY / b;
183
185             thing = 0.1 * max(handles.refdatY);
                        for k = 1:length(handles.refdatY)
187
189                         if abs(handles.refdatY(k)) >= 0.1
191                             t = t +1;
                                ALPHA = zeros(t+1,1);
193                             ALPHAX = zeros(length(ALPHA),1);
                                for l = 1:t
195                                 ALPHA(l) = BETA(l);
                                    ALPHAX(l) = l;
197                             end
                                ALPHA(t+1) = handles.refdatY(k);
199                             ALPHAX(t+1) = ALPHAX(t) + 1;
                                BETA = ALPHA;
201                         end
203                     end
            trig = 1;
205         thong = 0.1 * max(diffY);
                        for k = 1:length(diffY)
207
                            if (trig == 1) && (abs(diffY(k)) >=
    0.1)
209
                                trig = 0;
211                             alpha = zeros(length(ALPHA),1);
                                alphax = (linspace(1,length(
    alpha)+1,length(alpha)+1))';
213                             for l = k:(k+length(alpha))
                                    alpha(l - (k-1)) = diffY(l);
215
                                end
217                             %alpha(t+1) = diffY(k);
                                %alphax(t+1) = alphax(t) + 1;
```

```
219                                     %beta = alpha;

221                                 end

223                             end

225
                Falpha = gradient(smooth(alpha));
227             FALPHA = gradient(smooth(ALPHA));

229             interpalpha = interp1(alphax,alpha,ALPHAX,'linear');

231
                    residual = zeros(length(interpalpha),0);
233                 residual = abs(interpalpha - ALPHA);
                    residavg = sum(residual);
235


237
                    if residavg < preresidavg;
239                     ALPHAFINAL = ALPHA;
                        ALPHAXFINAL = ALPHAX;
241                     alphafinal = interpalpha;
                        handles.interpsave = diffYC;
243                     residualsave = residual;
                        handles.scalefactor = scalenum;
245                     handles.zeropoint = zeronum;
                        scalenum
247                     zeronum
                        preresidavg = residavg

249

251                 end
        end
253 end

255 [C,D] = max(handles.interpsave);
    [E,F] = max(handles.refdatY);
257
```

```
deltag = (h * nu) / (mu * (handles.W1X(D)/10000)) - (h * nu) / (
    mu * (handles.refdatX(F)/10000))
thing = handles.W1X(D) - handles.refdatX(F)
toc

handles.W2YC = (handles.W2Y * handles.scalefactor);
handles.W2XC = (handles.W2X + handles.zeropoint);



axes(handles.axes1);
plot(handles.W1X, handles.W1Y, handles.W2XC, handles.W2YC);
xlabel('Magnetic Field (G)');
ylabel('Arbitrary Units');


axes(handles.axes4);
plot(handles.W1X, handles.interpsave, handles.refdatX, handles.
    refdatYC);
%plot(ALPHAXFINAL, alphafinal, ALPHAXFINAL, ALPHAFINAL);
xlabel('Magnetic Field (G)');
ylabel('Arbitrary Units');

guidata(hObject, handles);

function edit_zero_Callback(hObject, eventdata, handles)

handles.zeropoint = get(handles.edit_zero, 'String');
handles.scalefactor = get(handles.edit_scale, 'String');
handles.W2YC = (handles.W2Y * str2num(handles.scalefactor));
handles.W2XC = (handles.W2X + str2num(handles.zeropoint));

axes(handles.axes1);
plot(handles.W1X, handles.W1Y, handles.W2XC, handles.W2YC);
xlabel('Magnetic Field (G)');
ylabel('Arbitrary Units');

handles.inter = interp1(handles.W2XC, handles.W2YC, handles.W1X, '
    linear');
```

```
axes(handles.axes4);
plot(handles.W1X,(handles.W1Y - handles.inter));
xlabel('Magnetic Field (G)');
ylabel('Arbitrary Units');

guidata(hObject, handles);

% --- Executes during object creation, after setting all
    properties.
function edit_zero_CreateFcn(hObject, eventdata, handles)
if ispc && isequal(get(hObject,'BackgroundColor'), get(0,'
    defaultUicontrolBackgroundColor'))
    set(hObject,'BackgroundColor','white');
end

% --- Executes on button press in dual_pushbutton.
function dual_pushbutton_Callback(hObject, eventdata, handles)

handles.zeropoint = get(handles.edit_zero,'String');
handles.scalefactor = get(handles.edit_scale,'String');
handles.W2YC = (handles.W2Y * str2num(handles.scalefactor));
handles.W2XC = (handles.W2X + str2num(handles.zeropoint));

axes(handles.axes1);
plot(handles.W1X, handles.W1Y, handles.W2XC, handles.W2YC);
xlabel('Magnetic Field (G)');
ylabel('Arbitrary Units');
guidata(hObject, handles);
```